8-24-2011

Air Plasma Sprayed Thermal Barrier Coatings: Experiments and Finite Element Analysis

Charles H. Thistle
charles.thistle@uconn.edu

Air Plasma Sprayed Thermal Barrier Coatings: Experiments and Finite Element Analysis

Charles Thistle

B.S.E., University of Connecticut, 2008
B.S., University of Connecticut, 2008

A Thesis

Submitted in Partial Fulfillment of the

Requirements for the Degree of

Master of Science

at the

University of Connecticut

2011

APPROVAL PAGE

Master of Science Thesis

Air Plasma Sprayed Thermal Barrier Coatings: Experiments and Finite Element Analysis

Presented by

Charles Thistle, B.S.E.

Major Advisor_____
Eric H. Jordan

Associate Advisor_____
Maurice Gell

Associate Advisor_____
Leon Shaw

University of Connecticut

2011

Acknowledgements

I would like to thank my major advisor, Dr. Eric Jordan, for his direction and assistance on this project. His daily guidance, on which I relied, and his wealth of knowledge and experience in the several fields upon which this thesis touches, proved invaluable in the successful completion of this work.

I would also like to thank my associate advisors, Dr. Maurice Gell and Dr. Leon Shaw, for reviewing this work, and whose willingness to help was fully appreciated.

Special thanks should be given to Jeff Roth and Mak Redjdal for their persistent encouragement and teaching along the way.

Finally, I wish to thank my parents, whose enthusiasm and patient support, which I appreciate greatly, have made this work possible.

Contents

List of Figures

List of Tables

Abstract

The purpose of this research is to examine the primary in-service failure mechanism of an air plasma sprayed thermal barrier coating commonly used in combustor applications, and to use that failure mechanism as a basis in developing a life prediction strategy. The research consisted of an experimental phase, in which the failure mechanism was identified and key features of the coating system measured, and a modeling phase, in which the findings of the experimental phase were used to build a system specific finite element model of the coating in order to extract relevant quantitative data for future use in a life prediction model. Observations were made on multiple thermal barrier coating samples, consisting of a nickel-based super alloy substrate, a MCrAlY bond coat, a thin layer of thermally grown oxide (TGO) which thickens during service, and an air-plasma sprayed yttria-stabilized zirconia (YSZ) coating. The samples originated from three sources, which offered three distinct failure conditions for evaluation and comparison: actual engine failed combustor liner panels, oxidation test samples, and a burner rig test specimen.

Observations were made by carefully sectioning the samples and evaluating them with an environmental scanning electron microscope (ESEM) equipped with energy dispersive spectroscopy (EDS) capability and in some cases an x-ray diffraction (XRD) machine and a field emission scanning electron microscope (FESEM). All three types of samples failed due to cracking in the same location: in the YSZ just above the TGO/YSZ interface. The mechanism proposed to explain the failure is initiated by areas of out-of-plane tension in the YSZ induced by pre-existing undulations at the TGO/YSZ

interface, and worsened by TGO growth and bond coat rumpling. Cracks, most likely initiated at splat boundaries, are extended by this tension until they reach a critical length at which the in-plane compression upon cooling is large enough to cause buckling.

The rate at which the TGO layer thickens in service is of particular importance to the failure of the system and was obtained experimentally. Oxidation testing was performed on the samples in order to obtain the activation energy for TGO growth, which allows for the calculation of TGO thickness as a function of the system temperature history. The TGO was found to obey a parabolic growth law with a value for activation energy consistent with values reported in the literature. Another important time-dependent feature of the coating is bond coat rumpling. Measurements of the tortuosity, or bond coat/TGO interface length over straight line length, are shown to increase proportionally with the TGO thickness.

Not only TGO thickness and rumpling, which contribute an overall time at temperature effect to the life of the coating, but also cycle frequency and duration, were considered as important factors in the life of the system. In order to quantify these effects it was necessary to build a finite element model of the system. Growth of the TGO layer, rumpling, and aluminum depletion from the bond coat were modeled to ascertain the relative importance of each to the development of stress in the coating. It was determined that TGO growth and rumpling have effects on the major trends of stress development, while aluminum depletion has a more minor role. Since it is assumed that the residual stress state in the YSZ at cool down is responsible for driving

the cracks that are ultimately responsible for failure, a previously developed viscoplastic constitutive model, specific to thermal barrier coatings, was employed in the model. The use of this high fidelity constitutive code to model the small scale geometric features of the TGO/YSZ interface, as well as the interpretation of stresses and strains arising from its use, are the primary new contributions this thesis puts forward. From the modeling results, quantities were identified as potential candidates for use in a damage parameter, which would be capable of tracking the life of the system. Specifically, it is shown that a combination of the inelastic strain accumulated in the coating upon cooling and the inelastic strain generated when the system is at high temperature provides the necessary time and temperature dependent features a damage parameter would need to accurately predict failure lives.

1. Background

A thermal barrier coating (TBC) is a multilayer material, ceramic and metal, whose primary job is to sustain a temperature gradient between the environment and an underlying component. TBCs are most often employed in jet engines and industrial gas turbines where they protect metal components from the hot gas stream in the high temperature sections of the engine. In current engines, the ideal power output increases with the gas temperature at the turbine inlet, but as the gas temperature rises, so does the work required to provide the flow of cooling air needed to bring the hot section materials to within their temperature limitations. The gap between ideal and actual power output represents an inefficiency whose root cause is the inability of component materials to withstand higher engine temperatures [1]. TBCs help close this gap by sustaining a temperature gradient between the hot gas stream and the component surface, typically lowering the maximum surface temperature of the component by 200^{o}C. The lower surface temperature allows the engine designer to either reduce the cooling air to raise efficiency and save fuel, increase the turbine inlet temperature and increase power, or retain the same flow of cooling air and improve component durability.

Modern thermal barrier coatings have their origins in the 1970s. Flame-sprayed ceramic coatings, such as alumina, zirconia-calcia, or zirconia-magnesia, were developed as an alternative to frit enamels, which were applied to aerospace applications in the 1950's, and used in relatively undemanding roles [2-3]. Plasma spraying of materials, which was developed as an offshoot of research into low thrust plasma arc engines for

spacecraft, proved to be an efficient and effective way of depositing ceramics. By 1970, plasma-sprayed ceramics were beginning to see use in low risk hot-sections of aircraft engines. As TBCs saw more advanced applications and hotter temperatures, ongoing materials research found, by 1978, that 6-8% yttria-stabilized zirconia, still used today, optimized the durability of coatings in typical operation [2-4]. TBCs have advanced from use in low risk areas of the engine to the more demanding hot-sections due to, along with material improvements, the confidence gained by advances in life prediction. Life prediction methods, initiated by NASA in the early 1980's [2-3], have advanced significantly up to the present, but the lack of a robust and physically-based life prediction method persists, and precludes TBCs from being used to the fullest extent that the current materials allow.

The temperature of the hot gas in the combustor and at the turbine inlet is typically much hotter than the melting temperature of the superalloy components, which is usually around 1300^{o}C. In service, the engine either cycles frequently, as in the case of airplane engines, cooling and heating the TBC rapidly for many cycles, or it cycles infrequently but for long durations, as in the case of base-load power generating turbines. In these extreme environments, a TBC is susceptible to an array of structural and material phenomena that lead to the eventual degradation and failure of the TBC, exposing the underlying metal to dangerous gases which can accelerate the failure of the component. Because of the apprehension about premature failure with little warning, TBC systems in practice are not designed to their full potential, leaving increases in efficiency and performance on the table. The reason for the apprehension

lies in the fact that although TBCs are over 30 years old, they are still not well understood [5]. The high temperature interplay between mechanical and material phenomena like thermal expansion, diffusion, oxidation, creep, microcracking, sintering, and fatigue is difficult to untangle and leads to very complex and sensitive stress states, making life prediction difficult. A reliable, robust, physically-based life prediction model would allow designs that lead to an enhanced realization of the increases in engine efficiency and performance.

This thesis seeks to establish a solid physical foundation for an APS life prediction model by: (1) determining the dominant failure mechanism through careful experimental observations, (2) systematically studying all the mechanical and material phenomenological configurations that could affect this failure mechanism by use of finite element analysis, (3) developing an in-depth understanding of the most probable combination and identifying a damage parameter that lends itself to use in a life prediction model.

1.1 Review of Thermal Barrier Coatings

TBC systems are composed of four layers (Figure 1.1): (1) a ceramic top coat, typically yittria-stabilized zirconia (YSZ); (2) a thin layer of thermally grown oxide (TGO) that forms during service; (3) an intermetallic bond coat (BC), typically MCrAlY or an aluminide; and (4) the substrate, or underlying component, which in the hot sections of an engine is usually a Ni-based superalloy. These four layers comprise a TBC system. In discussion, however, TBC is sometimes meant to refer only to the YSZ top coat.

1.1.1 Top Coat

The job of the top coat is to provide a temperature drop across its thickness, insulating the substrate from the hot gas stream. Only materials with very low thermal conductivities can achieve this while maintaining a minimal thickness, precluding most metals. A high melting temperature is also required, so ceramics emerge as the obvious choice. The thermal expansion coefficient is also very important, as the ceramic must be able to somewhat keep up with the metal layers as they expand and contract. Low stiffness is required as well, so that the ceramic can absorb any strain imposed upon it by thermal mismatch. Other desirable material properties include phase stability to avoid large strains due to transformation, a low density to promote strain tolerance and reduce weight, and a high hardness to resist erosion and foreign body impact.

The material that is most widely chosen in industry to meet these criteria is Zirconia, ZrO_2, which has one of the lowest thermal conductivities of any ceramic (~ 2.3 $W \cdot m^{-1} \cdot K^{-1}$ at 1000°C, fully dense) [5]. The conductivity is further reduced during deposition, owing to the resultant microstructure. Zirconia also has a high thermal expansion coefficient ($\sim 11 \times 10^{-6}$ $^oC^{-1}$) [5] and a low stiffness due its particular microstructure. It resists corrosion, has a sufficiently high melting temperature of about 2700^{o}C, and holds up well to impact with a hardness of around 14 GPa [5].

Zirconia in its pure form, however, undergoes a phase transformation from monoclinic to tetragonal at 1180^{o}C and from tetragonal to cubic at 2370^{o}C. These transformations are accompanied by large volume changes, which when constrained, as is the case with TBC applications, lead to very large stresses, likely resulting in failure.

Stabilizing the zirconia so that it reduces the severity of these transformations can be done by doping it with various oxides [6,7]. Yttria has emerged as the ideal dopant because it prohibits the zirconia from transforming from the tetragonal to monoclinic phase, which is accompanied by a 4% volume reduction. The metastable tetragonal (t) phase of zirconia, which is formed on rapid cool down of the coating after doping with yttria, has the highest fracture toughness of any form of zirconia. The metastable t phase, however, can transform to the monoclinic phase under applied stress. However, if the zirconia is allowed to cool in a certain manner after forming, a non-transformable tetragonal (t') phase will form, which retains the high fracture toughness and will not transform under stress [7]. The amount of t' phase present is maximized with about 8 weight percent yttria, so the material used most often for deposition of the top coat in TBCs is either 7 or 8 wt. % t' yttria stabilized zirconia (7YSZ or 8YSZ).

1.1.1.1 Deposition of the Top Coat

Although other techniques exist, the two preferred methods for depositing YSZ onto a substrate are by air-plasma spraying (APS) and electron beam physical vapor deposition (EBPVD). These two methods are most widely accepted by industry due to their efficiency, reliability, and the resulting microstructures they permit. EBPVD YSZ is often preferred to APS YSZ because it is typically more durable and its failure life more predictable, due to a more consistent microstructure. The underlying bond coat surface can be smooth, and the grains of YSZ form in a columnar manner perpendicular to the surface, providing good strain tolerance in operation. The microstructure of an EBPVD

coating is shown in Figure 1.2. However, EBPVD involves high costs in capital, in operation, and in time to produce the coating, so it is often reserved for the more critical components of the engine, such as the first stage turbine blades. APS YSZ, on the other hand, is a faster and more robust process, allowing for greater versatility in processing parameters. The process can be configured to various components in relatively little time compared to EBPVD. The resulting microstructure of APS YSZ typically contains 15-25% porosity [5] in the form of 'splat boundaries', providing a reduced elastic modulus and improved strain tolerance compared to fully dense YSZ. The porosity lays parallel to the surface of the coating in APS YSZ, rather than perpendicular as in EBPVD. The result is that APS YSZ enjoys a lower thermal conductivity than EBPVD YSZ, but its strain tolerance is less. The microstructure of an APS coating is shown in Figure 1.3. Unlike EBPVD coatings, APS coatings require a rough bond coat surface for adhesion. The undulation of the bond coat surface induces out-of-plane tension in the YSZ during thermal cycling which can be detrimental to the life of the coating. Furthermore, the randomness of the bond coat surface geometry gives rise to a wide range of coating life. This inherent uncertainty is largely what limits APS YSZ coatings to non-critical applications.

Typical industrial YSZ for APS application begins as a powder and is injected into a high velocity flame coming from a plasma gun. The plasma gun works by ionizing high velocity carrier gas (usually argon and hydrogen or nitrogen and hydrogen) passing through a DC arc inside the gun, turning it into a plasma. The resulting plasma jet reaches temperatures of up to 6000-12000^{o}C [8], melting the YSZ powder and propelling

it towards a substrate. When the molten YSZ impacts the substrate it cools, creating a 'splat'. The final coating is a multitude of these splats, creating the characteristic splat boundaries which make up the APS YSZ microstructure. A drawing of the APS process is shown in Figure 1.4.

1.1.2 Bond Coat

The primary purpose of the bond coat is to act as a reservoir that delivers supplies of aluminum to the bond coat/top coat interface in order to block the oxygen that passes through the top coat, turning it into α-Al_2O_3 (TGO) and protecting the superalloy from oxidation. The bond coat used with EBPVD top coats is usually a platinum-aluminide diffusion coating, applied by pack cementation or chemical vapor deposition (CVD). Pt has long been known to improve EBPVD coating life, and recent evidence shows it promotes Al diffusion towards and Ni diffusion away from the bond coat surface, giving increased preference to the growth of stable α-Al_2O_3 [9]. Bond coats used with APS top coats are generally MCrAlY coatings (the 'M' indicating a variable element, usually Ni, Co, Fe or a combination), produced by APS or low-pressure-plasma spray (LPPS). A good amount of latitude can be taken in choosing the composition of the MCrAlY bond coat. Yttria is added to prevent sulfur from gathering at the bond coat/TGO interface, which can lead to TGO detachment, although the mechanism by which this takes place is still being investigated [36]. Chromium is often included to enhance the hot-corrosion resistance of the bond coat, although too much added can lead to the formation of Cr rich phases in the bond coat and the formation of

non-α-oxides in the TGO. Cobalt can also be added to improve hot-corrosion and oxidation resistance, but it suffers from poor ductility. Aluminum, whose main job is to exist in a sufficient presence for the stable conversion of oxygen to Al_2O_3, also reduces the ductility of the bond coat. To hedge the reductions in ductility caused by Co and Al, nickel is sometimes added, which promotes ductility.

The other job of the bond coat is to improve adherence between the top coat and the substrate. The stable growth of TGO on the bond coat provides an interface for ceramic to ceramic adhesion. Also, since the thermal expansion coefficient of the bond coat lies between that of the top coat and the substrate, the strain that would otherwise be imposed on the coating is somewhat cushioned, although only in certain areas, like edges, is this effect more than negligible, due to the small thickness of the bond coat compared to the substrate. Furthermore, MCrAlY bond coats provide the undulating surface necessary for adherence of APS top coats.

MCrAlY can also be subject to a phase transformation as the aluminum concentration decreases due to the growth of Al_2O_3. For instance, NiCoCrAlY contains large regions of the β-NiAl phase. As the TGO thickens, the concentration of β-NiAl in the bond coat deceases and the concentration of its byproduct with oxygen, γ'-Ni_3Al, increases according to

$$3NiAl + \frac{3}{2}O_2 \rightarrow Ni_3Al + Al_2O_3$$

This reaction implies an associated volume change within the β-NiAl phases of the bond coat. If the entire bond coat were composed of β-NiAl, the associated bond coat

volumetric shrinkage due to 100% aluminum depletion would be 36.97%, which would certainly have an effect on the stresses in the YSZ.

1.1.3 Thermally Grown Oxide

The TGO is a necessary layer of a TBC system, providing an oxidation barrier for the underlying component, as noted above. Unfortunately, it is also the TGO that is the main driver of failure in both types of TBCs: APS and EBPVD. Oxygen from the environment moves through the YSZ top coat, either through connected porosity or directly through the YSZ (ZrO_2 has a very high ionic diffusivity, basically rendering it "oxygen transparent") [5]. Upon reaching the top coat/bond coat interface, the oxygen reacts with outwardly diffusing aluminum to create a thin layer of Al_2O_3. The layer of Al_2O_3 has a very low oxygen diffusivity, so the rate at which oxygen can penetrate the TGO layer is slower than the rate at which Al can diffuse up to meet it, creating a situation where there will always be enough Al for the O_2, ensuring stable growth for the TGO layer. Because the rate at which oxygen finds its way to the bond coat surface slows as the TGO thickens, the rate at which the TGO thickens also slows, so the thickness can be described as a parabolic function of time, in agreement with experiments (ref).

Although the stable TGO, α-Al_2O_3, is the most likely oxide to form, growth of other non-α-Al_2O_3 is possible. These can form during the early stages of growth when oxygen activity at the bond coat surface is at a maximum, and also in later stages of growth in areas where the Al has been depleted. A non-α-Al_2O_3 oxide may have a much

higher diffusivity than α-Al_2O_3, allowing it to thicken quickly, accompanied by large growth strain. Also, a non-α-Al_2O_3 oxide may have an undesirable mechanical property, such as a low fracture toughness, that proves to be a weak link during operation. For these reasons, the bond coat composition and the initial layer of TGO growth are often noted as the most important factors in a TBC system.

1.2 Failure Modes in APS TBCs

APS and EBPVD coatings display completely distinct failure mechanisms due to differences in the YSZ microstructures, chemical composition of the bond coats, and bond coat surface morphologies. The major generality that can be made between the two types of coatings is that while the EBPVD failure plane is most often located at the TGO/bond coat interface (Figure 1.5), the APS failure plane is primarily found in the top coat above the YSZ/TGO interface [5,7,10] (Figure 1.6). Since this study is limited to APS TBCs, some of the more prevalent theories on failure modes in these coatings will be given in this section. While the following modes are considered to be responsible for the majority of the TBC failures, many exceptions exist.

1.2.1 Imperfection/Bond Coat Geometry Induced Failure

The argument for this failure mechanism is that out-of-plane stress, σ_{22} (see Figure 1.7), is responsible for propagating cracks in the YSZ that ultimately lead to large scale bucking. The basis for the argument is the observation that regions of tensile stress develop above bond coat asperities upon cool down of the TBC. The stresses can

be explained by representing an asperity as a three-layer sphere (BC/substrate, TGO, and top coat) imbedded in an infinite material [11,12]. A sphere with the top coat at the core represents a 'valley', while a sphere with the BC/substrate at the core represents a 'peak', as shown in Figure 1.8. The YSZ top coat has a thermal expansion coefficient somewhere between the BC/substrate (the highest) and the TGO (the lowest). When thermal strains are applied to mimic cooling to room temperature, the model reveals the well-known result that when the TGO is thin, radial stress at the TGO/top coat interface is tensile for the peak and compressive for the valley. When the TGO thickness passes a threshold, the stress state becomes reversed. Applied to a coating, this would mean that, early on, cracks will be initiated over peaks due to a tensile σ_{22}, and once the TGO reaches a certain thickness, the tensile region will shift and the cracks will be able to coalesce. When a crack reaches a certain diameter, the large in-plane compression in the YSZ upon cool down will cause the detached coating to buckle [10]. Finite element modeling of two-dimensional interfaces, with bond coat asperities typically modeled as sine waves, have confirmed that the stress in the YSZ does undergo a transition in sign at a certain TGO thickness, dependent on the amplitude and wavelength of the undulation [13,14]. Particularly, it was noted that stress transition takes place the fastest for intermediate amplitude roughness [14]. Another general finding is that higher curvatures lead to higher stresses, but they dissipate rapidly into the surrounding TBC. On the other hand, lower curvatures lead to lower stresses, but with greater range. However, until recently, much of the past work on thermal barrier finite element

modeling failed to include the stress associated with TGO growth, which can significantly alter the stress above the interface [15].

The available work that does account for continuous TGO growth is contrary to the work that considers discrete values of TGO thickness [15,16]. Specifically, models showed that continuous TGO growth induces tension above the valleys and compression above the peaks, indicating that the stress in the YSZ due to growth strains in the TGO outweighed stress due to thermal mismatch alone. Currently, the general consensus is that the residual stress above the interface, when the YSZ is considered elastic, is a combination of stress from thermal mismatch and from TGO growth.

1.2.2. TGO Strain Energy Release

This failure mechanism theory is similar to the imperfection/surface geometry failure mechanism theory, in that the ultimate drivers of failure are TGO growth and thermal mismatch, but it differs by assuming that the TGO itself, rather than the geometry on which the TGO sits, is the primary cause of failure [17]. As the system cools, the thin-film TGO experiences a large in-plane compression and a corresponding increase in strain energy density, which is most readily relieved by lengthening in the out-of-plane direction, causing tension normal to the interfaces [10]. As the TGO displaces out-of-plane, the highest regions of tension develop at peak locations between the TGO and bond coat, which may cause debonding. Alternately, the debonding may occur at the raised bond coat grain boundaries in EBPVD TBCs [17]. Once the critical flaw is initiated, the strain energy release rate of the crack is basically governed by the

TGO, whose strain energy grows as the thickness of the TGO increases. When the energy release rate exceeds the interface toughness, the crack propagates. Since this mechanism does not require an initially undulated bond coat surface and failure at the TGO/bond coat interface is its characteristic, it is most often associated with EBPVD failure [17]. However, micrographs of cracked APS TBCs, such as the one displayed as Figure 1.9, often show crack excursions through the TGO which travel along the TGO/bond coat interface for a way, eventually linking up again with primary failure plain in the YSZ. This is most often observed at asperity peaks, which is consistent with this failure mechanism.

1.2.3 Thermal Gradient/Heat Flux Induced Failure

Thermal barrier coated components have the possibility of seeing very high thermal gradients in some locations of the engine. These gradients can be higher than what is possible to replicate during burner rig or furnace testing. Experiments using high heat flux lasers give evidence to another type of failure mechanism caused by these large thermal gradients [18-21]. The high heat flux gives rise to a thermal gradient in the coating. Since the material at the surface of the coating and in the center of the heat flux distribution is the hottest, it expands the most, but is constrained by the slightly cooler material beneath it and around it. It has been shown that the compressed YSZ in the gradient region relaxes away some of its stresses at the very high temperatures, and upon cooling, goes into in-plane tension, causing vertical cracks that begin at the surface and progress inward. It has been observed that these “mud splat”

cracks sometimes give rise to horizontal interface cracks as they near the YSZ/bond coat interface, which eventually coalesce with themselves or any other interface cracks present due to other mechanisms to cause failure.

1.3 Life Prediction Methods for APS TBCs

The initiative to create life prediction models was largely funded by NASA in the 1980s and included participation from major engine manufacturers [23-27]. Since then, many life prediction schemes have emerged in the literature for both APS and EBPVD TBCs. Many of the models for EBPVD include, in one form or another, the technique of photoluminescence piezospectroscopy (PLPS) which allows measurement of the residual stress in the TGO. PLPS works in a large part due to the columnar microstructure of EBPVD coatings. It fails in APS coatings due to the lamellar splat microstructure, which lies flat on top of the TGO. Because PLPS methods can't be used on APS coatings, and since this study doesn't consider EBPVD coatings, only a selection of models developed for APS coatings will be presented. Most of the life prediction models for APS TBCs can be separated into two groups: mechanical strain based models and fracture mechanics based models.

1.3.1 Mechanical Strain Based Models

A life prediction scheme was proposed by Miller in 1984 under the hypothesis, going on experimental evidence, that coating life was controlled by cycle duration and total time at temperature [24]. The model is based on an effective strain, ε_e, which is

comprised of strains due to thermal mismatch and oxide growth. The cycle duration effect is captured by the cyclic tensile radial strain, ε_r, caused by thermal mismatch. The total time at temperature effect is realized through bond coat oxidation, or TGO growth, measured as specific weight gain, *w*, of the sample. Miller assumed these combined to promote slow crack growth close to the interface. He defined N_{fo} as the number of cycles to failure, N_f, in the absence of oxidation ($w=0$), and w_c as the critical weight gain to cause failure in one cycle ($N_f=1$). He also reasoned that there must be a strain, ε_f, which would cause an unoxidized sample to fail in one cycle. Assuming the effective strain increases with specific weight gain by some power, *m*, leads to the formula

$$\sum_{N=1}^{N_f}\left[\left(1-\frac{\varepsilon_r}{\varepsilon_f}\right)\left(\frac{w_N}{w_c}\right)^m+\frac{\varepsilon_r}{\varepsilon_f}\right]^b=1,$$

where w_N is the weight gain after the *N*th cycle, *b* is a constant that depends on crack growth, and *m* is a constant that characterizes the relationship between effective strain and weight gain. The sample fails when the summation equals or exceeds 1 [24]. Miller's model correlated well with experiments, however he considered one coating at one temperature (1100^{o}C).

After finding that a combination of the normal and shear strain ranges associated with a thermal cycle correlated well with experimental failure lives, Hillery, Pilsner, McKnight, Cook, and Hartle (1988) proposed a life prediction model in the form: $N_f = f(\Delta\varepsilon_{rr}, \Delta\varepsilon_{rz})$ [25]. They correlated the strain ranges of a thermal cycle, calculated by way of a nonlinear finite element routine, to their experimental results, giving the number of cycles to failure, N_f, by the formula

$$0.135N_f^{-0.486} = \Delta\varepsilon_{rz} + 0.4\Delta\varepsilon_{rr}$$

where r is the in-plane direction, z is the out-of-plane direction (axisymmetric button specimens), and the deltas refer to the range in a stabilized thermal cycle. The strains for the model were probed at the "maximum severity location", or the edge of the coating (the top coat in their model was beveled at the edge, reducing it to zero thickness), and all the experimental samples failed at the edge, so they declared their model to describe life prediction for edge induced failure only.

In 1989, DeMasi, Sheffler, and Ortiz proposed a life prediction method that again attempted to combine the effects of cyclic phenomena and oxidation effects [26]. They used a Manson-Coffin type relationship relating the number of cycles to failure, *N*, to the inelastic out-of-plane strain range in the top coat for a given cycle, $N = A(\Delta\varepsilon_i)^b$. Using the inelastic strain range that causes failure in a single cycle, $\Delta\varepsilon_f$, as a condition on this equation, the proportionality constant, *A*, becomes $1/\left(\Delta\varepsilon_f\right)^b$. The expression for $\Delta\varepsilon_f$ consists of the inelastic strain range causing failure in one cycle with no oxidation, $\Delta\varepsilon_{fo}$, and the inelastic strain range for the cycle, $\Delta\varepsilon_i$, combined so they scale with oxide thickness, δ:

$$\Delta\varepsilon_f = \Delta\varepsilon_{fo}(1 - \frac{\delta}{\delta_c})^c + \Delta\varepsilon_i(\frac{\delta}{\delta_c})^d$$

where δ_c is the critical oxide thickness causing failure in one cycle. δ is calculated using a parabolic growth law, taking elapsed time and temperature into effect through an Arrhenius equation. The model assumes Miner's rule to account for varying cycle history, so that the coating fails when

$$\sum_{i=1}^{N_f} \frac{1}{N_i} \geq 1.$$

During the materials testing phase of the project, the "mechanical properties of the bulk ceramic were shown to be highly uncharacteristic of classical ceramic materials" ([26] page 191). In particular, the coating showed strong creep response, sensitive fatigue life, and a highly non-linear stress-strain response in tension and compression (the present work makes use of a previously developed viscoplastic constitutive model for the ceramic which was fitted to the material data from this report [28]). With these material properties (excluding the asymmetric tensile-compressive yield stresses), they used a non-linear finite element routine to calculate the inelastic strain range in the top coat for various cycles, and the inelastic strain range was considered to be the largest width of the resulting stress-strain hysteresis loop. Meir, Nissley, and Sheffler (1991) expanded this work to include EBPVD coatings [27].

EPRI produced a model (2006) that attempts to combine oxidation kinetics, thermal mismatch, sintering, geometry effects, and coating thickness to predict coating life [29]. The model multiplies the number of cycles to failure, N_f, raised to a power, by the elastic stress range of the coating during a thermal cycle and equates it to a time dependent fatigue strength, which is further discounted by the accumulated oxide thickness. The final form of the model is

$$N_f = \frac{\sigma^*_{TBC}}{\Delta\sigma_{TBC}}\left[1 - \left(\frac{\delta}{\delta^*}\right)^c\right]^{1/b}$$

where $\Delta\sigma_{TBC}$ is the stress range during a cycle, σ^*_{TBC} is the time dependent fatigue strength of the coating, δ^* is the critical oxide thickness, and *c* and *b* are constants. δ is

assumed to grow parabolically, and is given in the form of a typical Arrhenius equation. The top coat is assumed elastic, so $\Delta\sigma_{TBC} = E(t)\Delta\varepsilon_{TBC}$, where the time dependence of the elastic modulus attempts to account for sintering by letting $E(t) = E_o(t/t_o)^m$, where E_o is the Young's modulus of the coating at t_o and *m* is a sintering exponent. The strain range, $\Delta\varepsilon_{TBC}$, is assumed to be due to the thermal mismatch between the top coat and the substrate, given by

$$\Delta\varepsilon_{TBC} = \left(\alpha_{0,SS} - \alpha_{0,TBC}\right)(T_2 - T_1) + \frac{1}{2}\left(\alpha_{1,SS} - \alpha_{1,TBC}\right)(T_1^2 - T_2^2)$$

where $\alpha = \alpha_0 + \alpha_1 T$ (temperature dependent α) and T_1 and T_2 are the minimum and maximum temperatures in the cycle, respectively. Finally, the time dependent fatigue strength, σ^*_{TBC}, is given as

$$\sigma^*_{TBC} = \sigma^*_o \exp\left[-a_1\left(\frac{h}{R_i}\right)\right]\left(\frac{t}{t_o}\right)^{-n}$$

where *h* is the coating thickness, R_i is the radius of the geometry, and σ^*_o, a_1, and *n* are constants. Although the EPRI model correlates reasonably well with experimental results, it is highly empirical and may not contain a provision that takes into account the effect of cycle duration on life.

1.3.1. Fracture Mechanics Models

In the past decade, there has been much work to describe the interface geometry induced, and other types, of failure using fracture mechanics principles. For instance, Evans, Hutchinson, and He (2002) proposed a life prediction method based on this failure mechanism [16]. In their model, they considered continuous TGO growth, an

elastic-perfectly plastic TGO and bond coat (temperature dependent yield stress), and an elastic anisotropic top coat (also temperature dependent). Using stresses obtained from their finite element model, they calculated the energy release rates for different crack lengths originating in the tensile regions above the valleys. As the crack length increased, the energy release rates at first increased, then decreased as they encountered the compressive regions above the peaks, and finally increased again on the other side of the asperity. The minimum energy release rate, G_{min}, was encountered when the crack tip was in the compressive zone (compressive when crack-free) above the peak. G_{min} was tracked as the overall stress state increased due to TGO growth, and the coating was considered "failed" when G_{min} reached the fracture toughness of the YSZ. This work resulted in a formula for the number of cycles to failure:

$$N_f = N_o + \frac{\Gamma_{tbc}}{E_{tbc} L (\Delta\alpha \Delta T)^2 \kappa}$$

where Γ_{tbc} is the fracture toughness of the YSZ, L is half the wavelength of the asperity, and κ and N_o are constants. The formula is system specific as the constants depend on assumptions about TGO growth and TGO/bond coat material properties. More importantly, the formula does not offer a way to include the effect that cycle duration has on coating life.

Busso et al (2001) proposed a damage-mechanism based life prediction model using stress input derived from a continuum mechanics based constitutive model of the bond coat implemented in a finite element routine [22,23]. In this model, out-of-plane stress, T_{22}, depends on oxide growth, creep, sintering, and the geometry of the interface. The accumulation of damage, D, with number of cycles, N, is given as

$$\frac{dD}{dN} = D^{\left[1-C\left(\frac{T_{22\,max}}{\sigma_{co}}\right)\right]^{(q-p)}} \left[\frac{T_{22\,max}}{F_o(1-F_1 T_{22\,max})}\right]^p$$

where $T_{22\,max}$ is the maximum stress at a location during a thermal cycle, σ_{co} is the initial cleavage strength of the coating, and *p*, *q*, *C*, F_1, and F_0 are material dependent constants. The model is based on the assumption that when D=1, the stress is roughly the cleavage strength of the material. When *D=1*, the coating is considered failed. The model predicts that cycles with long dwell times fail mostly due to sintering and oxidation, and models with short dwell times fail primarily due to the cyclic effects of damage accumulation. A benefit of the model is that the stress input gives a physical basis to the model, and it seems to have the capacity to predict effects due to cycle duration, but it is relatively complicated and requires finite element analysis to obtain $T_{22\,max}$.

Beck et al (2008) proposed a fracture based life prediction model that hinged on the observation that the maximum crack length above the interface increased proportionally with TGO thickness up to a critical thickness, after which it increased rapidly to failure [30,31]. This critical thickness was found to be roughly ¼ of the average peak-to-peak roughness of the bondcoat. The maximum crack length at this thickness was observed to be about ½ the wavelength of the bondcoat peaks. This observation led to the separation of the coating life into two phases, an incubation phase and a propagation phase. During the incubation phase, the crack length was calculated as $a = 2\lambda d/R$, where λ is the average wavelength of the bondcoat, d is the TGO thickness (calculated from an Arrhenius equation), and R is the average bondcoat

roughness. In the propagation phase of coating life, the crack length is calculated from two separate energy release rates, the energy release rate due to thermal mismatch, G_{el}, and the energy release rate due to stresses imposed by thermal growth, G_{TGO}. G_{el} includes the thermal stresses caused upon cool down under a ductile-to-brittle transition temperature (DBTT). Above the DBTT, stresses are assumed to relax completely. G_{TGO} takes into account stresses due to both thickening and lateral TGO growth, assuming constant tension above the interface. The crack length is then calculated as

$$\frac{da}{dt} = A\left(G_{el} + \frac{1}{b}G_{TGO}\right)^{m}$$

where b and m are constants. The model also takes into account sintering through a time dependent elastic modulus. The coating is considered failed after the crack reaches a critical length of 6 mm. The model was able to correlate to experimental failure lives to within a factor of 2.

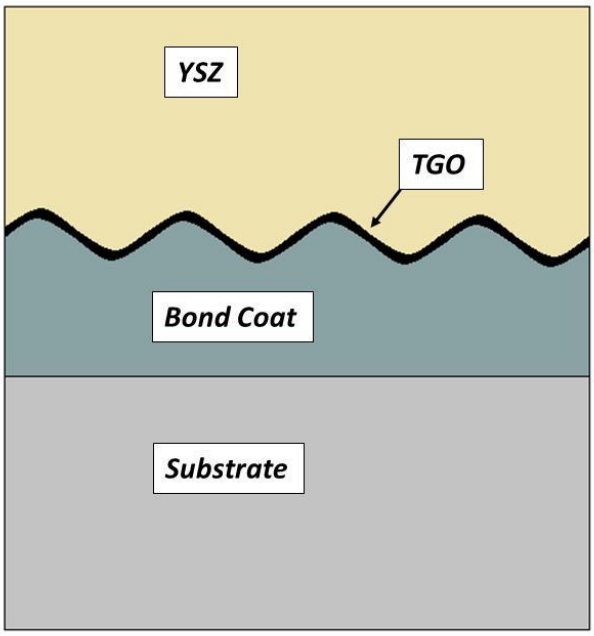

Figure 1.1 – The four layers of a TBC: YSZ topcoat, thermally grown oxide (TGO), bond coat, and substrate (component)

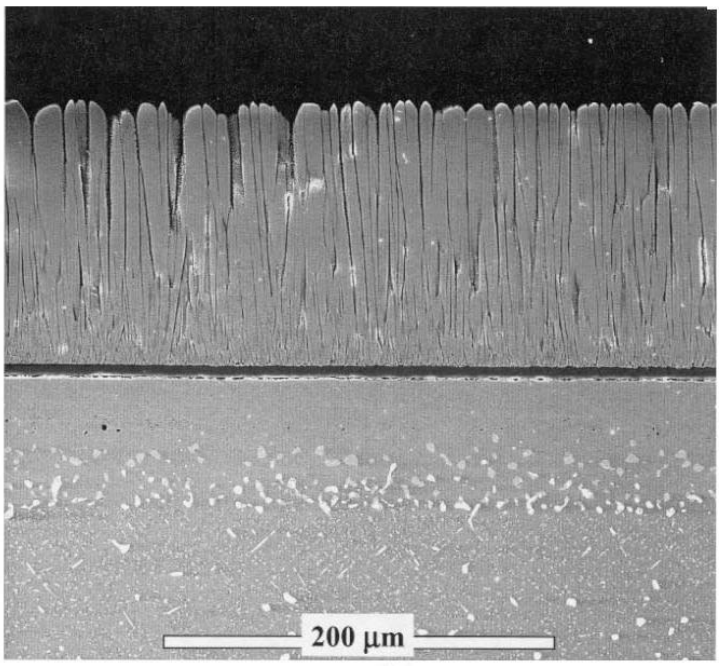

Figure 1.2 – Microstructure of a typical EPBVD thermal barrier coating [35]

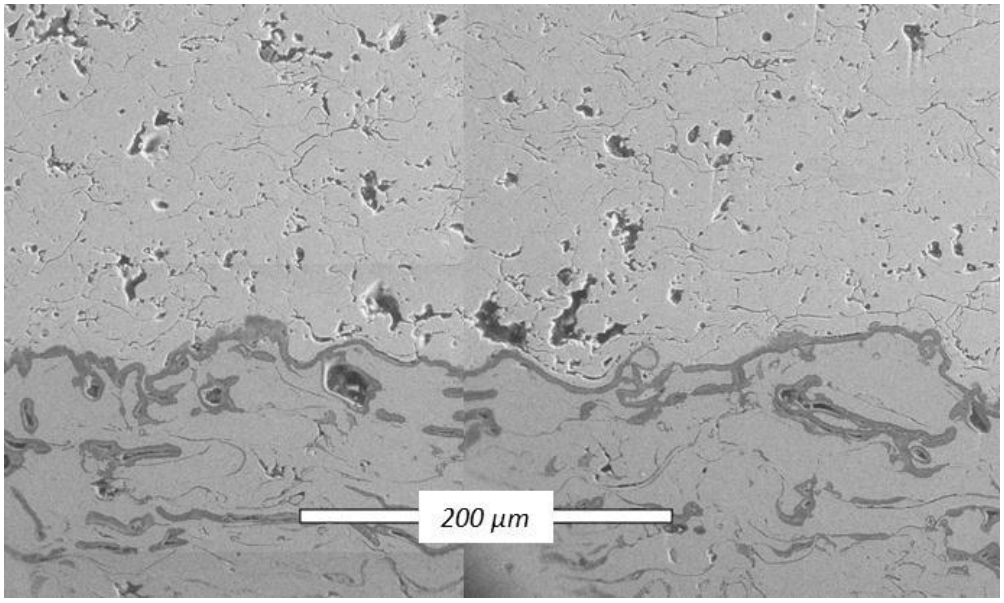

Figure 1.3 – Microstructure of a typical APS thermal barrier coating

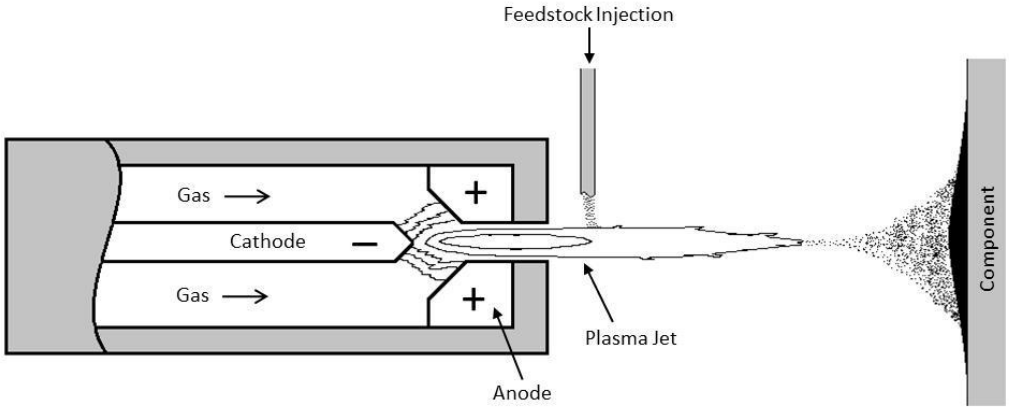

Figure 1.4 – Schematic showing the APS deposition process

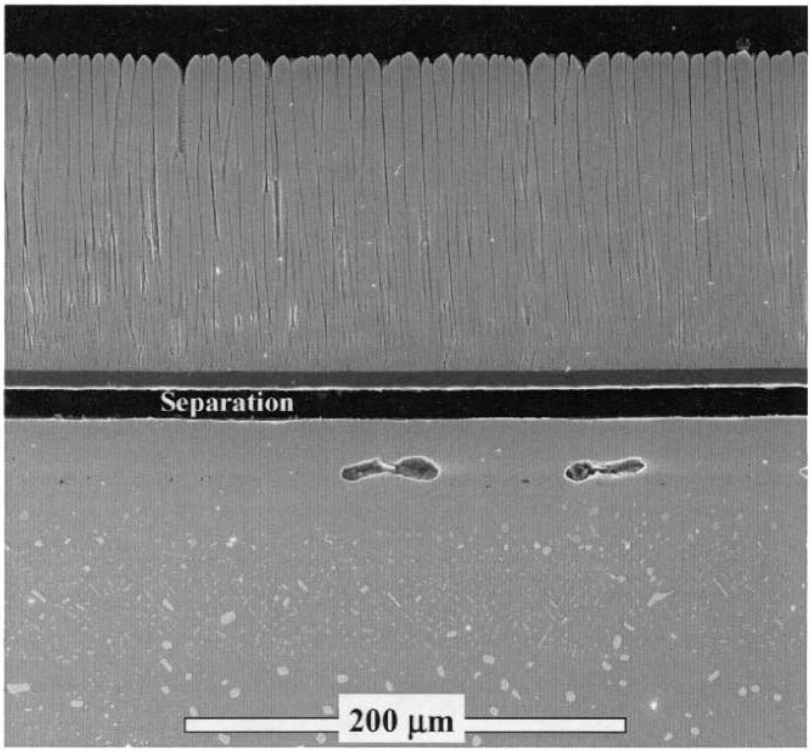

Figure 1.5 – Failure at the TGO/bond coat interface in an EBPVD TBC [35]

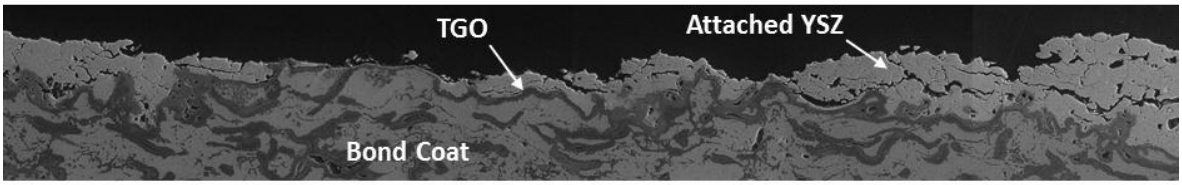

Figure 1.6 – Failure just above the YSZ/TGO interface in an APS TBC

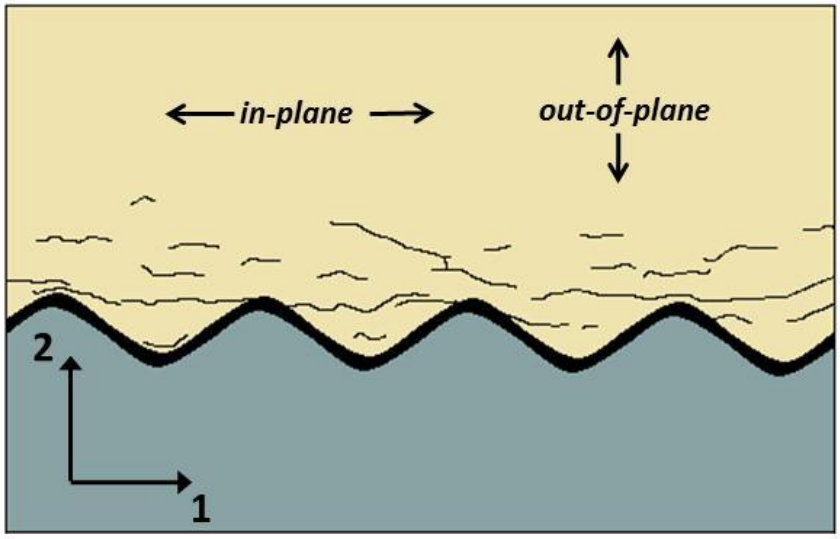

Figure 1.7 – Coordinate and nomenclature conventions

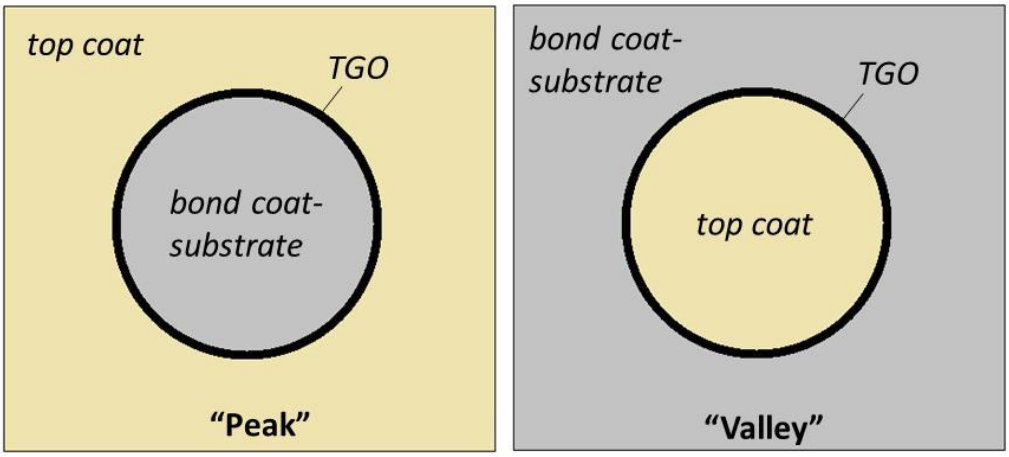

Figure 1.8 – "3-spheres model": simplified analysis of the interface stress state by considering a sphere and shell embedded in an infinite matrix

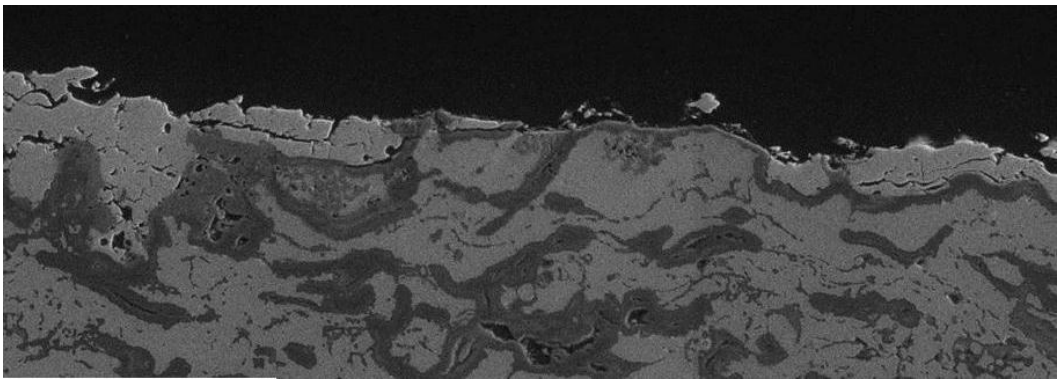

Figure 1.9 – Shows an excursion of the failure plane from the YSZ through the TGO and back to the YSZ

2. Experimental Procedure

2.1 Oxidation Testing

2.1.1 Oxidation Test Samples

One inch square test samples were used for the uniform temperature oxidation testing, with the purpose of growing and measuring the TGO in a controlled environment. The samples consisted of the three basic thermal barrier coating layers: substrate, bond coat, and top coat. A typical NiCoCrAlY bond coat with a thickness of about 0.0075 inches (190.5 µm) was deposited on a PWA 1455 Ni-based superalloy substrate having a nominal thickness of 0.125 inches (3175 µm). A 0.010 inch (254 µm) thick 7 wt% YSZ air-plasma sprayed top coat was then deposited on top of the bond coat, bringing the total nominal thickness of the sample to 0.1425 inches (3619.5 µm). The bond coat is grit blasted to improve top coat adhesion, resulting in an undulating bond coat/top coat interface. A schematic of the test sample is shown in Figure 2.1.

2.1.2 Furnace Cycling

The furnace used in this test was a CM, inc. (Bloomfield, NJ) elevator-type furnace with a Zirconia platform. A Eurotherm 2404 controller regulates the temperature of the furnace based on a thermocouple welded to the back side of a dummy sample (superalloy disk), located at the center of the platform. A photo of the furnace and controller is shown in Figure 2.2. To monitor the temperature, two additional thermocouples are attached to the elevator platform. One of these

thermocouples is exposed to the open furnace and located at the front edge of the platform, while another is insulated in Zirconia and located at the other front edge of the platform. The thermocouples were checked periodically to ensure agreement to within ±5 ˚C at steady state operation. To further confirm the accuracy of the furnace, another thermocouple was inserted into the upper chamber of the furnace halfway between the two rows of heating elements which line the side walls. This thermocouple also agreed with the others to within ±5 ˚C at steady state.

2.1.2.1 Cyclic Testing

Cyclic furnace tests were conducted at three temperatures, 2100˚F (1149˚C), 2000˚F (1121˚C), and 1900˚F (1093˚C). Three temperatures were necessary to obtain sufficient data to extract the activation energy for TGO growth from an Arrhenius equation relating TGO thickness to time and temperature. A cycle lasted 50 hours and 32 minutes, consisting of a ramp up to hold temperature (22 min), a hold at temperature (50 hrs), and a forced convection cooling (10 min). Figure 2.3 shows a schematic of this cycle. A 22 minute ramp up was deemed sufficient to keep the amount of temperature overshoot as the furnace approached the hold temperature to a minimum. Three samples were used in each of the three tests. After every 50 hours, a section of a sample was carefully cut, mounted, and polished, and the TGO was measured. The cyclic tests were run either to sample failure or until a sufficient amount of data had been collected to allow for calculation of the activation energy. To test the reproducibility of the results, a confirmation test was performed in which a

single sample was heated to 2100˚F in 50 hour cycles after an initial cycle of 150 hours to accelerate the test. The TGO thicknesses in the 2100˚F original test and the confirmation test agreed, ensuring the reproducibility of results. To rule out possible controller or data acquisition inaccuracy, an as-sprayed sample was placed in a tube furnace at approximately 2100˚F for 100 hours, and the TGO was measured. The TGO thickness of this sample agreed well with the samples cycled in the elevator furnace, ruling out furnace inaccuracy.

2.2 Sample Preparation

This section describes the techniques used to cut, mount, grind, and polish a sample before the cross section could be examined either by optical or electron microscope. All the techniques described in this section are standard metallographic preparation techniques.

2.2.1 Sectioning and Mounting

After every 50 hour cycle in the standard oxidation tests, a sample was removed and a square section was cut from it. The section was either 1 x ¼ inches or ¼ x ¼ inches, approximately. The 1 x ¼ inch section was preferred because it offered more cross sectional area for examination, but the ¼ x ¼ section was often used to conserve the amount of total remaining sample, especially in the low temperature (1900˚F) test. The sections were cut as to retain the square geometry and to minimize the number of cut edges on the intact sample to avoid premature failure. A photo of a sectioned piece

is shown in Figure 2.4. The samples were cut with a LECO VC-50 low-speed wet saw using a Buehler diamond wafering blade. The blade was made to rotate into the coating to avoid applying excessive outward force directly to the coating, which could cause the top coat to crack or separate.

The cut sections were then mounted in Allied, inc. EpoxySet, which consisted of a mixture of 100:12, resin to hardener. The mixture was poured into a standard circular metallographic mold and allowed to cure for eight to ten hours. The epoxy effectively binds the sample together so no damage can be done during grinding and polishing. Also, during subsequent examination, the presence of an epoxy filled crack gives good evidence that the damaged region was not caused by grinding or polishing.

2.2.2 Grinding and Polishing

After curing, the mounted samples were hand ground and polished on either a Struers RotoPol-22 or a Buehler Beta, both of which are rotating disk polishing machines. Disposable LECO silicon carbide grinding disks were used in a 120, 180, 320, 600, 800, 1200 progression of grit sizes in order to remove a progressively finer amount of material from the sample. Water was used as a coolant throughout the grinding stage. Polishing of the samples was done with LECO diamond grit polishing suspension. Multiple Struers MD-Dac satin-woven acetate polishing pads were used, each pad being dedicated to a particular grit suspension. The progression of grit size was: 9 µm, 6 µm, 3 µm, 1 µm, which refers to the average size of the diamond in suspension. The samples were rinsed with deionized water between stages to reduce the possibility of

transferring any residual grit to a pad dedicated to smaller grit sizes, which could lead to scratches in the surface of the sample.

In the cases where a spalled or otherwise failed cross section was to be prepared for examination, for example the engine-failed specimens, the section was mounted in epoxy first and then carefully cut, ground, and polished in order to eliminate further damage of the sample that could otherwise occur during cutting.

2.3 Failure Characterization

After preparation, samples were examined in several ways as a means to determine the failure mechanism in the particular type of sample. The sample types again were: engine-failed combustor liner samples, oxidation test samples, and a failed burner bar sample. In the oxidation test samples, both the TGO thickness and the evolution of the TBC/bond coat interface region in terms of rumpling and cracking was of interest.

2.3.1 Scanning Electron Microscopy

Polished cross section samples as well as some failure surfaces were examined by scanning electron microscope. Most often, the microscope used was a Philips ESEM 2020 (Environmental Scanning Electron Microscope). The ESEM introduces a small amount of water vapor at a controlled pressure into the microscope chamber, eliminating the need for a conductive coating to be applied to nonconductive materials, like YSZ. The ESEM is also equipped with a backscatter detector, which produces

greater contrast between heavy and light elements as well as greater topological contrast, and was used often in this study. Most of the failure characterization and all of the TGO measurements were performed on this microscope.

The ESEM also has the capability to determine the elemental composition of regions of the sample. This is made possible by an auxiliary EDAX CDU/SUTW Energy Dispersive X-ray system (EDX). EDX measurements were used to determine the composition of some failed surfaces and also in identifying some non-alpha oxides in the TGO.

In certain instances when the ESEM was being serviced or when higher resolution micrographs were required, a JEOL JSM-6335F cold cathode field emission SEM (FESEM) was used for sample characterization. Although the FESEM is capable of high resolution images, it operates in a vacuum, so non-conductive samples, like YSZ, must be coated with a thin layer of gold prior to evaluation, and all epoxy, which produces a vapor leading to attenuation of the electron beam, must be trimmed as far as possible. Since the extent of sample preparation was far greater for the FESEM, the ESEM was used as much as possible. In using both microscopes, copper tape was applied to bridge the non-conductive YSZ with the metal sample holder, helping to increase the conductivity, thereby increasing the resolution.

In addition to the electron microscopes, extensive use was made of optical microscopes in examining the larger scale characteristics of the samples as well as in making judgments about the quality of polishing.

2.3.2 X-Ray Diffraction

In some cases it was necessary to determine the composition of material on a larger scale where EDX is not appropriate, as in determining whether a thin layer of YSZ exists continuously on a failure surface. Discrete EDX measurements could only be made point wise and would miss many points, making it difficult to infer the composition of a large continuous area. X-ray diffraction was employed for making these large scale inferences. A Bruker D5005 diffractometer was used and the resulting diffraction pattern compared to a standard database of patterns.

2.4 Quantitative Measurements

2.4.1 Measuring TGO Growth

Cyclic isothermal furnace cycling tests were performed at three temperatures, 2100˚F, 2000˚F, and 1900˚F, for two reasons: to observe the failure mechanism under a uniform temperature loading and to quantitatively measure the rate of TGO growth. The TGO thickness measurements were taken after every cycle (50 hour cycles) and were made on the ESEM using the built-in measurement tool. Measurements were made locally within several larger spaced locations across the interface, in order to account for large scale spatial variations in thickness. For example, measurements on some sections were made near each edge and in the middle of the section. Larger cross sections (the 1 x ¼ inch sections), as well as specimens that demonstrated notably larger variations in thickness (the 2100˚F sections) required more locations to be included, up

to ten in some cases, while sections that demonstrated minimal variation required only three. Within each location, an average of 15 local measurements were made, spaced at least 50 microns apart, to average out the small scale spatial variation in thickness. The average thicknesses at all the locations across the section were again averaged to obtain the final TGO thickness for the section.

Difficulties arise in measuring the TGO thickness in air-plasma sprayed systems, predominately at the highest temperatures. A very messy interface composition in which the TGO thickness varies excessively can arise due to a combination of breakaway oxidation, areas of fast growing non-alpha oxides, and regions with excessive curvature of the bond coat surface. A concerted effort was made to take measurements only in areas in which the TGO appeared to be growing fairly uniformly, thus, the actual average TGO thickness of the section (which contains non-alpha oxides and areas of breakaway oxidation) was not measured, but rather the average TGO thickness if the TGO was grown uniformly was measured. Figure 2.5 shows the distinction between the regions.

2.4.2 Measuring Interface Tortuosity

Tortuosity of an interface can be defined as the ratio of the length of its curve to its straight line length. Tracking it gives a good quantitative measure of the severity of bond coat rumpling. The tortuosity was measured from about 10 micrographs which were combined to show a longer length of the interface, about 2500 microns. The measurements were performed manually with a pixel based computer measurement

program. That is, a line was drawn along the bond coat/TGO interface, and the number of pixels along that line was compared to the straight line length. As with measuring the TGO, the interface regions used for measurement were typical regions – exceedingly large local variations in tortuosity were not considered.

2.5 Finite Element Modeling

To examine the effects of loading history on out-of-plane stresses, a small scale model was built that includes all four layers of the TBC and takes into consideration bond coat roughness. A sine curve was used to represent the bond coat roughness primarily for consistency, because it is the most common representation in the literature, owing to the fact that the curve represents the true asperity shape reasonably well and can be parameterized to examine the effects of varying roughness. An amplitude and wavelength of 25 and 100 μm was used for all the cases (see Figure 2.6), representing an average roughness commonly observed experimentally and used in the literature. The general effects of varying the amplitude and wavelength have been studied, as noted in section 1.2.1, which is the reason only a single representative interface shape has been considered in this work. The only discrepancy is that the model really represents “troughs” in the thickness direction rather than realistic “bumps”, since the model is confined to two dimensions.

2.5.1 Mesh

The model was designed to represent a cross-sectional slice taken out of the middle of a flat plate. The width is half the sine curve wavelength, with symmetry boundary conditions on the left side and periodic boundary conditions on the right. The mesh is shown in Figure 2.7. Generalized plane strain elements (with rotation suppressed) were necessary to allow the layers to expand in the thickness direction, as shown in Figure 2.8. "Six-node quad" elements, or four-node quadrilateral elements with 2 incompatible modes, were used because some shear locking was observed at the peak and valley of the TGO layer when four-node quads were used. The two extra modes effectively allow the element to alleviate shear locking by bending like an eight-node quad; however, the interpolation of the displacements between nodes is still linear, as opposed to quadratic, resulting in constant strain across the element. It was deemed that the accuracy of the strains with suitable mesh refinement was sufficient, the increased computational cost of using 8-node quads being too great to justify a small improvement in accuracy. The Abaqus element used was CPEG4I, and the final mesh contained 174,700 displacement degrees of freedom [32].

2.5.2 Loading

All the models were run as static analyses. They were 'quasi-static' in the sense that the nonlinear behavior of the system was found by progressive iteration of static solutions using the standard Newton-Raphson technique and tracked using 'time' as a variable, but they did not involve accelerations or heat fluxes, which would have

required transient analyses. Temperatures, needed only to drive thermal strains, were dictated to the model rather than calculated from a field equation and boundary conditions, which would have required the use of coupled temperature-displacement elements. The temperatures were prescribed uniformly over the model in both the heating and cooling stages, roughly simulating a furnace test environment. A diagram of the temperature cycle is shown in Figure 2.9. The stress-free temperature of all the layers was taken to be 1000^{o}F for simplicity, which is commonly used in the literature [16]. Although the stress-free temperatures are critical when the stress state is driven by thermal expansion mismatch only, in the presence of morphologically driven events like TGO growth, the effects of the stress-free temperature were found to be subtle. The hold temperatures ranged from 1900^{o}F to 2100^{o}F, and the room temperature was taken to be 75^{o}F. The standard heat and cool times were taken to be 10 minutes each, while the cycle times varied from 2 to 200 hours. The initial heat time was set so that the rate matched the standard heat and cool rates.

The material properties used in the models can be seen in Table 2.1. Simplified, non-temperature dependent material properties for the TGO, bond coat, and substrate were used that were taken or averaged from a number of sources, including the literature [16]. For the linear elastic YSZ, a temperature dependent modulus that matched the modulus in the viscoplastic YSZ constitutive model was used for consistency.

2.5.3 Modeling TGO Growth

The effects of TGO growth were analyzed by imposing a growth strain onto the TGO elements via an irreversible 'dummy' thermal strain. The increment of thermal strain was based on the current value of TGO thickness, which was calculated throughout the loading history according to the differential form of an Arrhenius equation using constants measured from the data collected in the experimental aspect of this work. Lateral TGO growth, or growth along the interface length, was not taken into account. Since it was assumed that the TGO growth occurred only normal to the interface, the total thermal strain on the elements was applied orthotropically, so that the fraction of the total strain in the vertical and horizontal directions varied depending on element coordinates, which yielded a uniform thickness. The scheme was implemented into the Abaqus user-subroutine UEXPAN. The final thermal strain at each increment was corrected for by adding in the reversible 'real' thermal strain.

2.5.4 Modeling Rumpling

Bond coat rumpling was implemented into the model in a manner similar to TGO growth. It was assumed, primarily for the model simplicity, that rumpling manifests itself through bond coat amplitude change while the wavelength remains constant. The model tortuosity change was calculated based on the measured tortuosity change and converted to an amplitude. Assuming that it is the TGO growth which is ultimately responsible for rumpling [10,37], the modeled asperity was stretched from its initial to final amplitude in proportion to TGO growth, again accomplished by imposing a dummy

thermal strain, this time on the bond coat elements under the asperity. As in the case of TGO growth, the final thermal strains at each increment were corrected by the real thermal strain.

2.5.5 Modeling Al-Depletion from Bond Coat

As noted in section 1.1.2, NiCoCrAlY bond coats contain large phases of β-NiAl. As the TGO thickens, aluminum ions are drawn from these regions to react with the incoming oxygen, creating Al_2O_3. The byproduct of the reaction is a new phase of nickel-aluminum, γ'-Ni_3Al. The reaction can be written as

$$3NiAl + \frac{3}{2}O_2 \rightarrow Ni_3Al + Al_2O_3$$

So for every mole of TGO created, three moles of β-NiAl are transformed into one mole of γ'-Ni_3Al. Since the molar masses and densities are known for all the reactants, the volume change associated with the transformation can be calculated. The volumetric shrinkage associated with transforming a volume of 3NiAl to a volume of Ni_3Al was found to be 36.97%. Also, the aluminum from a volume of 3NiAl can create Al_2O in a volume ratio of 1:0.6037. Alternatively, these calculations can be done from knowledge of the reactants' lattice parameters.

When TGO is formed, the β-NiAl from where the aluminum was taken will transform into γ'-Ni_3Al and shrink. While it is hard to say exactly how the aluminum diffuses and from where, it's reasonable to think that initially it comes from close to the interface. A severe case would consist of a bond coat asperity made up entirely of β-NiAl, transforming into γ'-Ni_3Al as TGO was deposited on its surface. If the volume of

the TGO were known as a function of its thickness, the thickness at which the entire asperity has transformed to γ'-Ni_3Al could be calculated. Approximating the volume of the TGO as the length of a period of a sine wave times the thickness per unit depth, the volume was found numerically to be

$$Volume\ per\ unit\ depth \approx \frac{h}{L}(0.99827L^2 + 1.4167AL - 0.092789A^2)$$

where A is the amplitude, L is the wavelength, and h is the thickness. Using the volume of the TGO, the volume of the asperity (amplitude times wavelength), and the ratios of volumetric shrinkage, the thickness of TGO at which the entire asperity has been transformed (shrunk by 36.8%) can be calculated. For A=25 μm and L=100 μm (the parameters used in the model), the thickness is 11.207 μm. Assuming the volumetric shrinkage proceeds linearly with TGO thickness allows for the calculation of shrinkage strain as a function of TGO thickness.

The simulations in this thesis that account for bond coat shrinkage assume the most severe case, when the entire volume under an asperity is composed of β-NiAl and all the aluminum to create TGO comes from here. On the other hand, the least severe case would be that in which no shrinkage takes place, implying that all the aluminum comes from well below the interface. Like before, modeling bond coat volumetric shrinkage is accomplished by imposing dummy thermal strains on the bond coat through the user subroutine UEXPAN [33].

2.5.6. Viscoplastic YSZ Constitutive Code

2.5.6.1 Basis for the Model

It was noted in section 1.3.1 that testing on APS YSZ has shown material response uncharacteristic of traditional elastic ceramic materials. In particular, APS YSZ exhibits a nonlinear stress-strain response, observable even at room temperature, a very strong creep dependence on temperature, strain-rate dependence, and a compressive flow stress which is more than ten times greater than the tensile flow stress [28]. Figures 2.10 through 2.12 are material test results as reported by DeMasi et al highlighting some of these nonlinearities, taken from the materials testing phase of their report, "Thermal Barrier Coating Life Prediction Model Development" [26,28].

The viscoplastic constitutive model used for this work was originally developed by Janosik and Duffy in 1997 to model the nonlinearities associated with monolithic ceramics [34]. The model utilizes a Willam-Warnke yield surface, originally conceived to model concrete (Figure 2.13). In 2003, the model was modified by Xie, Walker, Jordan, and Gell to be non-associative, meaning the flow rule is derived from a slightly modified form of the yield function [28]. This removes a restriction on a model constant that would otherwise result in an unrealistic increasing volume expansion as the material is cycled between tension and compression. This volumetric expansion results from requiring flow increments to be normal to the yield surface, which is an unnecessary simplifying assumption of the original model [28].

The model was fit to the material data given by DeMasi et al for an air plasma sprayed TBC by using a genetic algorithm scheme to determine the material constants. The fit between the resulting model and the experimental data is shown in Figures 2.14 and 2.15 [28].

2.5.6.2 Implementation

The model has been previously written as an Abaqus user-material and is implemented through the user subroutine UMAT [33]. The only change that has been made to the code for the present work is the inclusion of twelve additional state variables (which don't enter into stress-strain response calculations) to allow for more detailed monitoring of the inelastic strain tensor. Specifically, the inelastic strain is broken down into a "hot" inelastic strain tensor (inelastic strain components accumulated when the temperature cycle is in the hold region) and a "cold" inelastic strain tensor (inelastic strain components accumulated when the temperature is below the hold temperature).

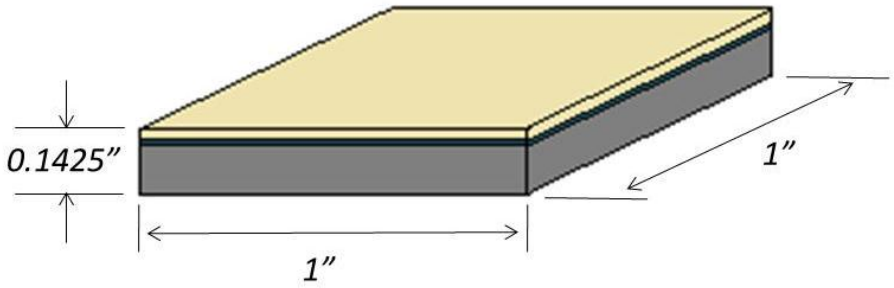

Figure 2.1 – TBC samples used in oxidation testing

Figure 2.2 – CM, inc. elevator-type furnace used in oxidation testing

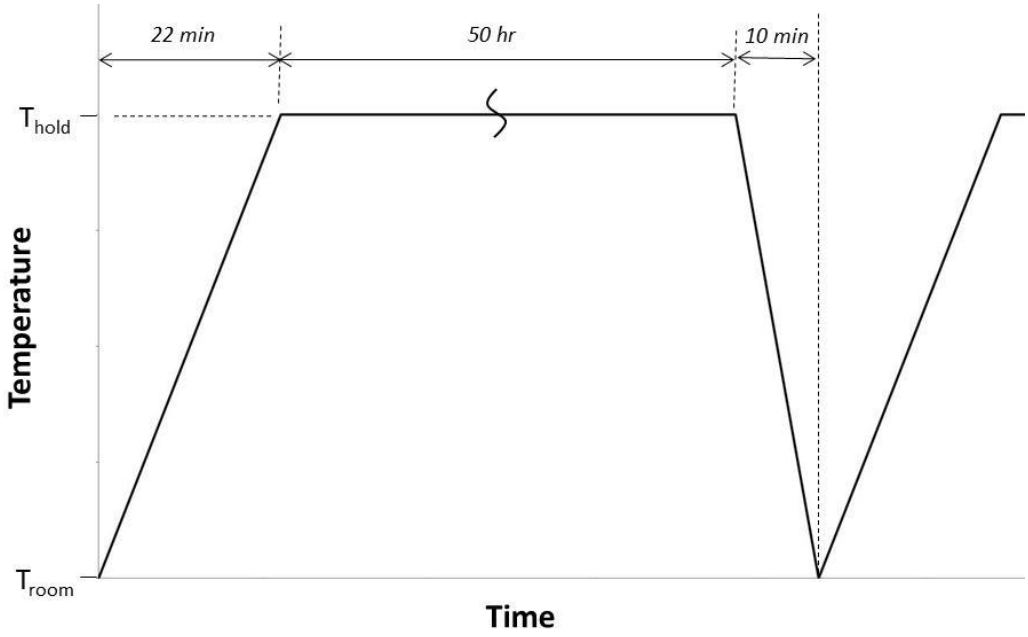

Figure 2.3 – Temperature cycle used in oxidation testing

Figure 2.4 – Photo of sectioned oxidation test sample after mounting (1/4 inch and 1 inch sections)

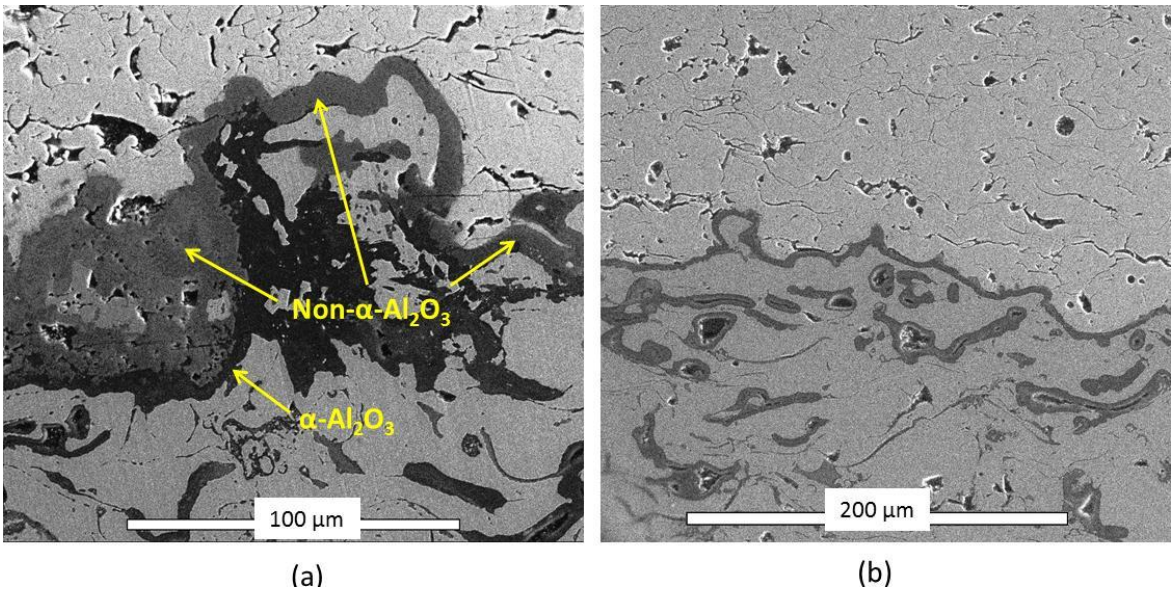

Figure 2.5 – (a) Interface region showing excessive non-α-oxide; measurements were not made in these regions; (b) Interface region showing continuous α-oxide growth; measurements were made regularly in these regions

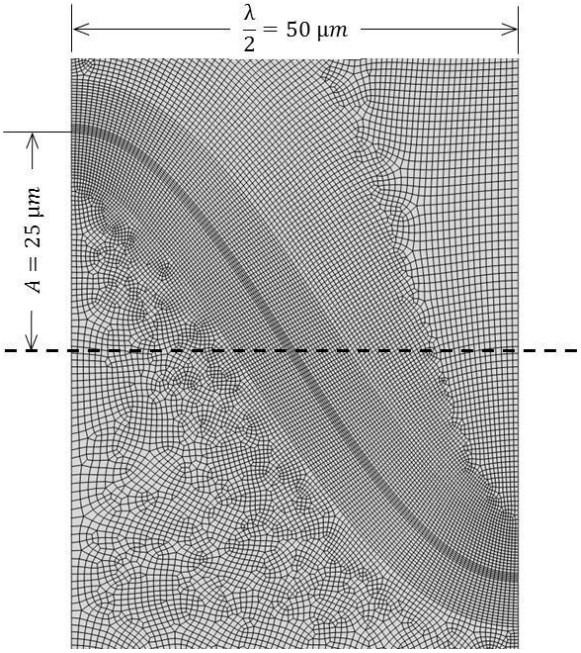

Figure 2.6 – Amplitude and wavelength used in models, representing a commonly observed geometry

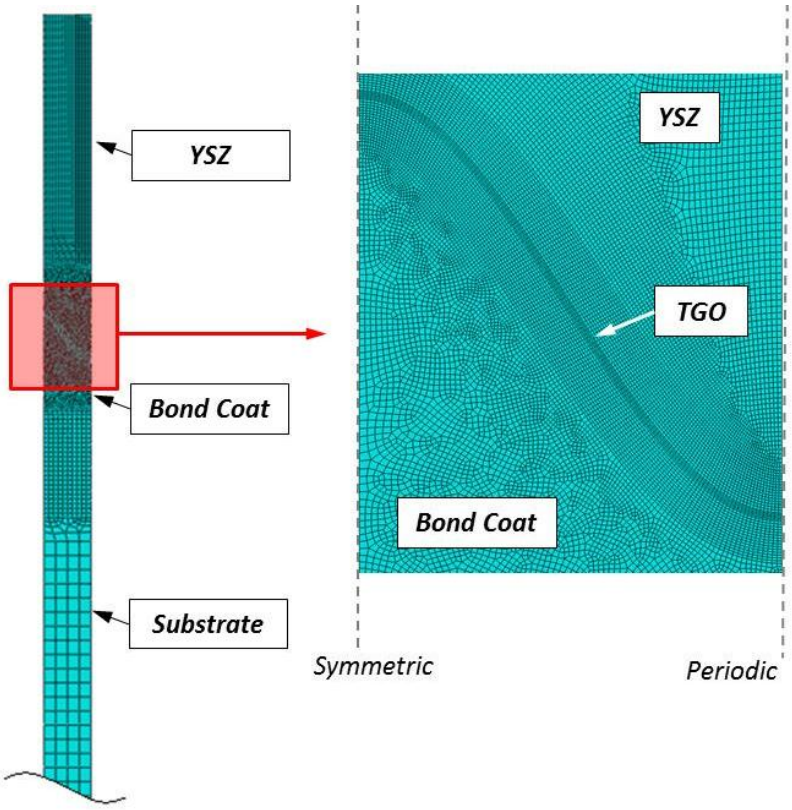

Figure 2.7 – The mesh used in most models and based on oxidation test sample geometry; mesh is 2D with symmetry and periodic constraints; 4-node generalized plane strain elements (with rotations suppressed) and incompatible modes were used

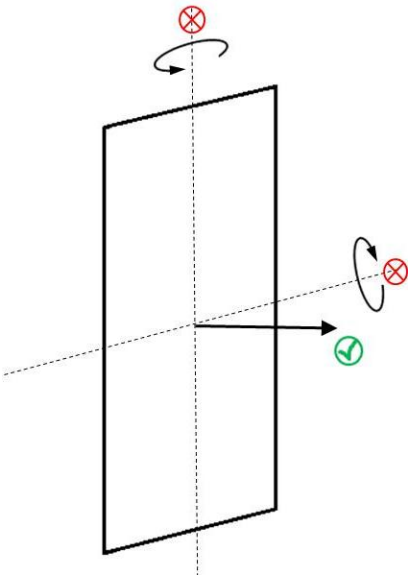

Figure 2.8 – Generalized plane strain boundary condition used: uniform normal expansion of the plane is permitted but relative expansion about the axes of the plane are suppressed

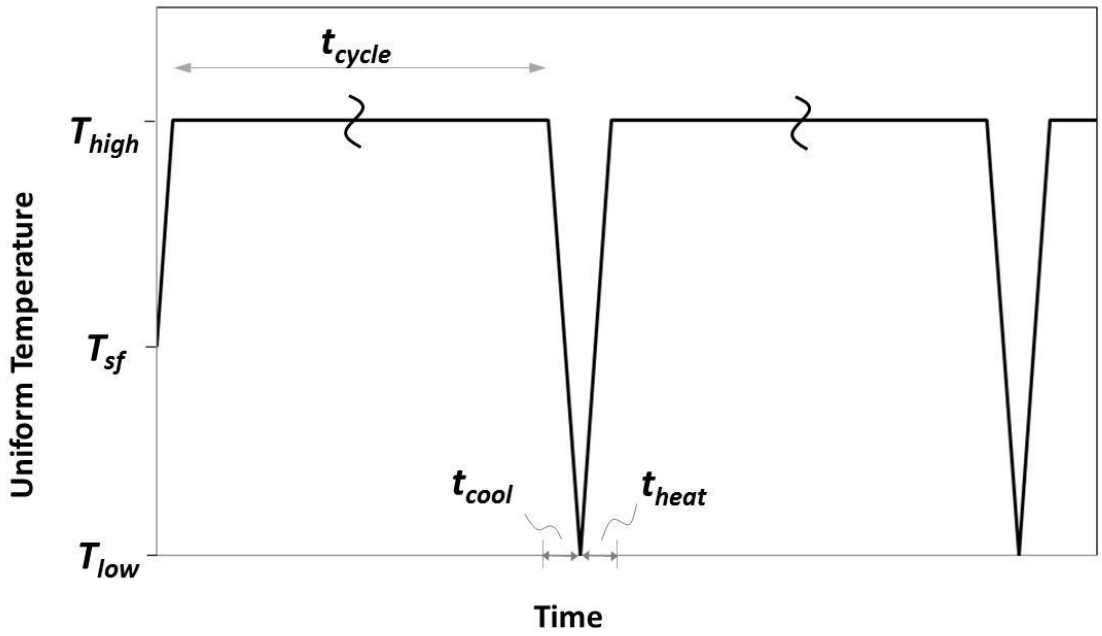

Figure 2.9 – Generic temperature cycle used in modeling

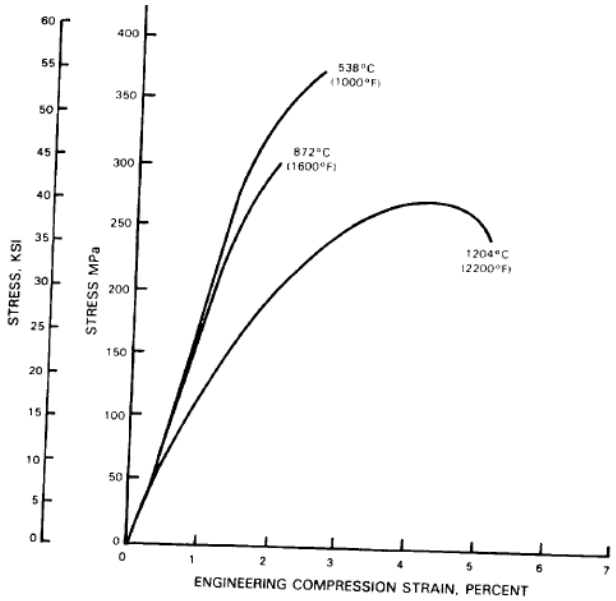

Figure 76 Representative Strain Tolerant Ceramic Compressive Stress-Strain Curves at Various Temperatures. Compressive strains calculated from corrected crosshead displacement.

Figure 2.10 – Compressive stress-strain curves at high temperatures; measured by DeMasi et. al. for YSZ [26]

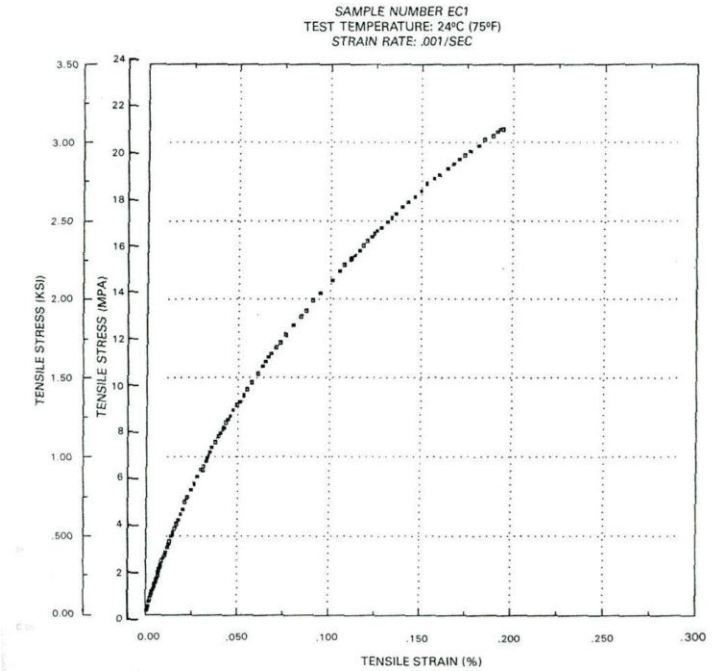

Figure 2.11 – Tension stress-strain curve is nonlinear even at room temperature; measured by DeMasi et. al. for YSZ [26]

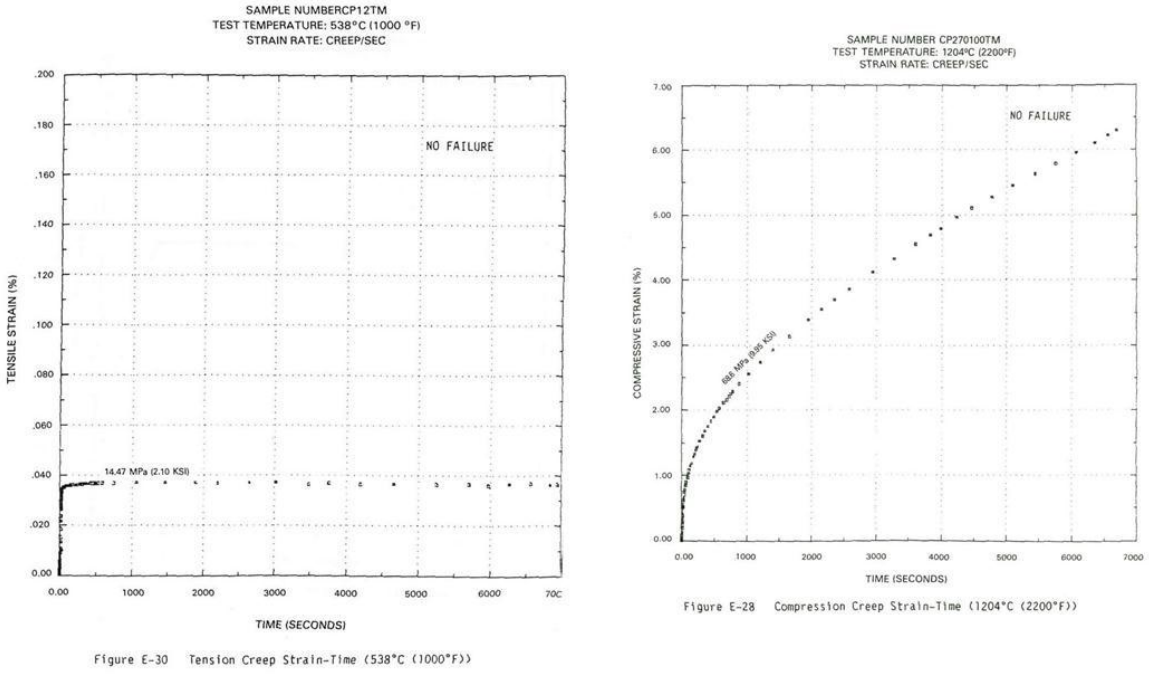

Figure 2.12 – Creep strongly dependent on temperature; tension creep at 1000°F (left); compression creep at 2200°F (right); measured by DeMasi et. al. [26]

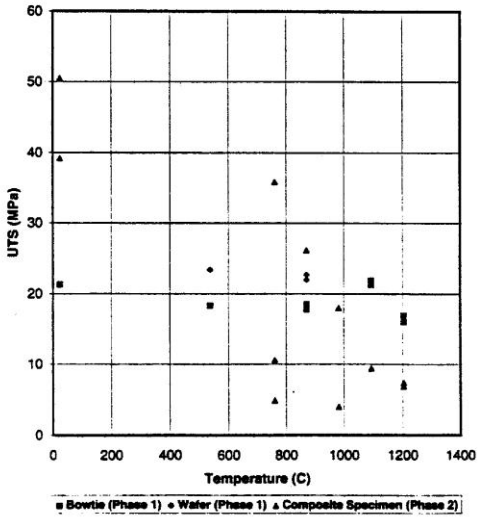

Fig. 8 Ultimate tensile strength vs. temperature for the bowtie, wafer, and composite specimens

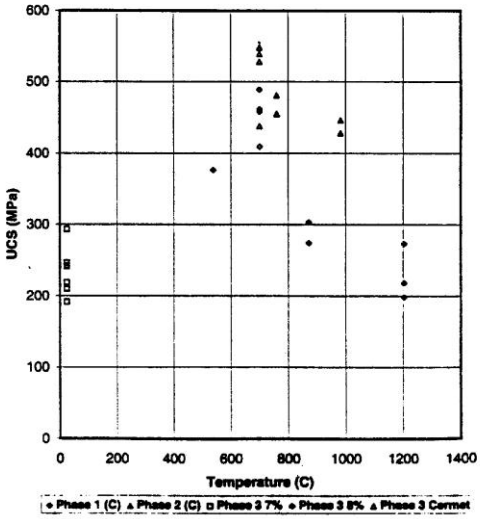

Fig. 9 Ultimate compression strength vs. temperature. C, compression; 7%, 7 wt% yttria PSZ; 8%, 8 wt% yttria PSZ

Figure 2.13 – Flow stress in tension (left) is about 10 times the flow stress in compression (right); measured by DeMasi et. al. [26]

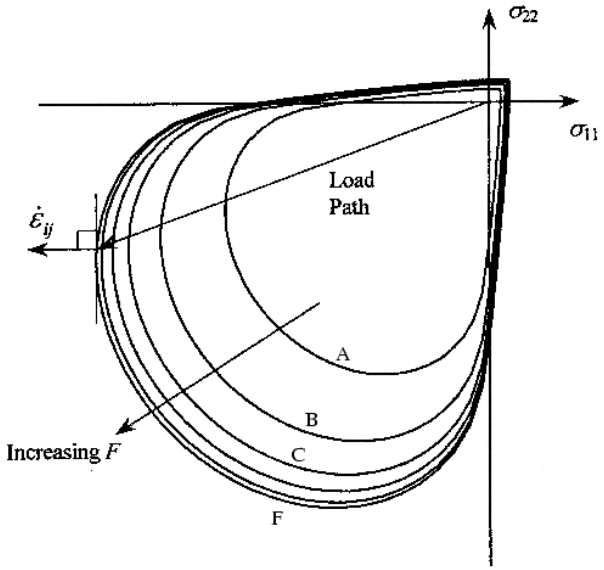

Figure 2.13 – Willam-Warnke flow surface plotted on the $\tau_{11} - \tau_{22}$ plane; A, B, C, etc. represent different σ_{33} [28]

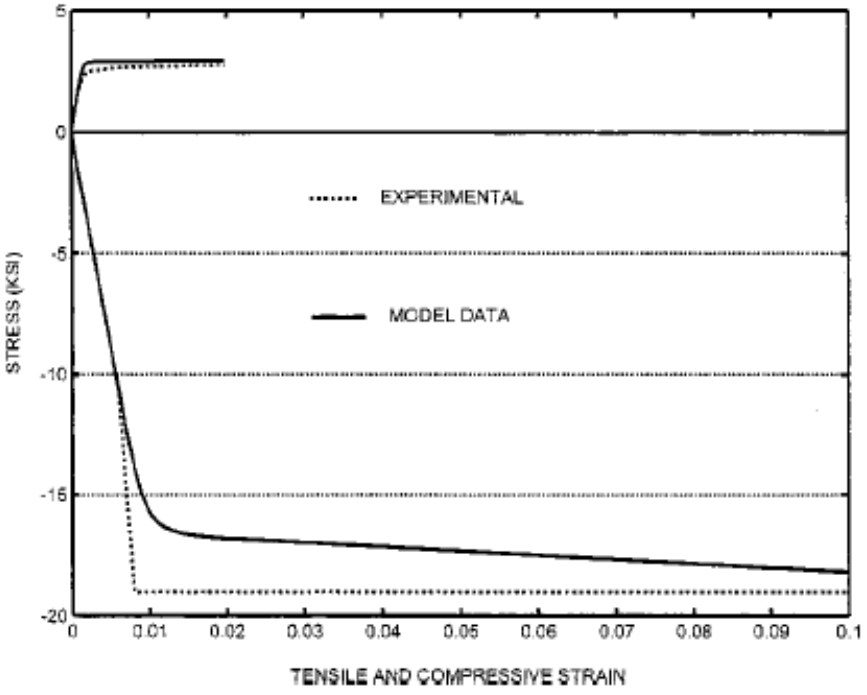

Figure 2.14 – Experimental vs. model for tensile and compressive response at 2200^{o}F [28]

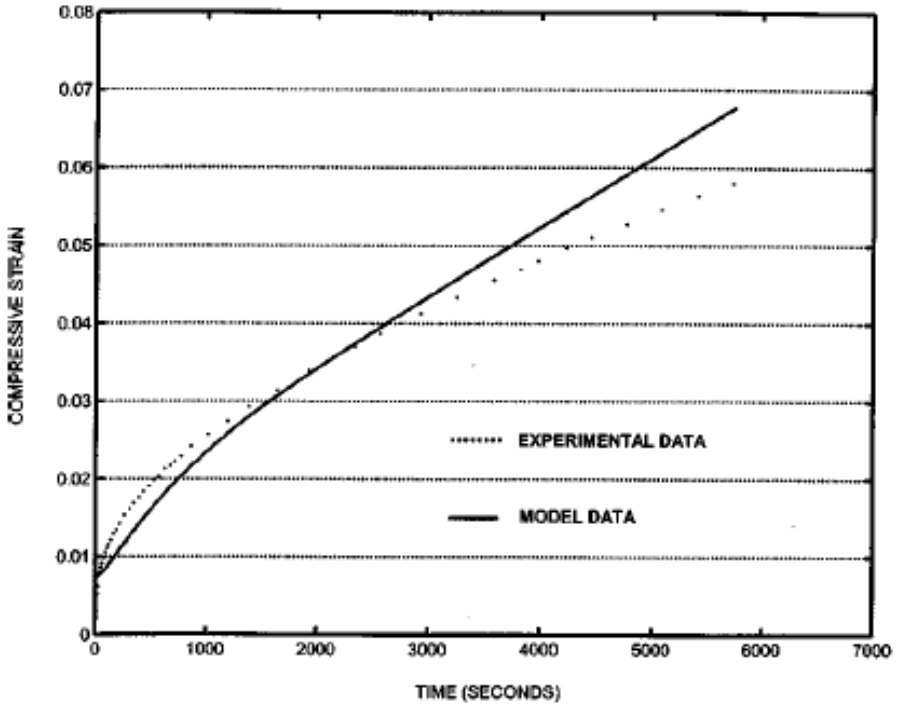

Figure 2.15 – Experimental vs. model for compressive creep at 2200^{o}F [28]

Table 2.1 – Generic material properties used for most models; linear elastic YSZ material properties used when viscoplastic constitutive model was not

	$\mathbf{E} \times \mathbf{10^{-6}}$ (psi)		ν	$\boldsymbol{\alpha} \times \mathbf{10^{6}}$ (1/°F)
Substrate	29		0.3	10
Bond Coat	29		0.3	8
TGO	50		0.25	4.5
Linear Elastic YSZ	2.50	75°F	0.22	6
	2.50	1000°F		
	2.30	1600°F		
	2.0	1800°F		
	1.80	2000°F		
	1.75	2200°F		

3. Results

The results presented here will be in two parts: results pertaining to physical observations made on the various coating samples and modeling results obtained from finite element analysis.

3.1 Part I: Experimental Results

3.1.1 TGO Thickness Results

Figure 3.1 shows the TGO thicknesses plotted against time for furnace cycling temperatures of 1900°F, 2000°F, and 2100°F. The data is also given in Table 3.1. The TGO growth of the samples was observed to be parabolic with time, as is commonly accepted, so the data was fit to an Arrhenius-type equation to facilitate the calculation of TGO thickness as a function of time and temperature. The equation was modified from the typical Arrhenius equation to account for linear interpolation of thickness between the initial thickness and the thickness at 50 hours, between which no data was collected. The initial growth rate of TGO is generally not parabolic, due to a different oxidation mechanism in the early stages of growth [39]. The equation used to calculate thickness is

$$h = \begin{cases} \frac{1}{50}(aT - b - h_o)t + h_o & t \leq 50 \\ \sqrt{k_{po}(t-50)e^{-Q/RT}} + h_{50} & t > 50 \end{cases}$$

where Q is the system specific activation energy for TGO growth, R is the gas constant, h_o is the initial TGO thickness, h_{50} is the thickness after 50 hours, and k_{po}, a, and b are constants. Figure 3.2 shows the TGO thickness measurements plotted against the square root of time, shifted by 50 hours. The slopes of these are the parabolic growth rates and the intercepts are the thicknesses at 50 hours. Figure 3.3 gives the thicknesses at 50 hours as a function of temperature, from which the constants a and b can be determined. The parabolic growth rate, k_p, is

$$k_p = \sqrt{k_{po} e^{-Q/RT}}$$

which can be rewritten as

$$-\ln\left(k_p{}^2\right) = \frac{Q}{R}\frac{1}{T} - \ln(k_{po})$$

If the natural log of the growth rates is plotted against inverse temperature, as in Figure 3.4, k_{po} and Q can be determined, since R is known. Q for this system was calculated to be approximately 206 kJ/mol. Table 3.2 gives a more complete summary of the values found for the present system. Figure 3.5 shows good agreement when the equation is plotted against the measured thicknesses.

3.1.2 Bond Coat Rumpling Results

Bond coat rumpling was measured using tortuosity, which was defined as the bond coat interface length over the straight line length. Measurements were made from micrographs of the interface using a pixel based measurement program. Due to the manner of data collection, the tortuosity measurements should be considered

rough. These quick and easy measurements did, however, yield important trend information about bond coat rumpling that we would not have had otherwise. More sophisticated image analysis can be applied to the micrographs to hone in on the precise measurements.

Measurements were made after every cycle (50 hour cycles) at every temperature from a series of about 10 micrographs extending over a distance of at least 2.5 mm. Figure 3.6 shows the tortuosity measurements plotted against TGO thickness, showing a roughly linear trend. This can imply that rumpling is driven by TGO growth, which has been previously suspected [17,10]. However, it should be noted that as the TGO thickens and internal oxidation increases, the delineation between TGO and bond coat becomes less and less apparent, making measurements more difficult, which is a possible alternative explanation for the apparent increase in tortuosity. As was the case when measuring the TGO thickness in the presence of non-α-oxide, it was ascertained that the best way to hedge against the uncertainty this ambiguity caused was to use good judgment when making the measurements.

3.1.3 Failure Mechanism Observations

3.1.3.1 Combustor Panels

Combustor lining panels that had failed in service were cut, mounted, polished, and examined using an environmental scanning electron microscope (ESEM). One sample, in particular, contained a region where the YSZ had spalled, surrounded by a region where the coating was intact. It was found that most of the damage occurred as

cracking of the YSZ top-coat above the YSZ/TGO interface. Figure 3.7 shows micrographs of the cross section of the sample in an area leading up to the spallation region, and Figure 3.8 shows the cross section in an area inside the spallation region.

From these cross section micrographs and others, it is clear that while there are areas of exposed TGO and bond coat, the majority of the spalled area remains coated with a thin layer of YSZ. Outside of the spalled area, any cracking is located just above the interface. To confirm the observation that failure propagated mainly through the YSZ above the interface, an x-ray diffraction pattern, in which the beam was long and thin and ran across the length of the sample, passing through the spallation zone, was compared to a pattern taken from an area with no spallation, and also to a catalogued pattern of Zr_2O_3, as shown in Figure 3.9. The patterns are close enough to confirm the observation, and do not reveal any new information about the structure of the system.

3.1.3.2 Oxidation Test Samples

Oxidation tests were performed for the purpose of identifying the TGO growth rate of the system, the results of which were presented in section 3.1.1. In addition to the oxidation measurements, the tests provided the opportunity to observe the failure mechanism in a uniform heating environment. One inch square samples were heated in 50 hour cycles as described in section 2.1.2. After every 50 hours, one sample was sectioned using a low-speed wet saw, mounted, polished, and examined under an ESEM to determine the TGO thickness and make failure mechanism observations.

Table 3.3 is a summary of the failure lives of the oxidation test samples. The lives are as follows. Three samples underwent cycles with a hold temperature of 2100˚F: two samples for the primary test (of which only one was actually cut into) and one as a confirmation test. The uncut sample failed upon cooling after the fourth cycle (200 hours) by large scale buckling (Figure 3.10), while the cut sample failed upon cooling after the fifth cycle (250 hours) by what appears to have been delamination initiated at the edge. The confirmation test sample was heated to 2100˚F in 50 hour cycles, following an initial cycle of 150 hours to accelerate the test. Failure of the confirmation test sample occurred upon cooling at 300 hours. Micrographs showing failure from selected cross sections of the 2100˚F samples are shown in Figures 3.11 and 3.12. Two samples underwent cycles with a hold temperature of 2000˚F. This time one of the samples was consumed due to cutting, while the second sample incurred only minimal cutting. The remaining sample failed upon cooling after 600 hours, again by large scale buckling (Figure 3.13). Micrographs of the cross sections of the 2000F samples are shown in Figures 3.13 and 3.14. Three samples were used for cycling at 1900˚F. Two of the samples had been consumed due to cutting when the testing was suspended after 2400 hours (more than enough TGO thickness data having already been collected). Figure 3.15 shows a cross section from one of the 1900F samples. Comparing this figure to one of the previous ones, it becomes clear that the amount of damage incurred is highly sensitive to temperature. The progressiveness of the damage will be commented on in the discussion section.

The micrographs show that most of the damage occurs in the YSZ above the TGO/YSZ interface, either close to the interface or sometimes as much as 25-50 microns above it. Occasionally a crack dips below the interface and runs through the TGO. In an attempt to confirm that the main failure plane was in the YSZ, image analysis was performed on the failure surfaces to determine the relative amounts of YSZ and TGO/bond coat on each surface. High resolution photos of the surfaces were imported into an image processing program, the images were reduced to two colors using a threshold, and the proportion of each color was obtained. Figures 3.16 and 3.17 show the failure surfaces of the 2100F and 2000F samples, respectively, and the percentages of YSZ and TGO/bond coat on each. Note that there is more YSZ on the topcoat side than the substrate side in both cases. This discrepancy can be attributed to areas where the failure crack passes directly between the YSZ and oxide, which is common, as shown in Figure 3.18.

Another finding that is worth reporting is the presence of non-α-Al_2O_3 in all the samples, but especially the disproportionate amount in the 2100F samples, which developed large regions of non-α-Al_2O_3, possibly Cr_2O_3 or a NiCr spinel, in the proximity of the YSZ/TGO interface and can be seen in Figure 3.18. These areas were not present in the as-sprayed samples, but were well established after 50 hours at 2100F. The areas of non-α-Al_2O_3 were not continuous along the interface, but were only present at intervals, where the thickness ranged from 2 to 4 times the thickness of the α-Al_2O_3. Observations of these regions under an optical microscope revealed them to be blue, indicative of a chromium rich composition. An EDX analysis of this non-α-Al_2O_3, Figure

3.19, shows the oxide to be rich with chromium. The non-α-Al_2O_3 regions were found to contain distinct horizontal cracks parallel to the interface, characteristically different than the cracking found in the YSZ (Figure 3.20). These cracks were found in some of the non-α-Al_2O_3 after 50 hours and in the majority after 100 hours. Figure 3.21 shows the main failure crack of a 2100F sample running through a large tract of non-α-Al_2O_3. The strict horizontal cracks seem to indicate that the non-α-Al_2O_3 acts as a low toughness pathway for crack extension, possibly accelerating coating failure.

3.1.3.2.1 Crack Opening Displacements

The crack openings seen in some of the micrographs of the progressively damaged oxidation test samples offered a chance to estimate the residual stress present in the coating. Figure A shows the two particular cracks that were used in the calculations. The crack opening displacement at the center of the crack was compared to the exact solution for a "penny-crack" in an infinite domain subject to far field out-of-plane stress. The far field stress (or, equivalently, the uniform pressure load on the crack faces) required to create an opening, δ_o, in a linear elastic material is:

$$\sigma = \frac{\delta_o \pi E}{8a(1-\nu^2)}$$

where *a* is the crack radius [38]. The crack opening displacements in Figures 3.22(a) and 3.22(b) were 22 μm and 12.5 μm at their centers. The far field stresses required to for these displacements were found to be 539 MPa and 439 MPa, respectively. The implications of these comparisons will be elaborated on in the discussion.

3.1.3.3 Burner Rig Sample

Observations were also made on a sample which had failed during burner rig testing, allowing observations to be made on a sample which had failed in a thermal gradient environment. Figure 3.23 shows the as received sample has an area of heavy damage as well as an area which appears similar to the failure surfaces of the oxidation test samples. It is assumed that the heavy damage to the coating was incurred as a result of continual heating after the coating had already failed. This is supported by Figure 3.24, which shows oxide growth directly on the substrate, which means that the sample must have experienced high temperatures after the top coat, and even bond coat, had spalled away. The sample was examined using a field emission scanning electron microscope (FESEM). The micrograph in Figure 3.25 was taken near the edge of the failed region, showing the failure crack to pass just above the interface like the oxidation sample and combustor panel failure cracks. To be sure that the white areas of the spalled surface were predominately YSZ, an EDX element map was obtained and is shown in Figure 3.26.

3.2 Part II: Finite Element Modeling Results

Table 3.4 gives a synopsis of the different cases that were modeled. First, a baseline case was run which depended only on thermal expansion mismatch. Next, several cases were run which attempted to model the morphological phenomena observed in part 3.1. Of these, the case which had the largest effect on the trend of the

stress state and which was considered most realistic was selected for a more detailed stress analysis.

Unless otherwise noted, stresses are output at four locations: just above the peak (location P), just above the valley (location V), 25 microns above the peak, over the peak (location AP), and 25 microns above the peak, over the valley (location AV), as depicted in Figure 3.27. These locations were chosen because they represent the bounds in which the final failure crack usually passes, and it was thought that the stresses in between could be inferred from stresses at these locations. Most of the stress presented is the out-of-plane stress (out of the plane of the coating) ($S_{22,}$ or the normal stress in the vertical direction). This is thought to be the most relevant stress to failure because it acts perpendicular to the failure plane and is therefore largely responsible for any mode 1 cracking.

3.2.1 Thermal Mismatch Only Reference Case

To obtain a baseline for comparison when more complicated effects are taken into consideration, stresses resulting from thermal mismatch only were obtained at the four locations for TGO thicknesses of 1, 2, 3, 4, 5, 6, and 8 microns. All layers were considered to be elastic. A net temperature drop of 975^{o}F was considered, with the stress-free temperature chosen to be 1000^{o}F and room temperature set at 75^{o}F. The out-of-plane stresses as a function of TGO thickness at the four locations are shown in Figure 3.28. The stresses are initially tensile above the peak and compressive over the valley. When the TGO reaches a thickness of about 5 to 6 microns, the stress at

locations P and V switches its sign. The change in sign at locations AP and AV takes longer, implying that the rate of stress transition decreases as the distance from the interface increases. These findings aren't too surprising, and they are in agreement with analytical results from concentric cylinder models [11] and also with previously published finite element modeling [14]. Probably the most valuable results from this model are the general magnitudes of the stresses, which are in the 10's of MPa range and give an indication of realistic stress magnitudes for these systems.

3.2.2 Morphological Phenomena Models

Models considering TGO growth, bond coat rumpling, bond coat shrinkage, TGO plasticity, and combinations thereof were analyzed to understand their implications on the stress state in the YSZ. The YSZ was first considered to be elastic, then later viscoplastic. The hold temperature was 2000^{o}F for all cases.

3.2.2.1 YSZ Modeled as Elastic

3.2.2.1.1 TGO Growth

The TGO layer was grown continuously by the method described in section 2.5.3, according to the growth rate measured and presented in section 3.1.1. Out-of-plane stresses were output at the four locations as before. Figure 3.29 shows S_{22} plotted against time. Most of the time, the system is at high temperature, with the spikes being the return to room temperature. Figure 3.30 shows the stresses for the elastic case plotted against TGO thickness. The stress is clearly increasing proportionally to TGO

thickness. Notice the magnitudes of the stresses rise to be over two orders of magnitude greater than the thermal mismatch only case.

3.2.2.1.2 Bond Coat Rumpling

Rumpling was modeled by the procedure described in section 2.5.4. A simplified implementation of rumpling was adopted, where the change in tortuosity measured after 200 hours of thermal cycling was converted to a change in amplitude, holding the wavelength constant. The amplitude was changed from 25 microns to 35 microns in 200 hours, proportionally to TGO thickness (but for this case the TGO was not grown, only tracked). The shape change can be seen in Figure 3.31, which compares the two amplitudes drawn in Excel with the beginning and ending bond coat profiles from Abaqus. Figure 3.32 shows S_{22} plotted against time, and Figure 3.33 shows it plotted against TGO thickness. As in the previous case, the stresses are in the GPa range. Their magnitudes, however, are higher because the amplitude change in this case is greater than the effective amplitude change due to TGO growth.

3.2.2.1.3 TGO Growth & Bond Coat Rumpling

In this case, TGO growth and rumpling were considered together. Figure 3.34 shows S_{22} plotted against time, and Figure 3.35 shows it plotted against TGO thickness. The stresses shown in Figure 3.35 are the sum of the stresses generated by TGO growth only and rumpling only (Figures 3.30 and 3.33), as they should be, since the YSZ is linear elastic.

3.2.2.1.4 TGO Growth & Bond Coat Al Depletion

Bond coat aluminum depletion was modeled by the procedure described in section 2.5.5. TGO growth is included in this model since it is assumed that any aluminum depleted from the bond coat will be used to grow the TGO, so it makes sense that these two effects should always be coupled. As noted earlier, when the effects of bond coat shrinkage are taken into consideration, the present case, in which the entire volume under the asperity is considered to be composed of β-NiAl and all the aluminum to create TGO comes from here, can be considered the most severe. On the other hand, the case in which no bond coat shrinkage takes place (i.e. the results presented in 3.2.2.1.1), can be considered as least severe, representing the case when the aluminum to create TGO diffuses up from the interior of the bond coat, rather than under the asperity. Figure 3.36 shows S_{22} plotted against time, while Figure 3.37 plots it against TGO thickness. Figure 3.38 shows a comparison of Figure 3.37 (TGO growth & bond coat shrinkage) and Figure 3.30 (TGO growth only). It shows the depletion to lower the stress and implies that since these are the two bounding cases, the stresses resulting from the actual effects of bond coat aluminum depletion should lie in the shaded regions.

3.2.2.1.5 TGO Growth & TGO Plasticity

The effects of material nonlinearities in layers other than the topcoat were considered in this case. The TGO was considered because it incurs very large elastic stresses that have the highest potential of affecting the stress state in the topcoat when

they are redistributed. Particularly, the effect that a perfectly plastic TGO at high temperature would have on the YSZ was of interest. The yield strength of the TGO was considered temperature dependent. The low temperature yield strength was taken to be 10 GPa, after Evans et. al. [16], so that the TGO behaves elastically at low temperature. The yield stress at high temperature was chosen by trial and error so that the resulting maximum stress magnitude in the TGO upon cool down was in the range of 4 to 5 GPa, which is realistic when compared to direct measurements of stress in the TGO by PLPS (although this is for EBPVD coatings). Since resulting values by trial and error were close to the value of 1 GPa used by Evans et. al., for consistency, this was the value that was chosen. Figure 3.39 shows the temperature dependence of the yield strength.

Figure 3.40 shows S_{22} at the four locations plotted against time and Figure 3.41 shows them plotted against TGO thickness. Note that now both locations just above the interface are in tension and the locations 25 microns into the topcoat have swapped signs. Also, the stress dependence on TGO thickness is no longer linear.

3.2.2.1.6 TGO Growth, Bond Coat Al Depletion, & TGO Plasticity

TGO growth, bond coat shrinkage, and TGO plasticity were considered as a compliment to the previous case in order to obtain a lower bound for the stresses when aluminum depletion is accounted for. Figure 3.42 shows S_{22} at the four locations plotted against time and Figure 3.43 shows them plotted against TGO thickness. Figure 3.44 shows the stresses plotted against TGO thickness for TGO growth and TGO plasticity for

the cases with and without bond coat shrinkage (only locations P and V are plotted, for clarity). Note that the tensile stress above the peak increases while the tensile stress above the valley decreases when bond coat shrinkage is added.

3.2.2.2 YSZ Modeled as Viscoplastic

The stresses generated in the YSZ in the previous cases, with the exception of the baseline case where the stresses were due to thermal mismatch only, were all well into the GPa range. Since the YSZ obviously cannot accommodate these stresses without failing immediately, one of two possibilities exists. Either the stresses due to TGO growth are limited by material nonlinearities in the TGO and bond coat, or they are redistributed by the viscoplastic properties of the YSZ. Probably it is a combination of the two, but one of the effects must be more prevalent than the other. Figures 3.40 and 3.41 already give preliminary evidence that once the stresses in the YSZ, in the presence of TGO plasticity, redistribute, they continue to grow with TGO thickness into the GPa range. Therefore, for comparison purposes, the procedure to incorporate viscoplasticity into the YSZ, as described in section 2.5.6, was implemented in order to uncover the stress state that results when growth stresses are applied to a viscoplastic topcoat. The following cases are roughly analogous to the cases above with the exception of bond coat shrinkage, which was not considered.

3.2.2.2.1 TGO Growth

This case considers TGO growth only. Figure 3.45 shows S_{22} plotted against time. As before, the system is at high temperature most of the time, with the spikes being the return to room temperature. Note the disturbance in the stresses at 50 hours. This is due to the TGO growth rate being discontinuous here, a consequence of the switch from a linear to a parabolic growth rate in the model used to grow the TGO. Since the viscoplastic model is strain rate dependent, a sudden drop in growth rate leads to a sudden drop in stress. The stresses are plotted against TGO thickness in Figure 3.46. The stresses just above the peak dip into compression, but emerge into tension after about 100 hours, while the stresses just above the valley stay in compression nearly the entire time. An explanation for this stress state will be offered in the discussion section. Figure 3.47 shows contour plots at various times throughout the history. Only tension is shown, any compression is colored black. Notice that the out-of-plane tensile regions eventually traverse the entire width of the model, providing an opportunity for crack extension.

3.2.2.2.2 Bond Coat Rumpling: With and Without TGO Growth

Two cases were actually run here: bond coat rumpling with and without TGO growth. For the case without TGO growth, Figure 3.48 shows S_{22} plotted against time. The stresses just above the peak initially dip into compression, but unlike the previous case, they remain there. It is important when comparing the rumpling case to the TGO growth only case to remember that in the rumpling case, the material under the

asperity only grows vertically, while TGO growth causes the shape change of the asperity to have a vertical and horizontal component. This will be elaborated on in the discussion. Again, the reduction in the stresses at 50 hours is the result of the artificial discontinuity in growth rate. Figure 3.49 shows S_{22} plotted against time for the case with TGO growth. There is not much of a difference in the stress trends when TGO growth is added except for a slight increase in the magnitude of the stresses.

3.2.2.2.3 TGO Growth & TGO Plasticity

In this case, TGO plasticity was considered while only the TGO was grown. Figure 3.50 shows S_{22} at the four locations plotted against time and Figure 3.51 shows them plotted against TGO thickness. At the outset, the stresses quickly establish themselves at the "steady state" values, or their "elastic limits". Except for the initial stages of TGO growth, the stresses obtained for TGO growth cases with and without plasticity are very similar. Figure 3.52 shows contour plots at various times throughout the history. Notice in this case, unlike the case with no TGO plasticity, that the out-of-plane tensile region remains, for the most part, over the peak and does not traverse the entire width of the model, providing for a more difficult crack pathway.

3.2.3 Temperature & Cycle Dependence Results

Of the various cases run to determine the relative effects on the topcoat stress state, the case in which only TGO growth occurs was chosen as the representative case for development of a more detailed stress analysis. In this extended stress analysis, it

was desired to obtain information about the effects of cycle duration and temperature on the stress and strain history, to correlate this information with experimental observations that life increases with cycle duration and decreases with temperature, and thus provide direction for a possible life prediction method.

3.2.3.1 Stress Dependence on Temperature

Figure 3.53 shows S_{22} at location P taken out to 200 hours in 50 hour cycles. The hold temperatures were varied between 1950^{o}F and 2100^{o}F, with the rest of the cycle parameters remaining the same. The results show that for higher temperatures, the material above the peak goes into tension faster. Figure 3.54 shows the time it takes location P to go into tension for each temperature, annotated with the TGO thickness at that time. This implies that the TGO thickness is the driver of stress in this case. Figure 3.55 is a plot of S_{22} against TGO thickness for each temperature. The critical thickness when the YSZ above the peak switches sign is about 3 microns.

3.2.3.2 Stress Dependence on Cycle Duration

Figure 3.56 and Figure 3.57 show the evolution of S_{22} at locations P and V and locations AP and AV, respectively, for cycle durations of 2 hours and 200 hours (both 2000F). Clearly, the stresses are affected by the duration of the cycle, apparently more so as the distance from the interface increases. To see this effect more clearly, in Figure 3.58 is plotted S_{22} at location AP after 200 hours of hot time at 2000F for different cycle durations. To see the varying effect cycle duration has on stress as the distance above

the interface increases, stresses after 200 hours at 2000F were plotted along a path extending vertically above the peak (Figures 3.59). Figure 3.58 is a representation of Figure 3.59 when the distance above the peak is fixed at 25 microns. So for longer cycle durations, the effect of reducing the cycle duration on stress is small, especially close to the interface, but for shorter cycle durations (below about 50 hours in this case) the effect becomes noticeable, especially as the distance from the interface increases.

3.2.3.2 Inelastic Strain Dependence on Temperature

The limit stress of the viscoplastic constitutive law used to model the YSZ was taken to be the fracture stress, measured experimentally, so that any stresses obtained in finite element results would not be greater than the failure strength of the coating [28]. The physical interpretation of this would be localized failure in the regions where the calculated strains cause stresses to exceed the limit stress. Due to the brittleness of the YSZ at low temperature, this failure can be considered microcracking. At high temperatures, however, its viscoplastic characteristics permit material flow, possibly with some microcracking. This is why inelastic strain accumulation at both high and low temperatures was monitored in the following simulations. The areas of highest accumulation are the locations in the coating most susceptible to microcracking, and consequently most likely to eventually link up with the main failure crack.

In addition to total time at temperature, the accumulation of inelastic strain depends on both temperature and cycle duration. Figures 3.60 – 3.62 are plots of low temperature ("cold") inelastic strain contours for temperatures of 1950F, 2000F, and

2050F, with the cycle duration held constant at 50 hours, and Figures 3.63 – 3.65 show the complimentary high temperature "hot" inelastic strain accumulation.

From the contour plots, it is seen that the inelastic strain over the peak accumulates more slowly than the other locations. It is also the location that the tensile stress shifts to. Therefore, the rate of accumulation just above the peak is of special interest. In Figures 3.66, 3.67, 3.68, and 3.69, the combined inelastic strain accumulation just above the peak is plotted against hot time (total time adjusted for ramp time) for cycle durations of 2, 8, 50, and 200 hours, respectively.

3.2.3.3 Inelastic Strain Dependence on Cycle Duration

To illustrate the effect of cycle duration on inelastic strain accumulation, contour plots are shown for cycle durations of 2, 50, and 200 hours, with the hold temperature set at 2000^{o}F. Figures 3.70 – 3.72 show the low temperature inelastic strain contours while Figures 3.73 – 3.75 show the high temperature inelastic strain contours. Like before, in Figures 3.76, 3.77, and 3.78 are plotted the combined inelastic strain accumulation just above the peak, this time for temperatures of 1950^{o}F, 2000^{o}F, and 2050^{o}F, respectively.

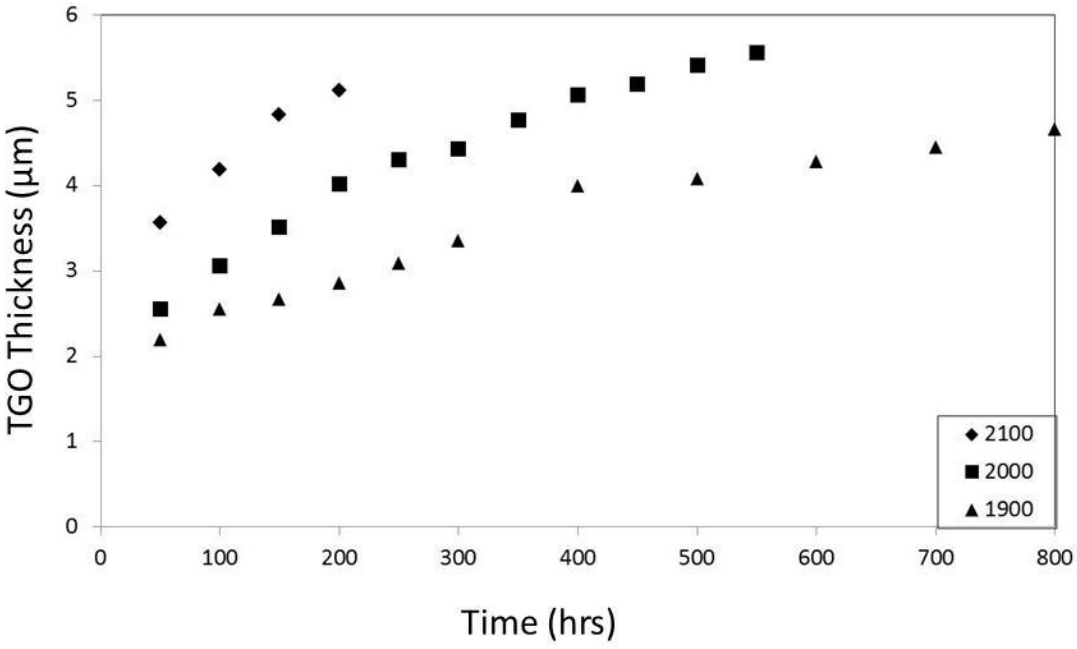

Figure 3.1 – Measured TGO thicknesses at 1900°F, 2000°F, and 2100°F

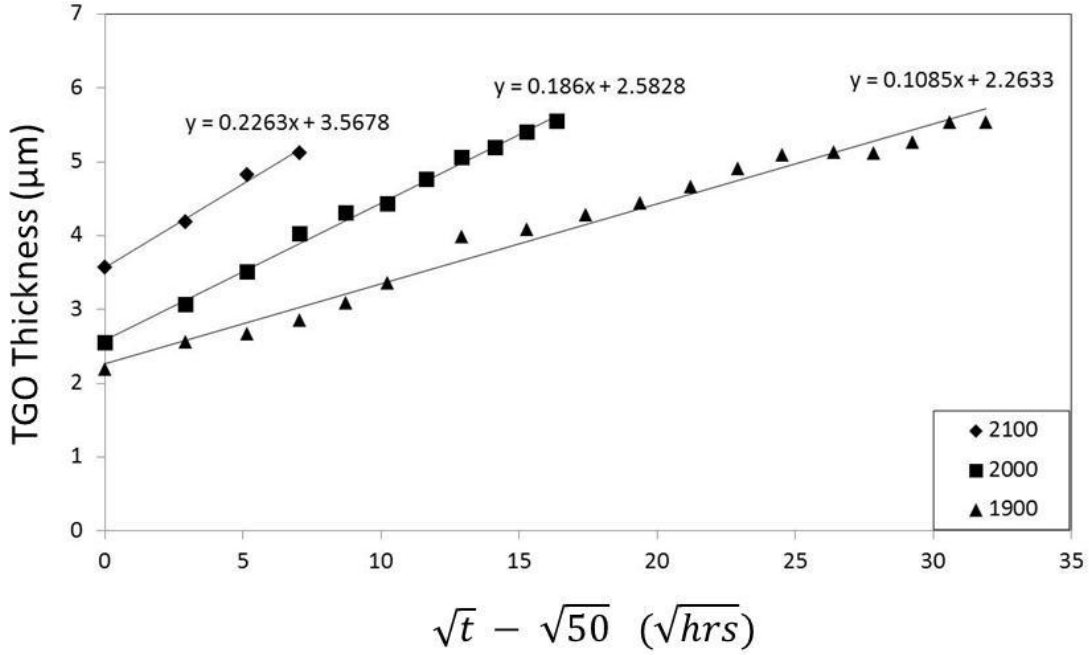

Figure 3.2 – TGO thickness vs. square root of hot time, shifted by 50 hours

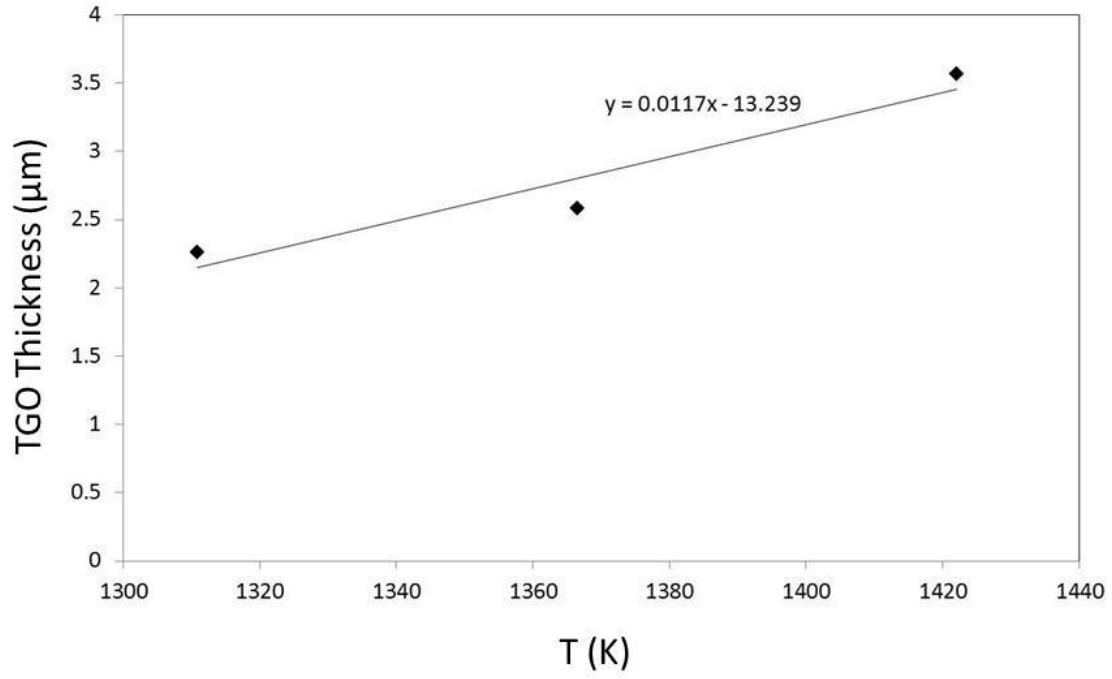

Figure 3.3 – TGO thickness after 50 hours for 1900°F, 2000°F, and 2100°F for extraction of a & b

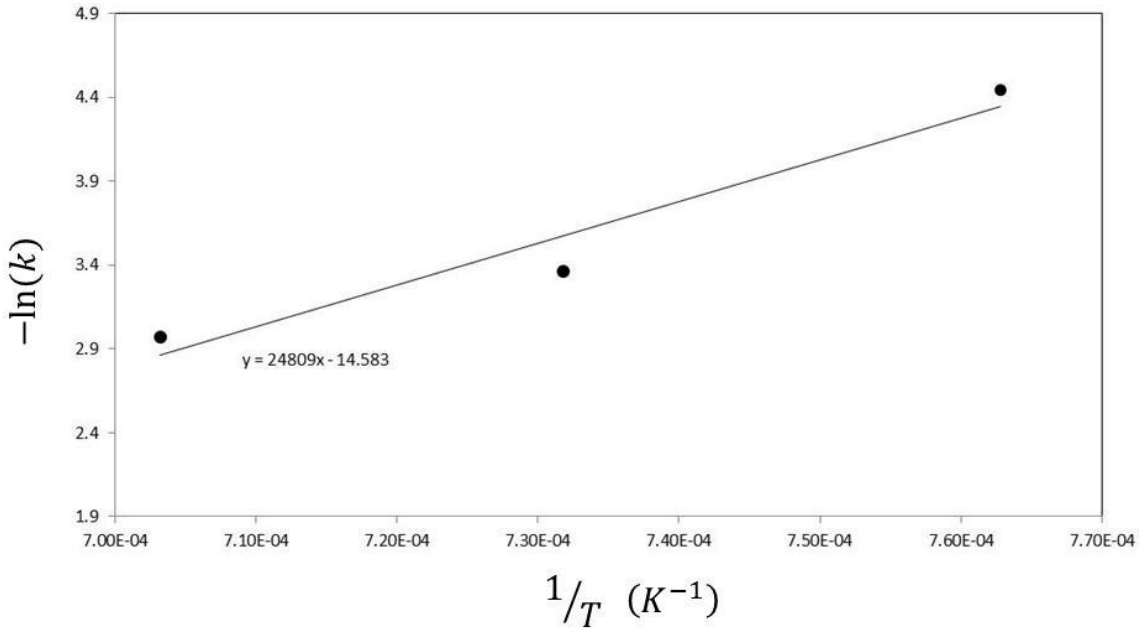

Figure 3.4 – Natural log of growth rates vs. inverse temperature for extraction of k_{po} and Q

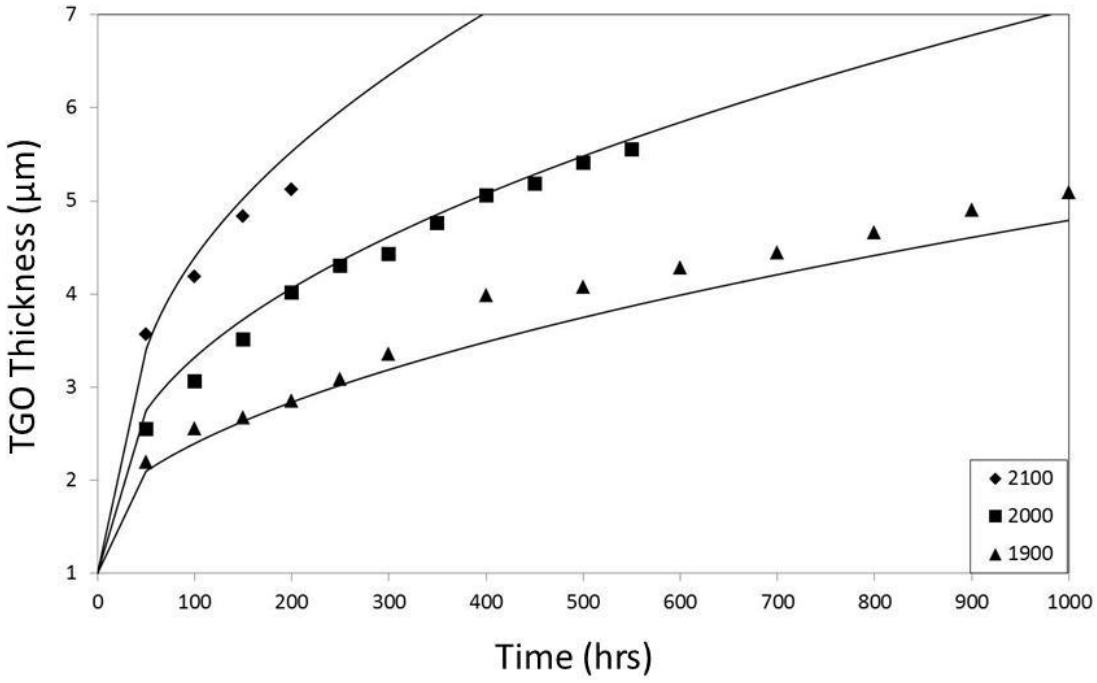

Figure 3.5 – Experimental values vs. model predictions show good agreement

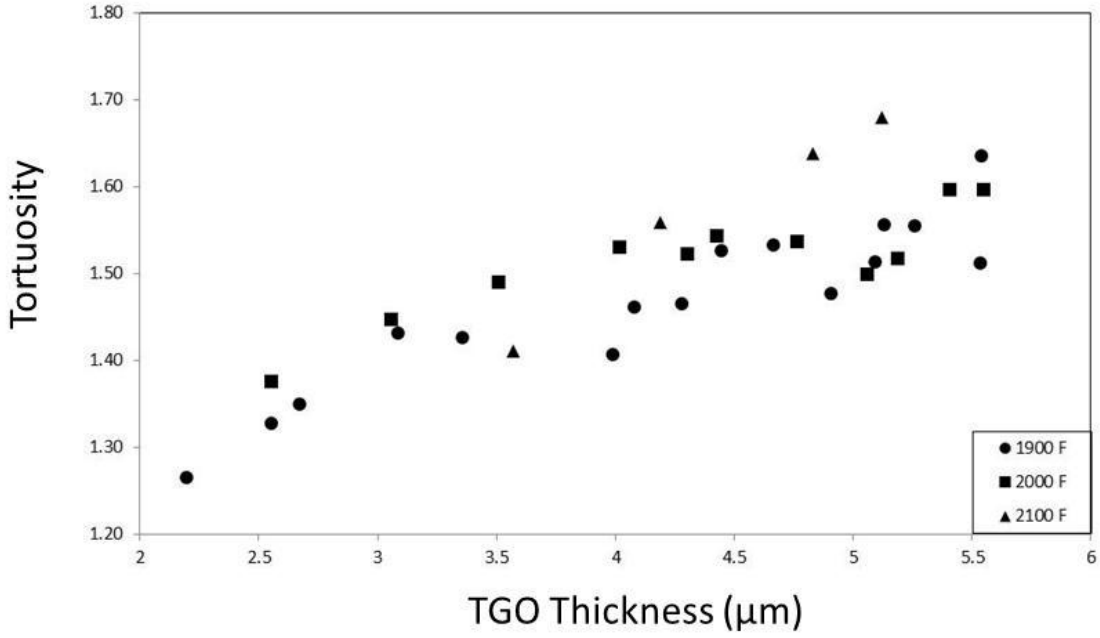

Figure 3.6 – Tortuosity at 1900°F, 2000°F, and 2100°F as a function of TGO thickness, showing a rough linear trend

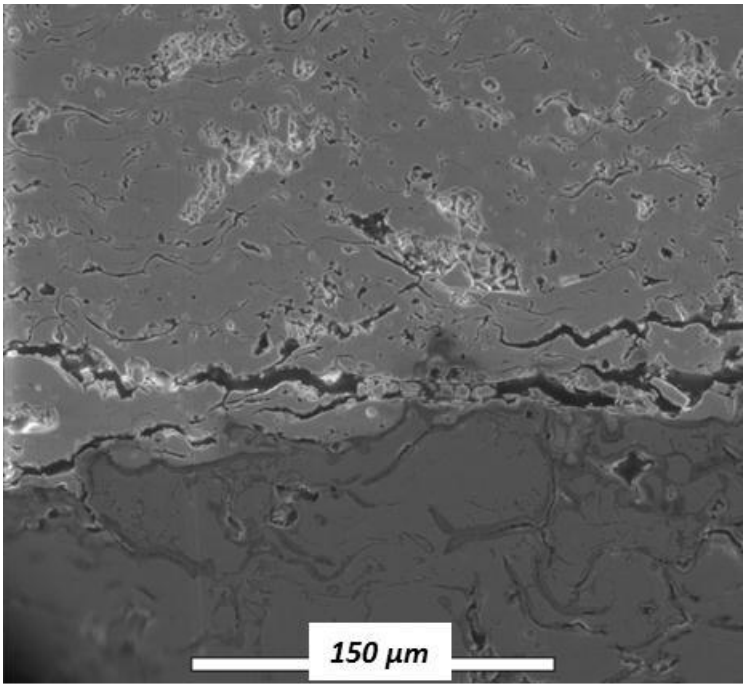

Figure 3.7 – Micrograph of combustor panel in an area approaching the spallation zone showing cracking above the interface

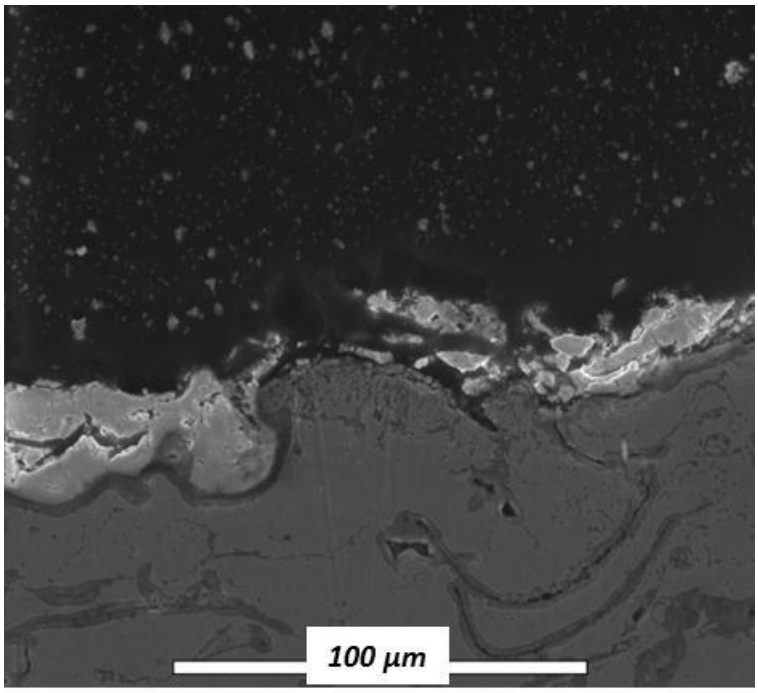

Figure 3.8 – Micrograph of combustor panel in an area inside the spallation zone showing a thin layer of YSZ remaining

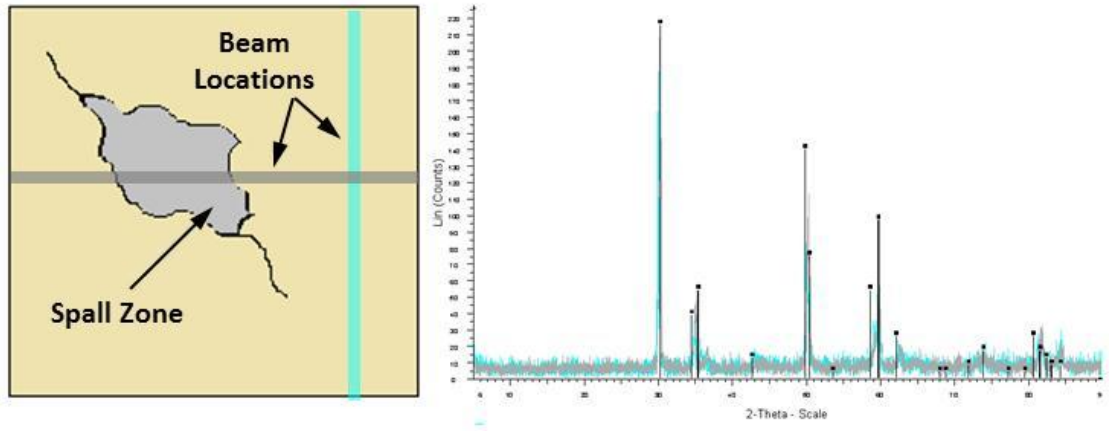

Figure 3.9 – Drawing of spalled combustor panel and beam locations(left); superimposed XRD patterns from 2 beam locations and a catalogued YSZ pattern show that spalled zone contains mainly YSZ (right)

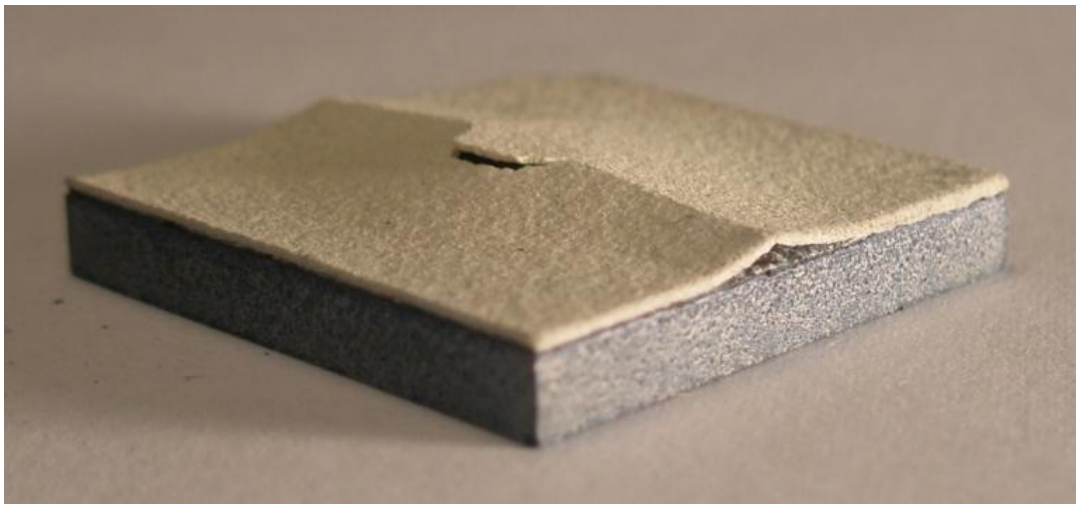

Figure 3.10 – Oxidation test sample: buckled upon cool down after 200 hours at 2100°F (50 hr/cycle)

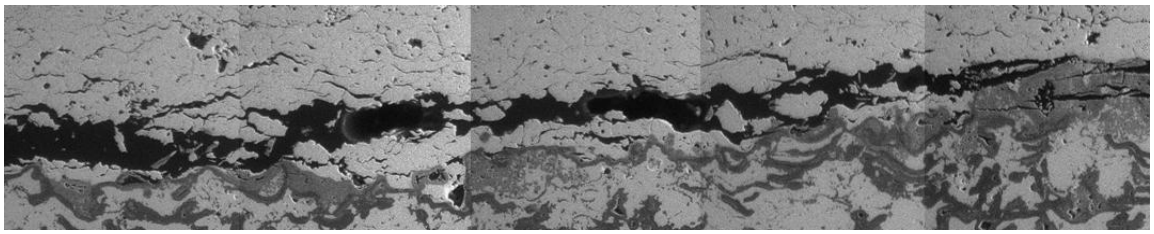

Figure 3.11 – Major failure crack after 250 hours at 2100°F (50 hr/cycle) (note also the heavy non-α-Al_2O_3)

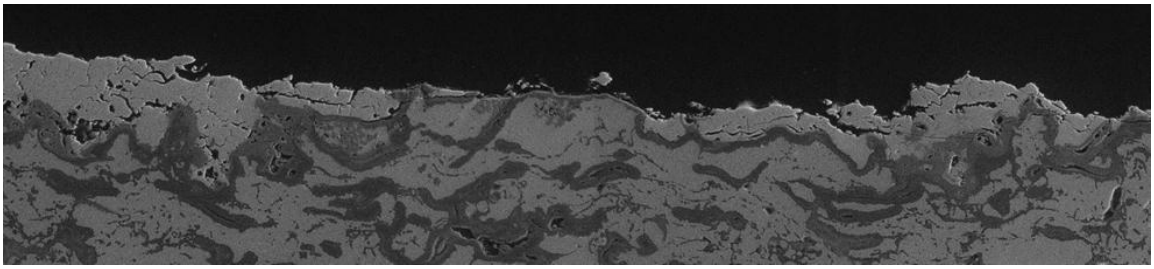

Figure 3.11 – Spalled coating after 300 hours at 2100^{o}F (50 hr/cycle)

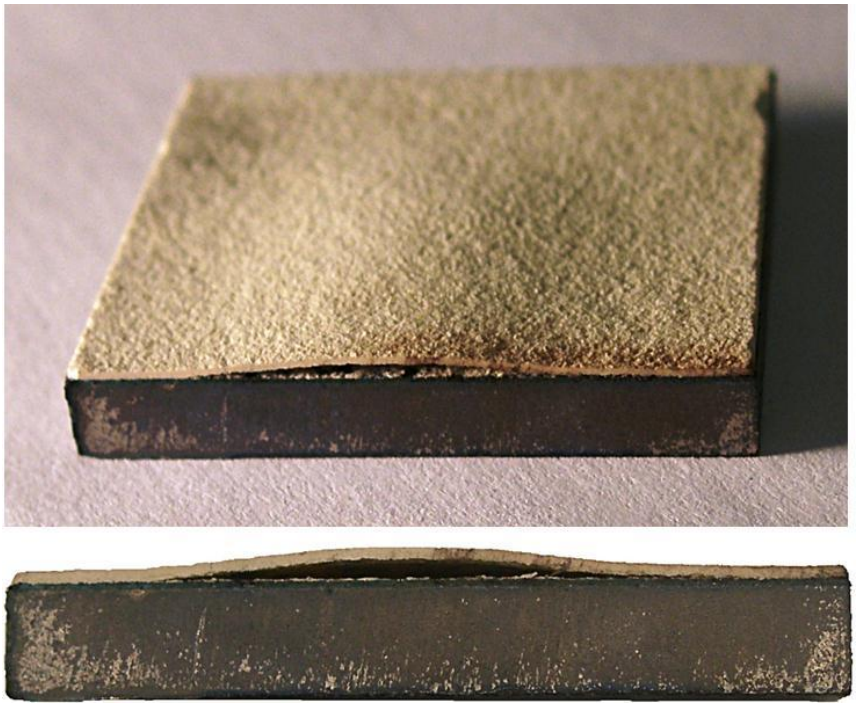

Figure 3.12 - Oxidation test sample: buckled upon cool down after 600 hours at 2000^{o}F (50 hr/cycle) (note the attached layer of YSZ)

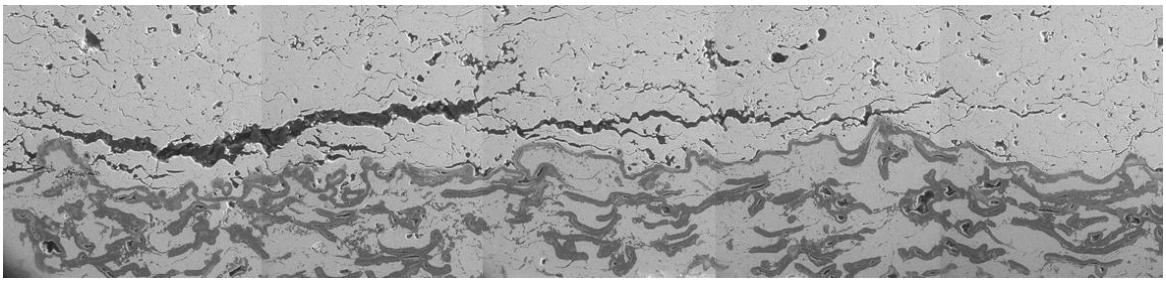

Figure 3.13 – cracks with large openings seen after 450 hours at 2000^{o}F (uncut sample failed after 600 hours)

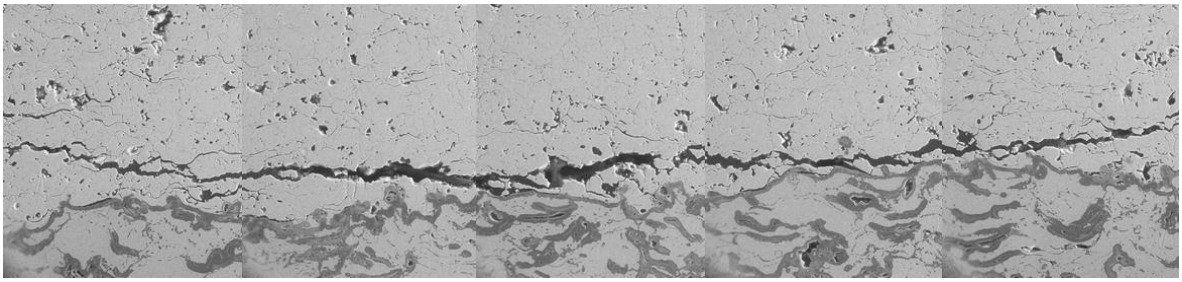

Figure 3.14 – Major crack running above interface of oxidation test sample after 500 hours at 2000^{o}F (50 hr/cycle)

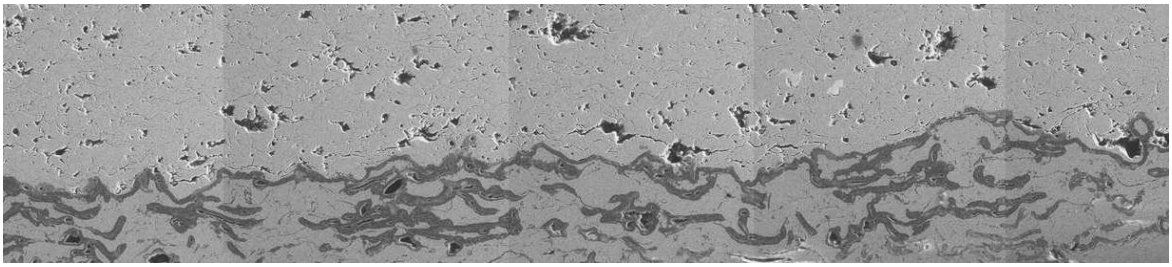

Figure 3.15 – Minimal cracking is seen even after 1520 hours at 1900^{o}F

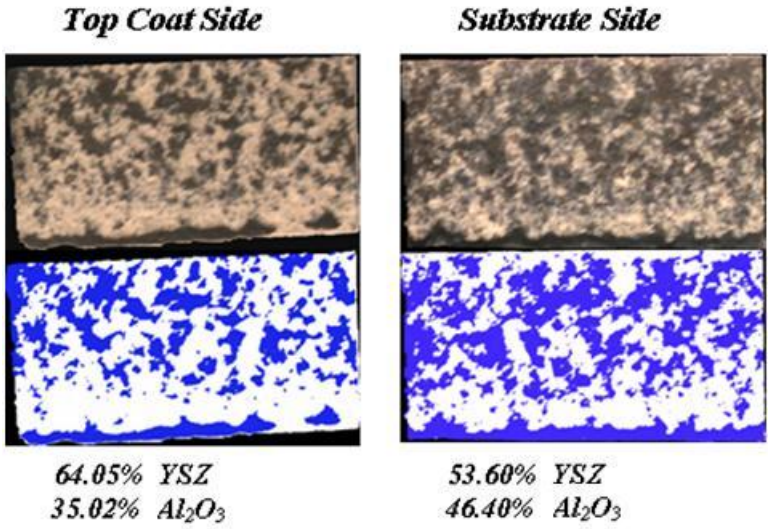

3.16 - Failure surface analysis from a sample failed after 250 hours at 2100^{o}F

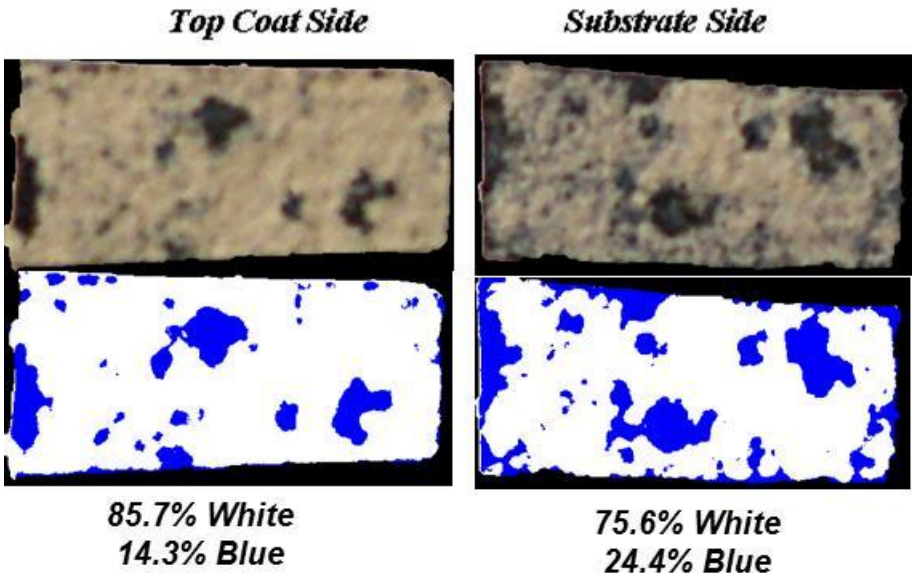

Figure 3.17 – Failure surface analysis from a sample failed after 600 hours at 2000^{o}F

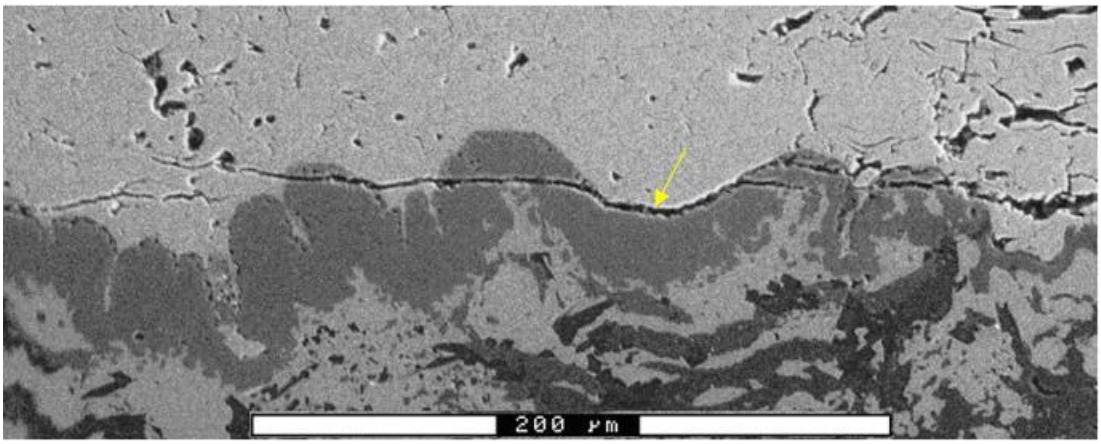

Figure 3.18 – Cracking at YSZ/non-α-Al_2O_3 interface (oxidation test sample after 100 hours at 2100˚F)

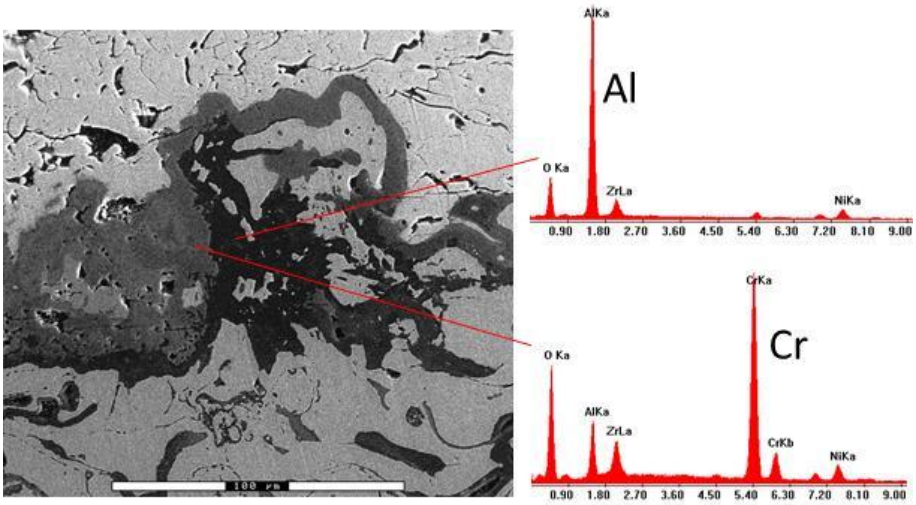

Figure 3.19 – An EDX analysis of the two oxides shows Al_2O_3 and an oxide rich in chromium

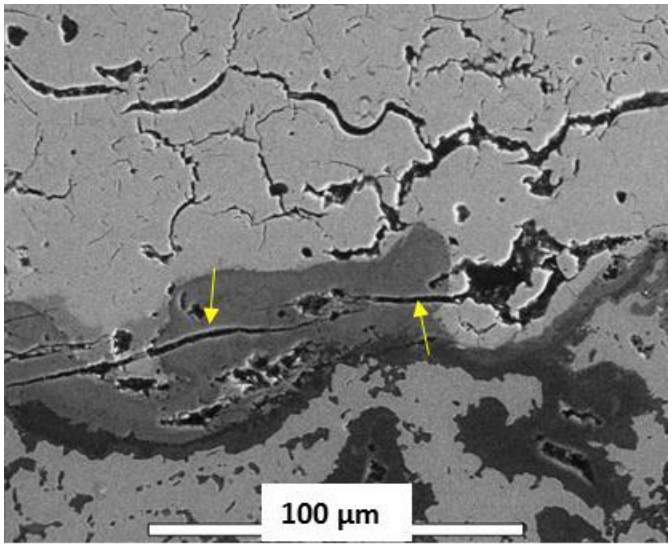

Figure 3.20 - Horizontal cracking in non-α-Al_2O_3 is characteristically different than cracking in YSZ (oxidation test sample after 200 hours at 2100 ˚F)

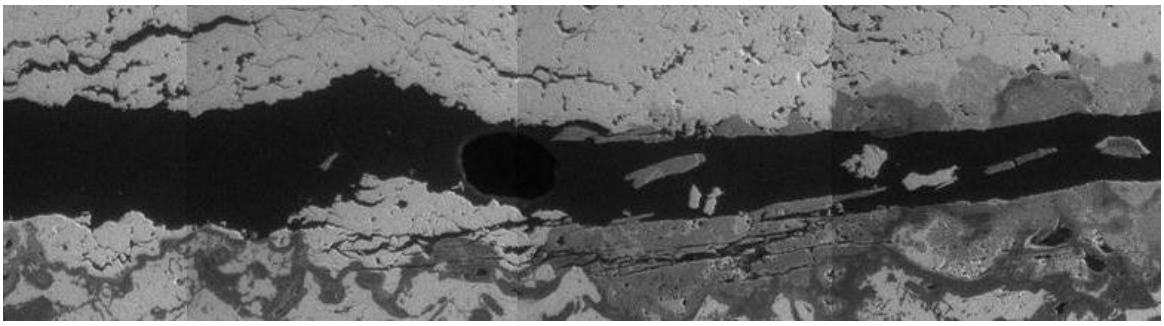

Figure 3.21 - Crack propagating through a region of non-α-Al_2O_3 (spalled oxidation sample after 300 hours at 1149 ˚C, 250x)

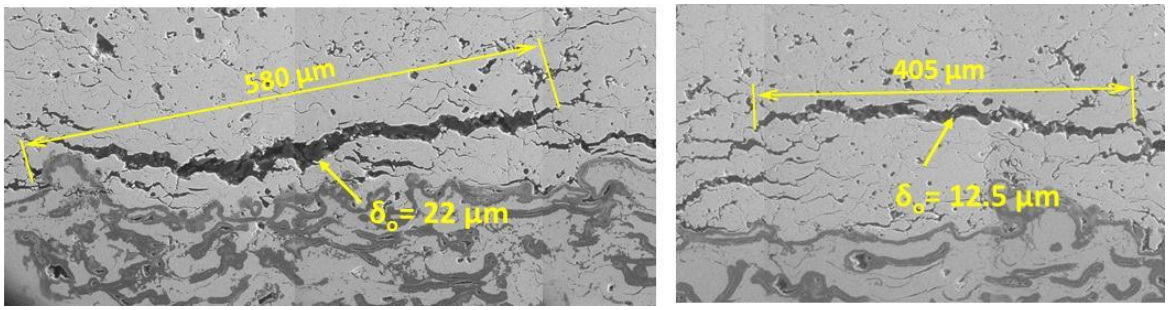

Figure 3.22 – Crack opening displacements after (a.) 450 hrs at 2000 ˚F (left,) and (b.) 350 hrs at 2000 ˚F (right)

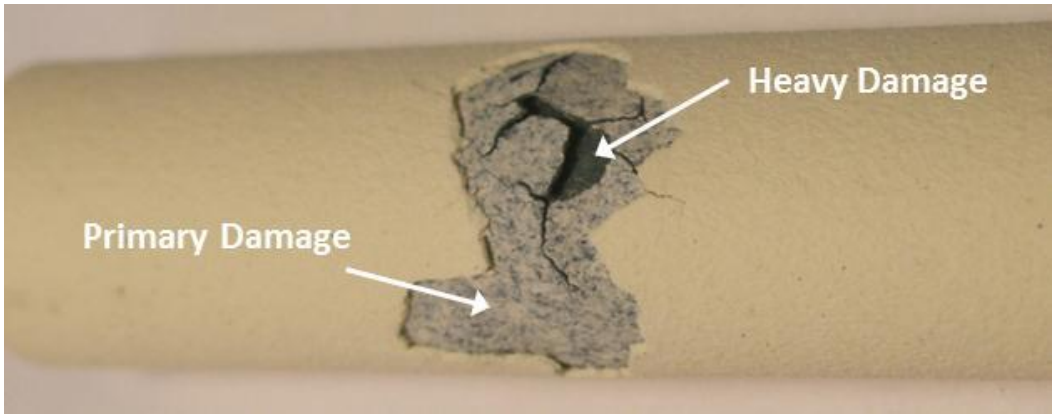

Figure 3.23 – Burner rig sample shows a heavily damaged region along with a region of damage consistent with oxidation test samples

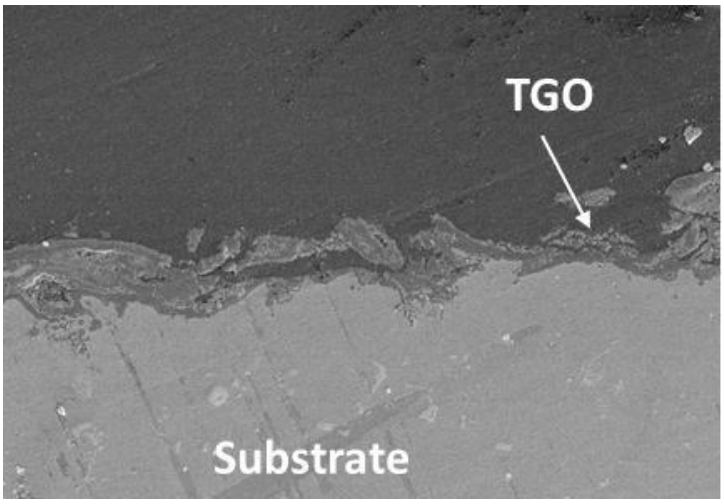

Figure 3.24 – TGO growth directly on substrate indicates continued loading after coating had failed

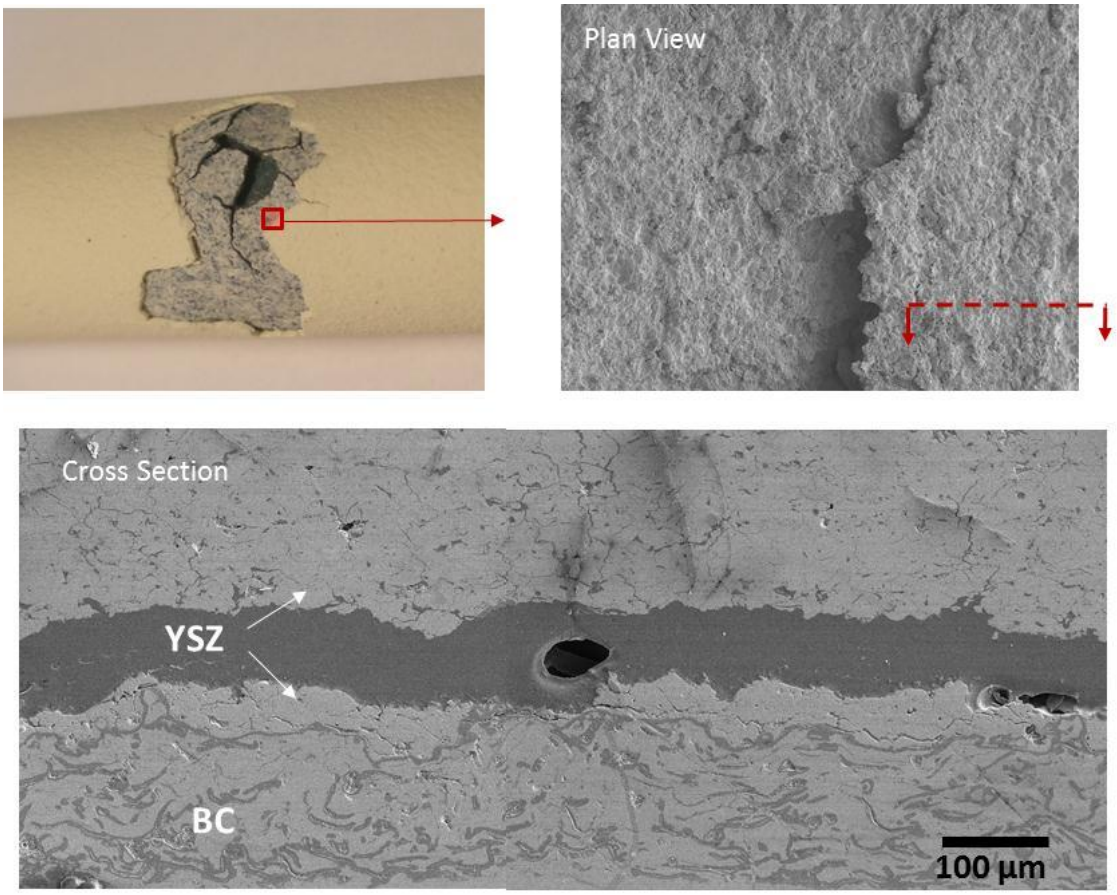

Figure 3.25 – Plan view micrograph (top right) of the area indicated in photo (top left) shows the location of the cross section micrograph (bottom)

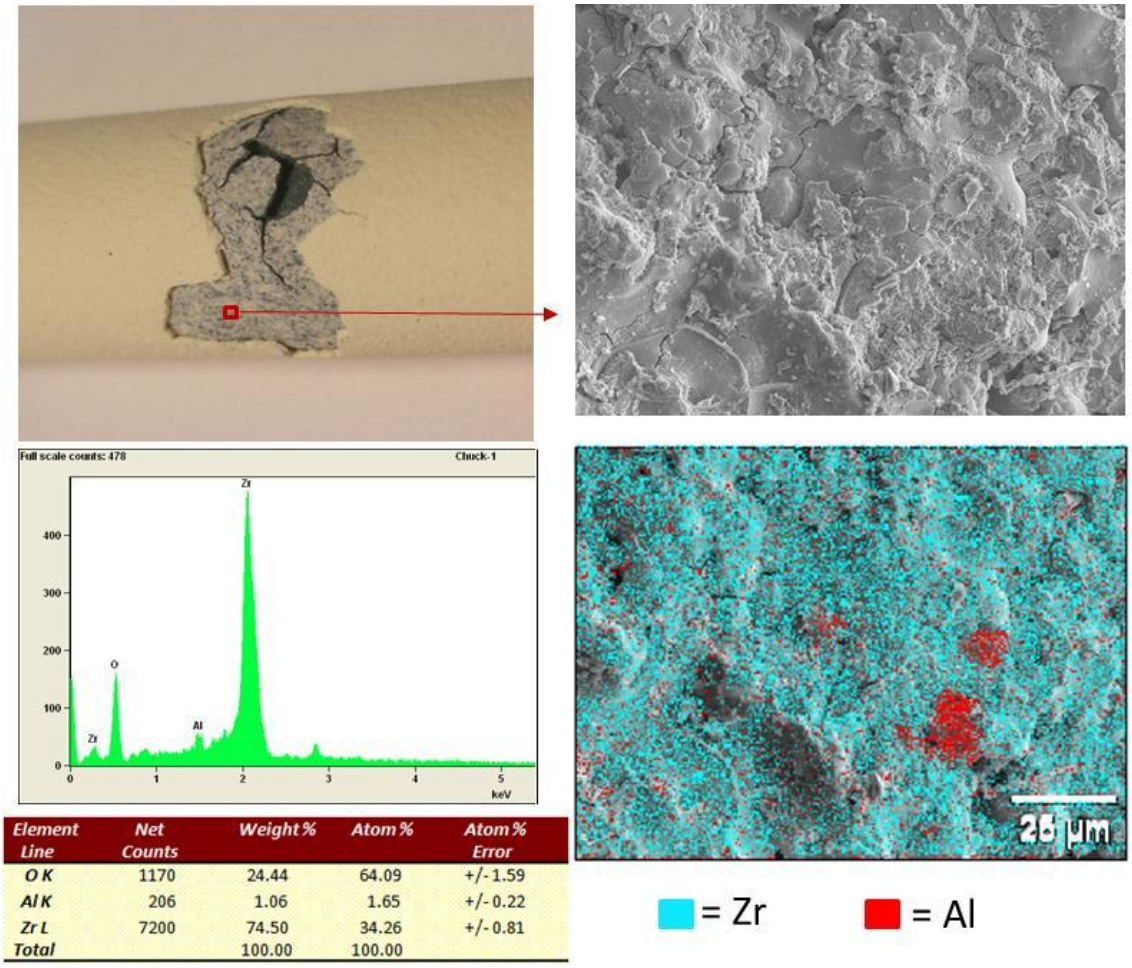

Figure 3.26 – EDX element map (bottom right) of the surface shown in micrograph (top right) located in area indicated in photo (top left); EDX spectrum and approximate elemental compositions are also given (bottom left)

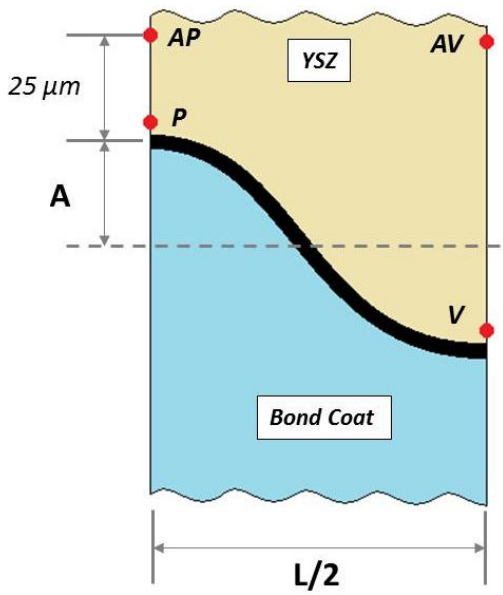

Figure 3.27 – Locations for stress outputs in the YSZ: peak (P), valley (V), above peak (AP), and above valley (AV)

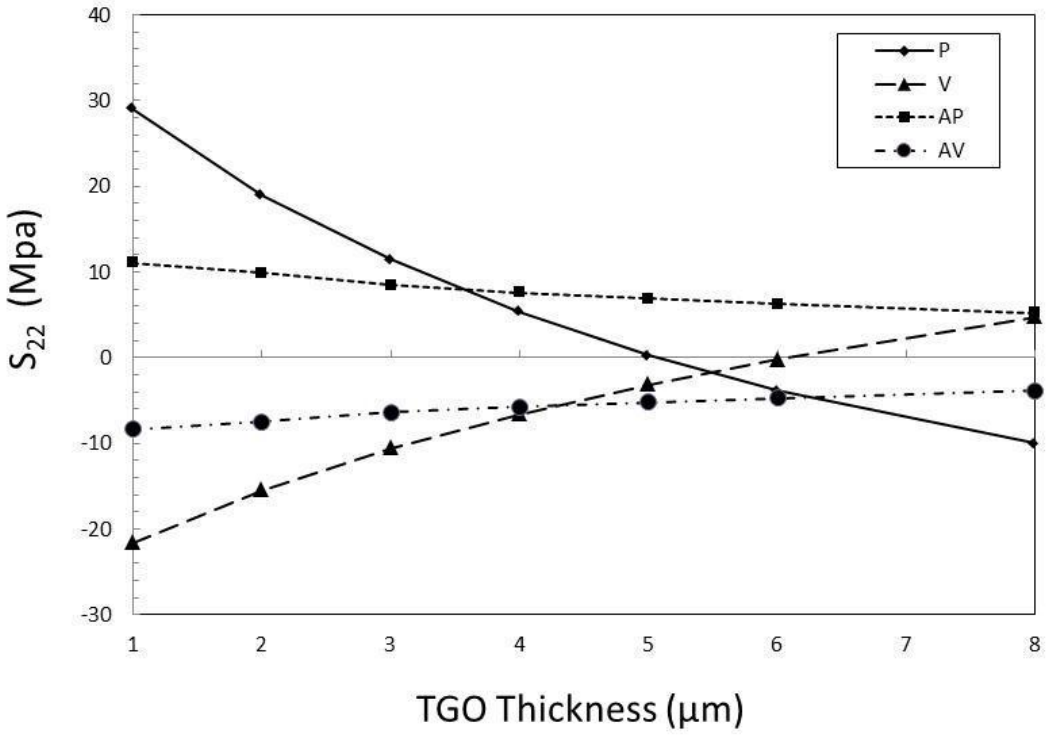

Figure 3.28 – Out-of-plane stress at 4 locations for the 'thermal mismatch only' case

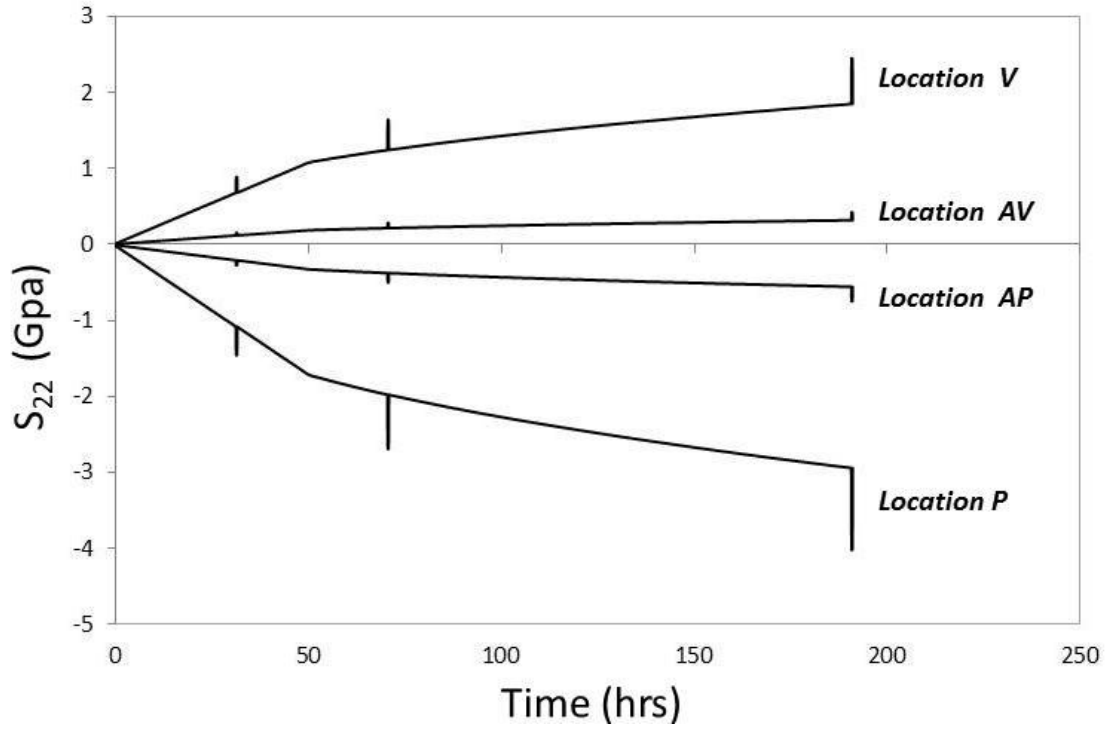

Figure 3.29 – Out-of-plane stress vs. time at 4 locations for the 'TGO growth only' case (YSZ linear elastic)

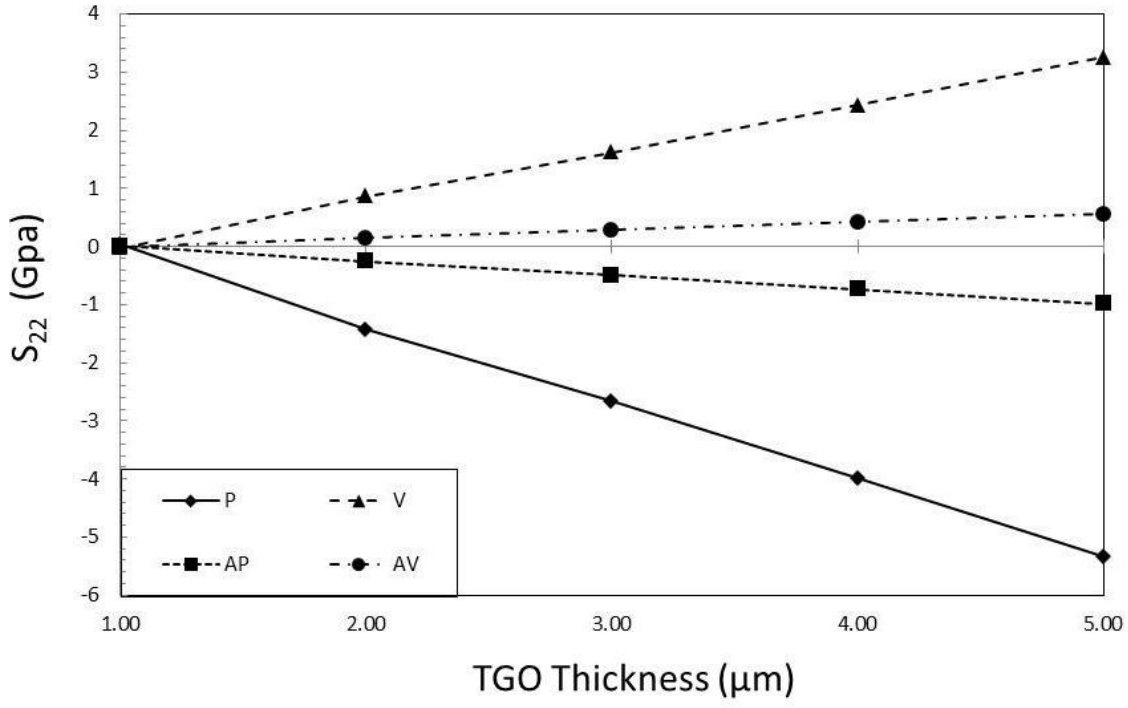

Figure 3.30 – Out-of-plane stress vs. TGO thickness at 4 locations for the 'TGO growth only' case (YSZ linear elastic)

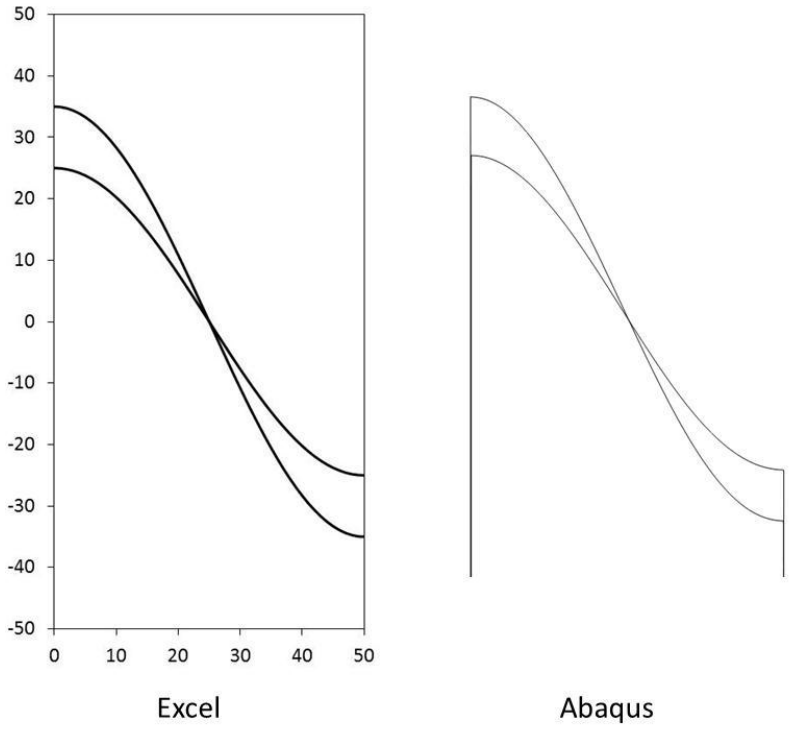

Figure 3.31 – Amplitude change due to tortuosity drawn in Excel (left) and implemented in Abaqus (right)

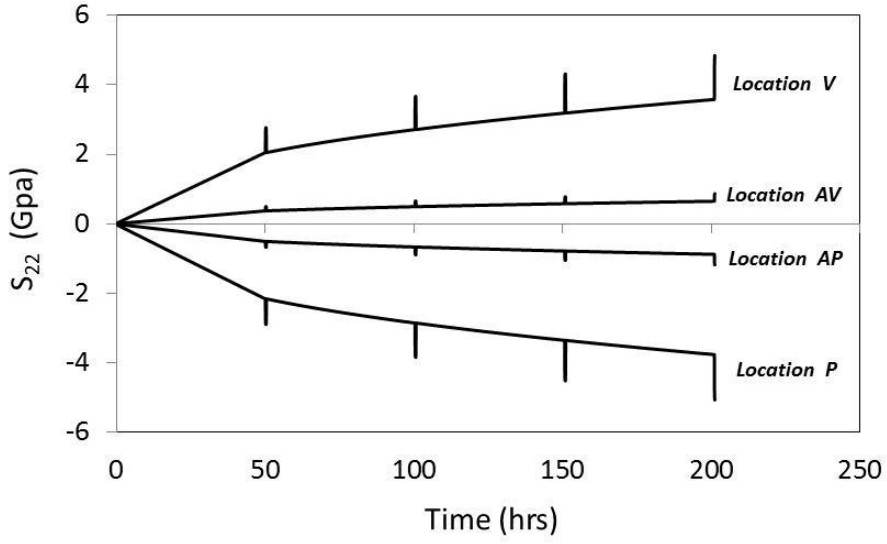

Figure 3.32 – Out-of-plane stress vs. time at 4 locations for the 'bond coat rumpling only' case (YSZ linear elastic)

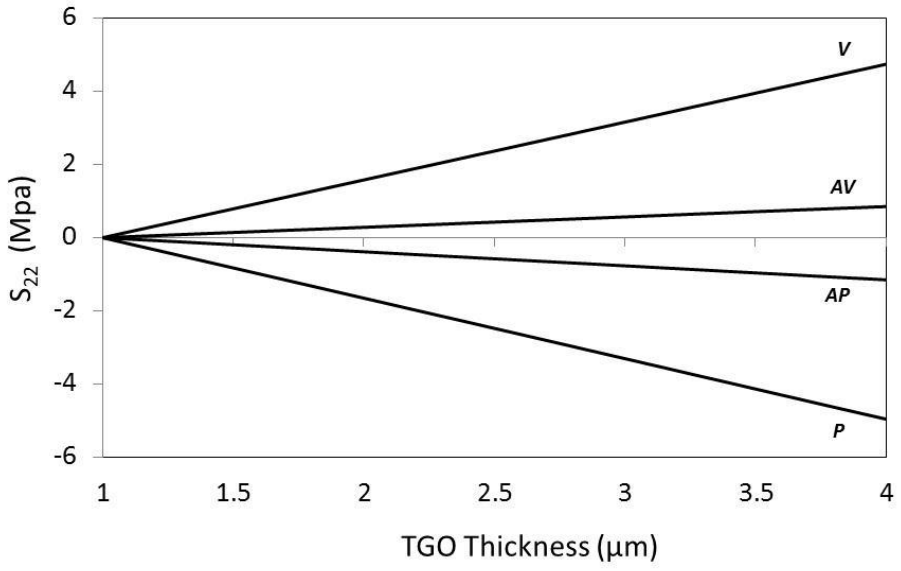

Figure 3.33 – Out-of-plane stress vs. TGO thickness at 4 locations for the 'bond coat rumpling only' case (YSZ linear elastic)

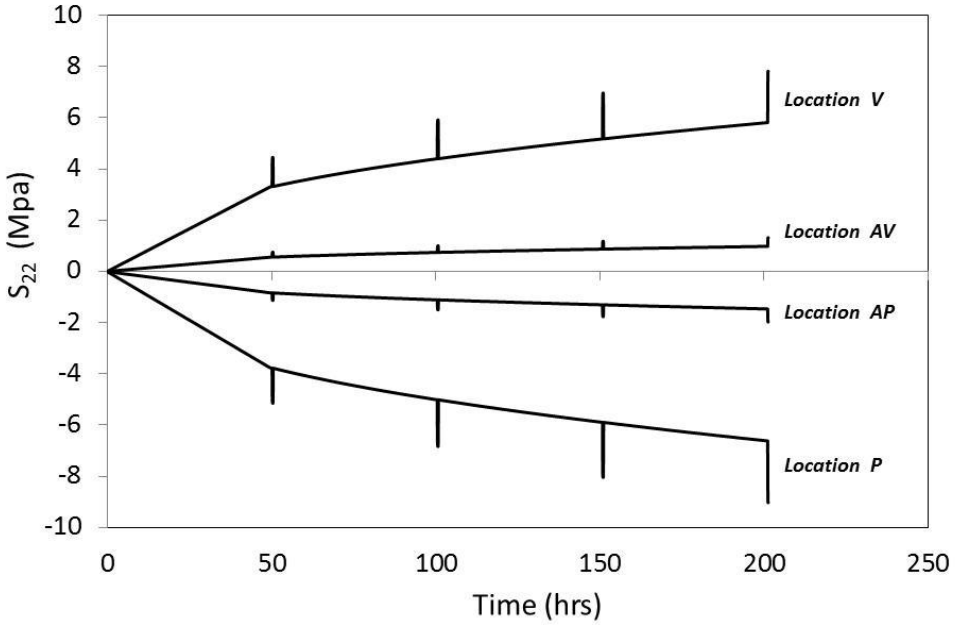

Figure 3.34 – Out-of-plane stress vs. time at 4 locations for the 'bond coat rumpling with TGO growth' case (YSZ linear elastic)

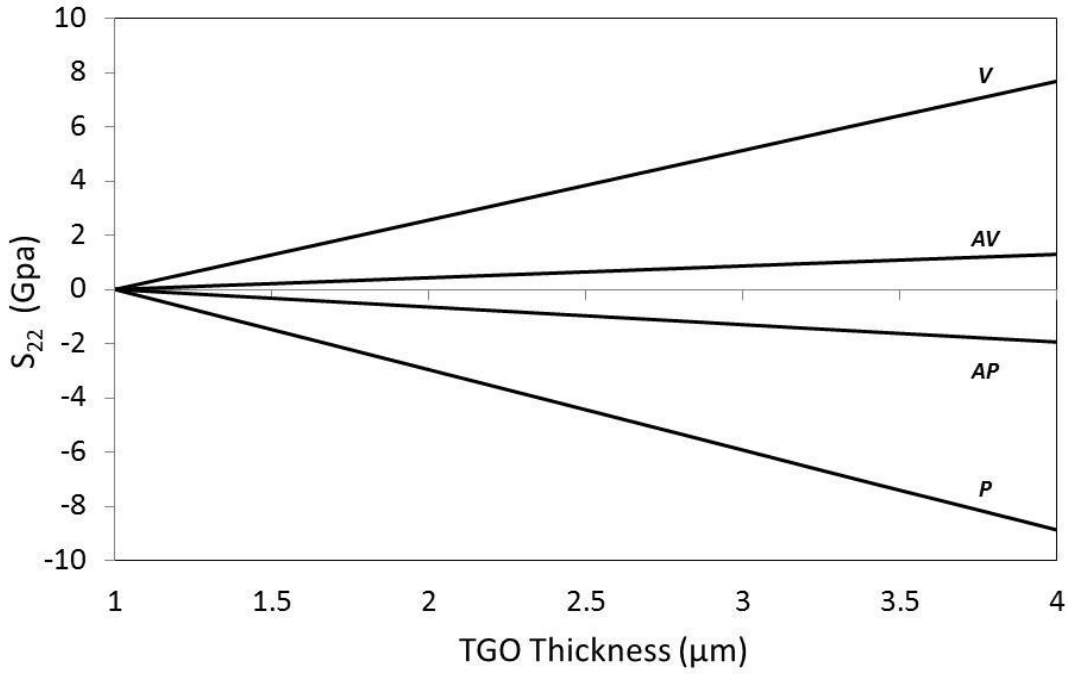

Figure 3.35 – Out-of-plane stress vs. TGO thickness at 4 locations for the 'bond coat rumpling with TGO growth' case (YSZ linear elastic)

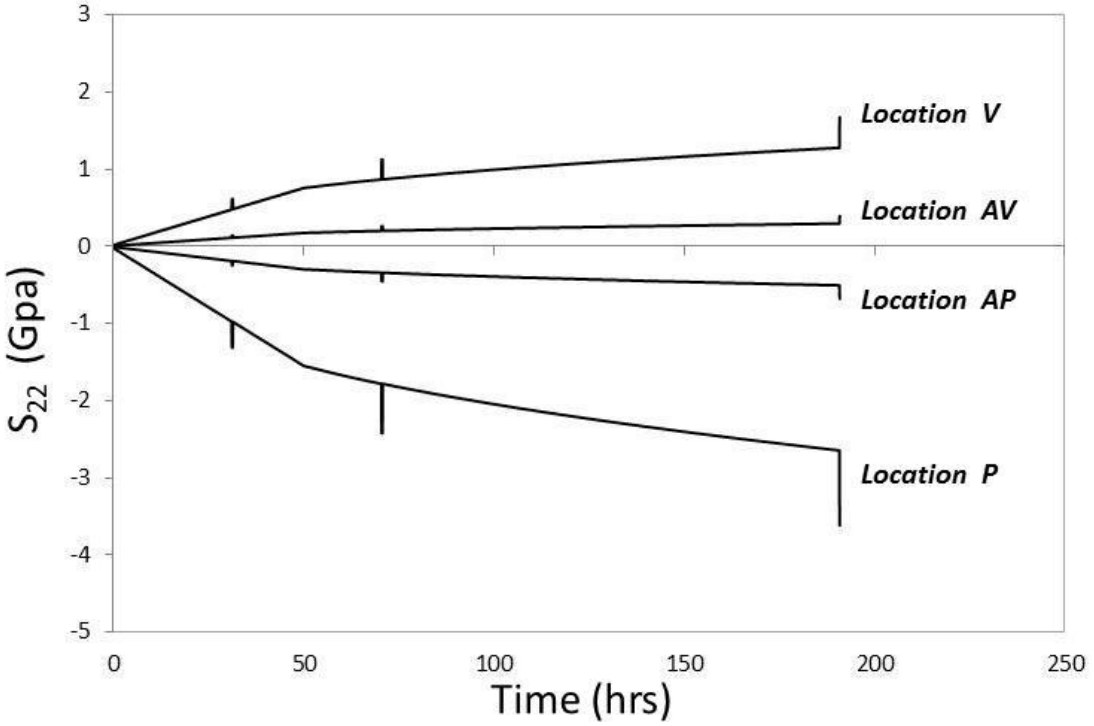

Figure 3.36 – Out-of-plane stress vs. time at 4 locations for the 'TGO growth with bond coat Al depletion' case (YSZ linear elastic)

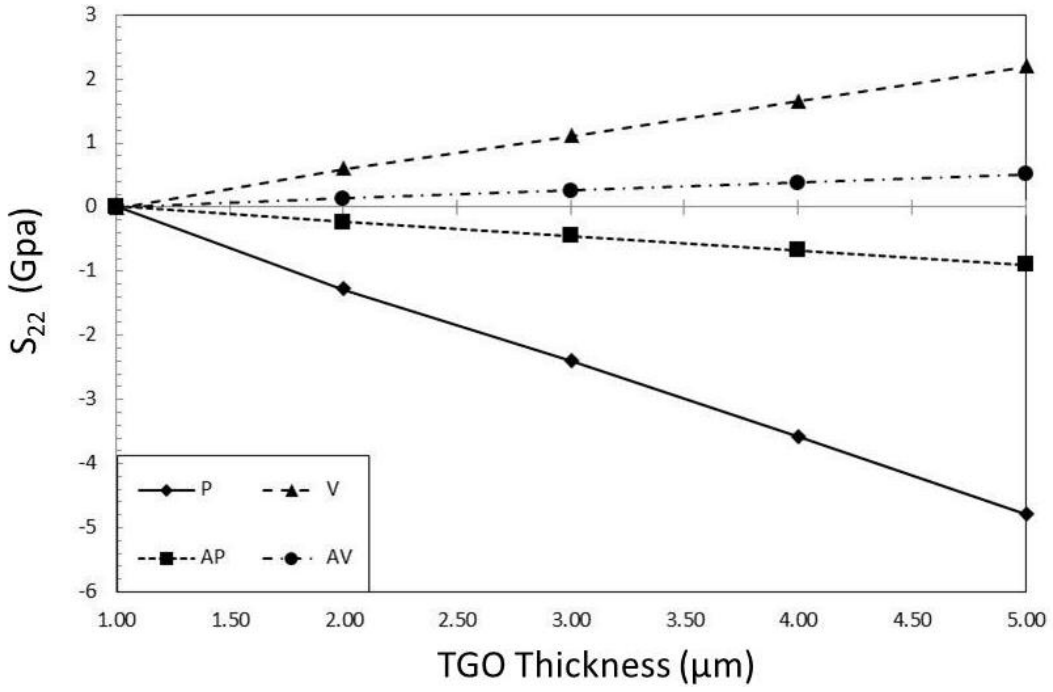

Figure 3.37 – Out-of-plane stress vs. time at 4 locations for the 'TGO growth with bond coat Al depletion' case (YSZ linear elastic)

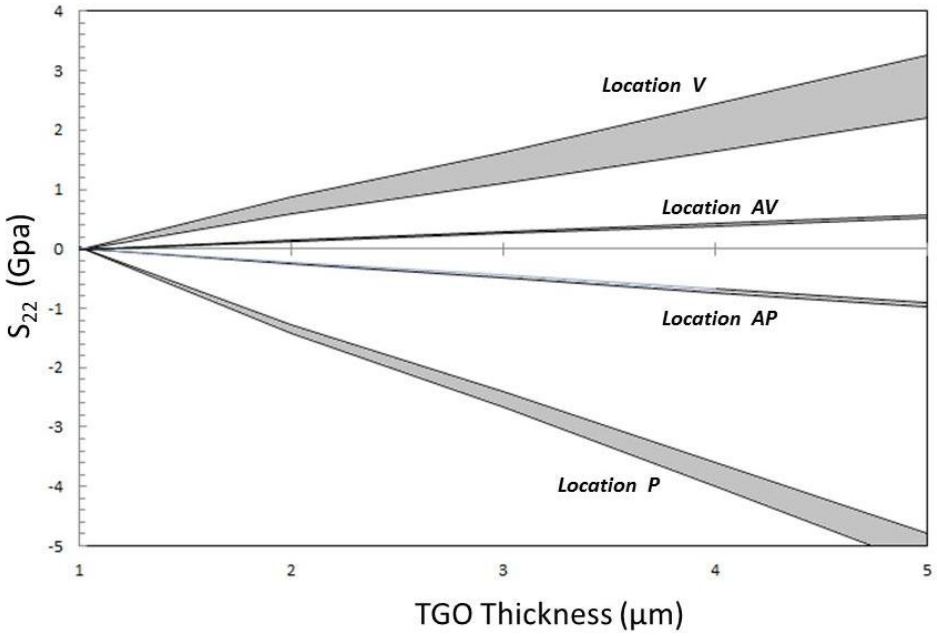

Figure 3.38 – Comparison of the 'TGO growth with bond coat Al depletion' case and the 'TGO growth only case' (YSZ linear elastic); the larger magnitude stresses are from the 'TGO growth only' case

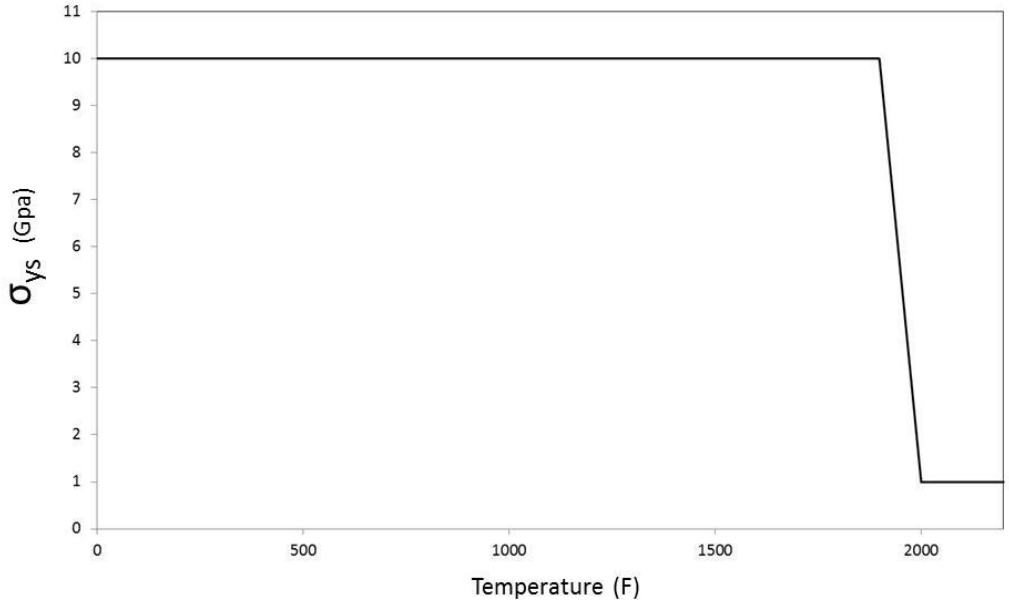

Figure 3.39 – Temperature dependent TGO yield stress used to incorporate perfect TGO plasticity into model

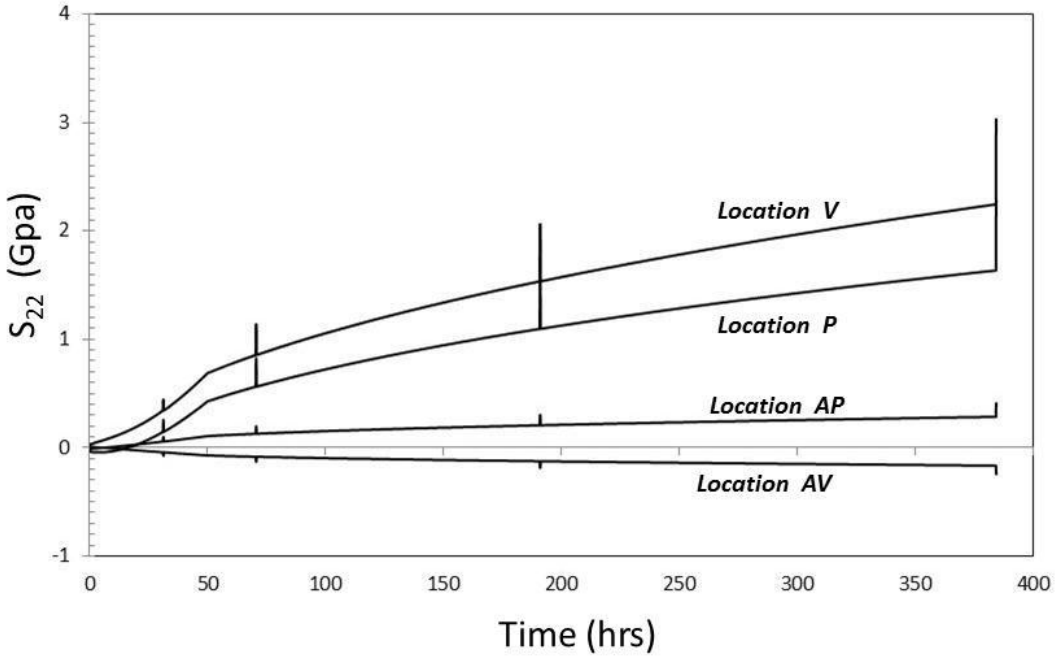

Figure 3.40 – Out-of-plane stress vs. time at 4 locations for the 'TGO growth with TGO plasticity' case (YSZ linear elastic)

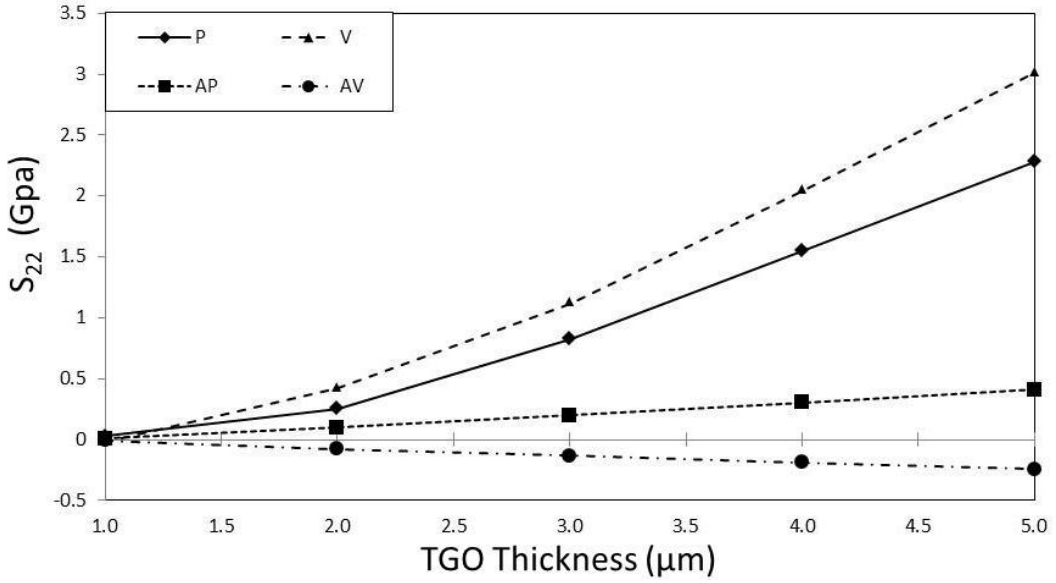

Figure 3.41 – Out-of-plane stress vs. TGO thickness at 4 locations for the 'TGO growth with TGO plasticity' case (YSZ linear elastic)

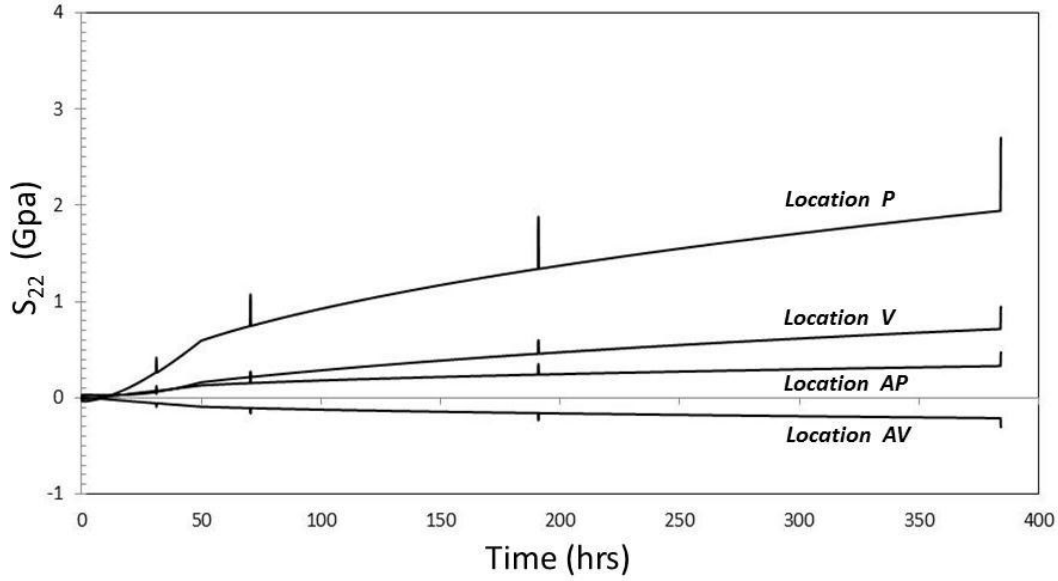

Figure 3.42 – Out-of-plane stress vs. time at 4 locations for the 'TGO growth, bond coat Al depletion, and TGO plasticity' case (YSZ linear elastic)

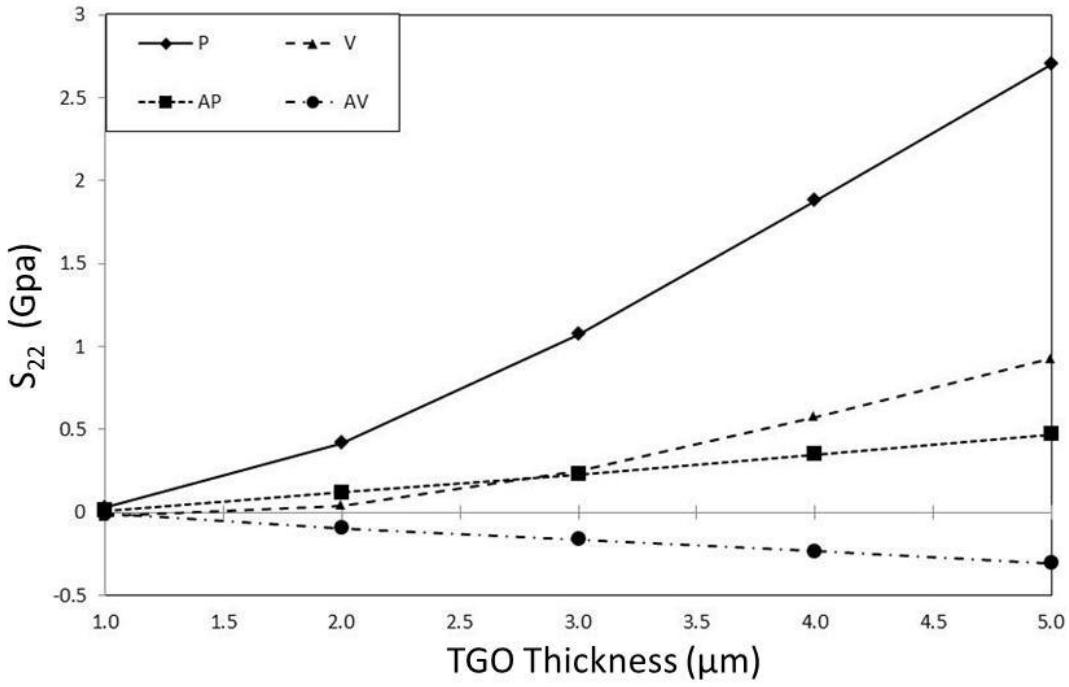

Figure 3.43 – Out-of-plane stress vs. TGO thickness at 4 locations for the 'TGO growth, bond coat Al depletion, and TGO plasticity' case (YSZ linear elastic)

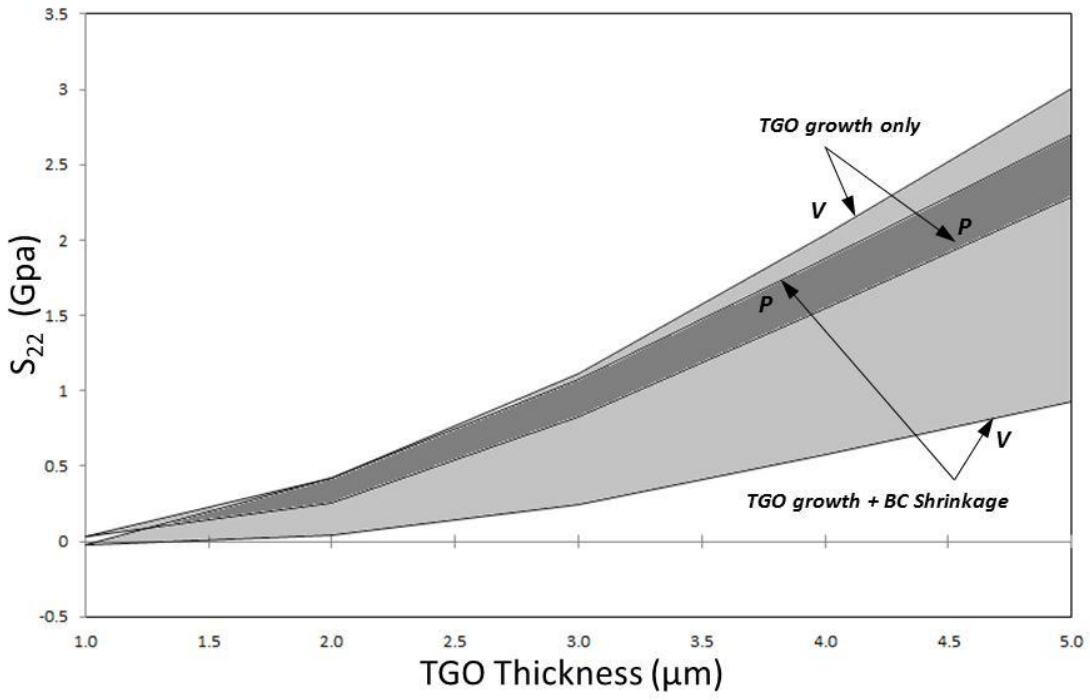

Figure 3.44 – Comparison of the 'TGO growth with TGO plasticity' case and the 'TGO growth, bond coat Al depletion, and TGO growth case (YSZ linear elastic)

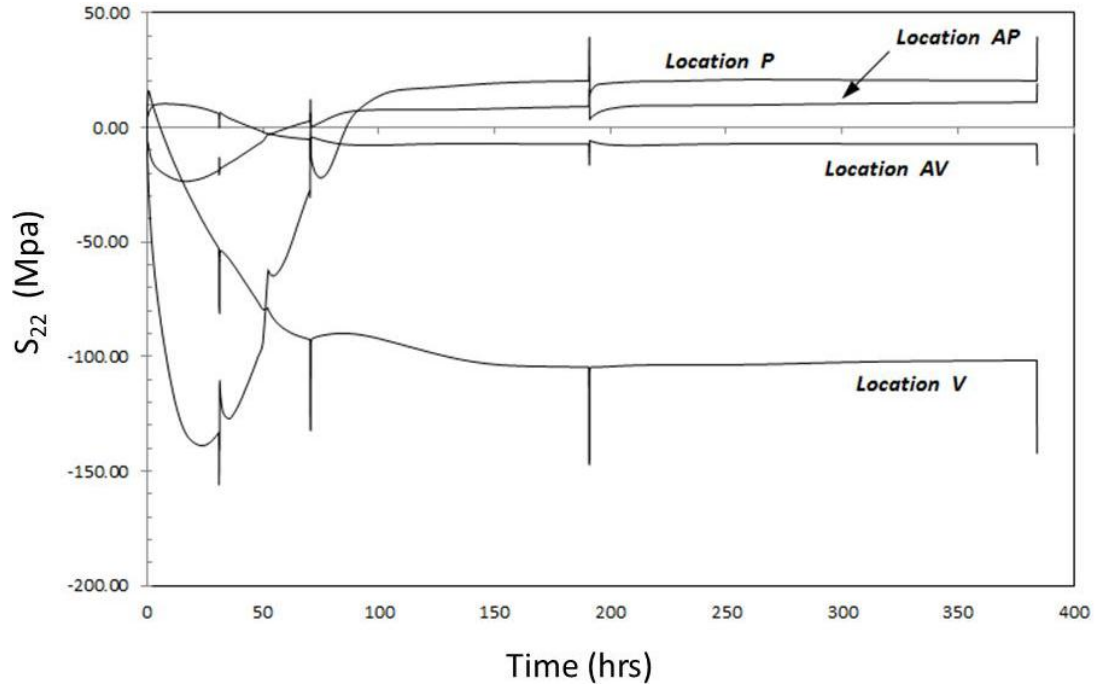

Figure 3.45 – Out-of-plane stress vs. time at 4 locations for the 'TGO growth only' case (YSZ viscoplastic)

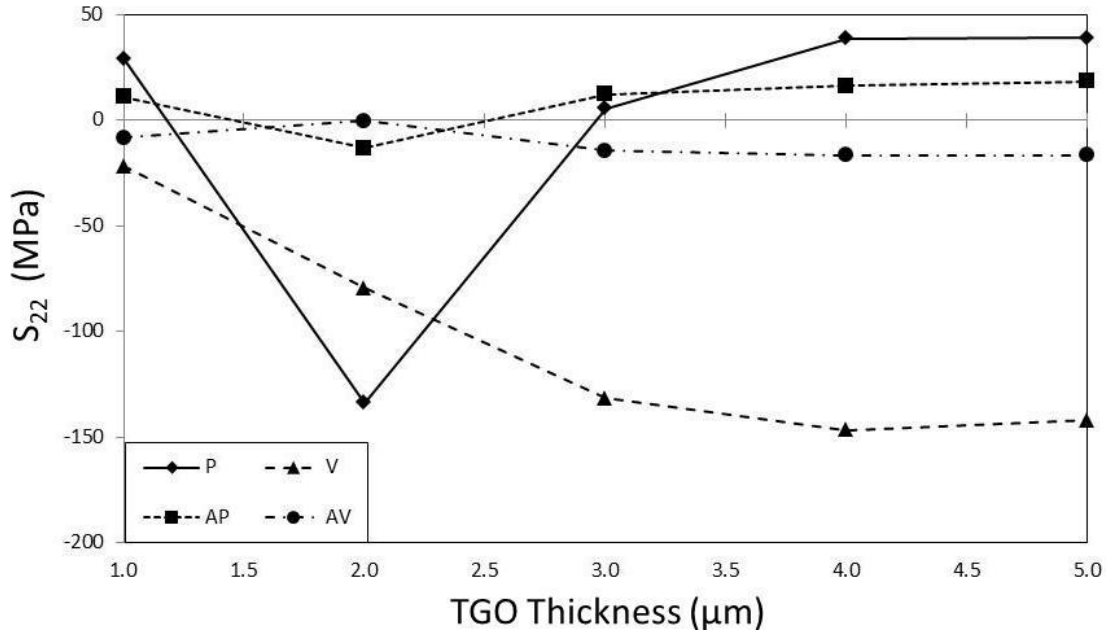

Figure 3.46 – Out-of-plane stress vs. TGO thickness at 4 locations for the 'TGO growth only' case (YSZ viscoplastic)

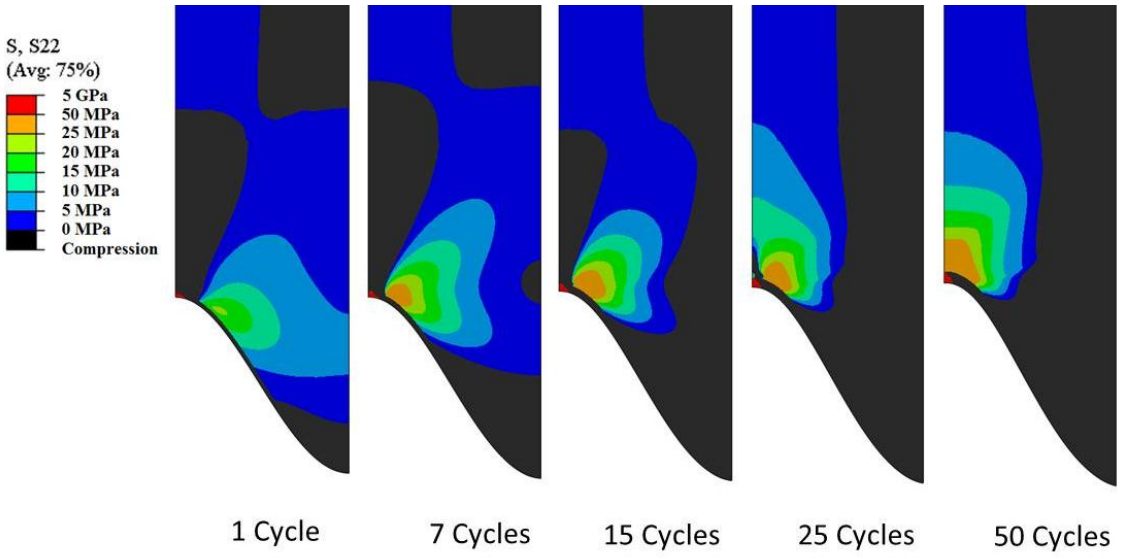

Figure 3.47 – Contour plots of the out-of-plane tension for the 'TGO growth only' case (cycle durations of 4 hours)

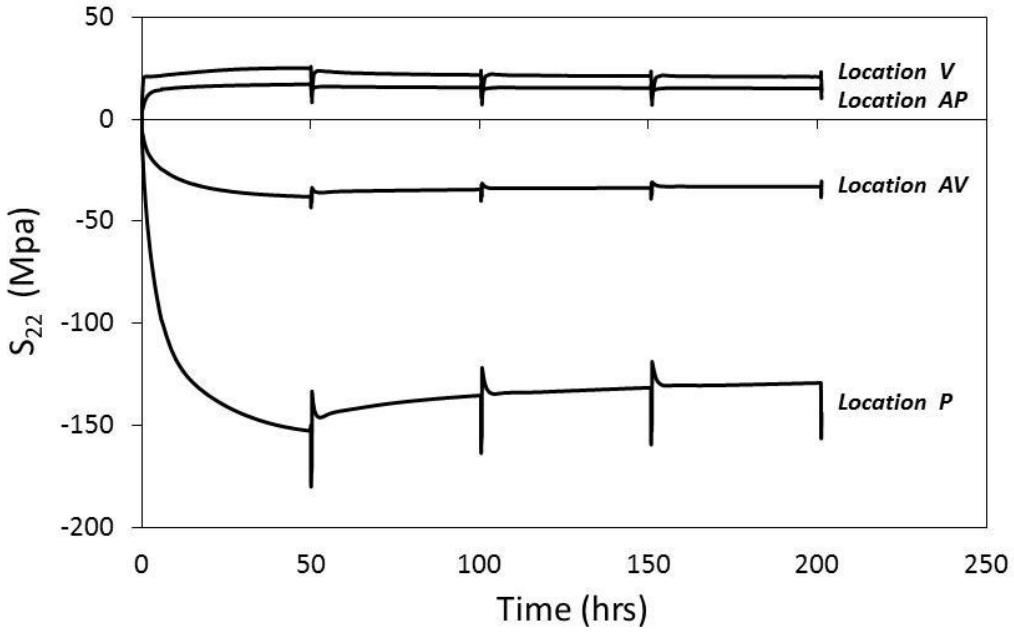

Figure 3.48 – Out-of-plane stress vs. time at 4 locations for the 'bond coat rumpling only' case (YSZ viscoplastic)

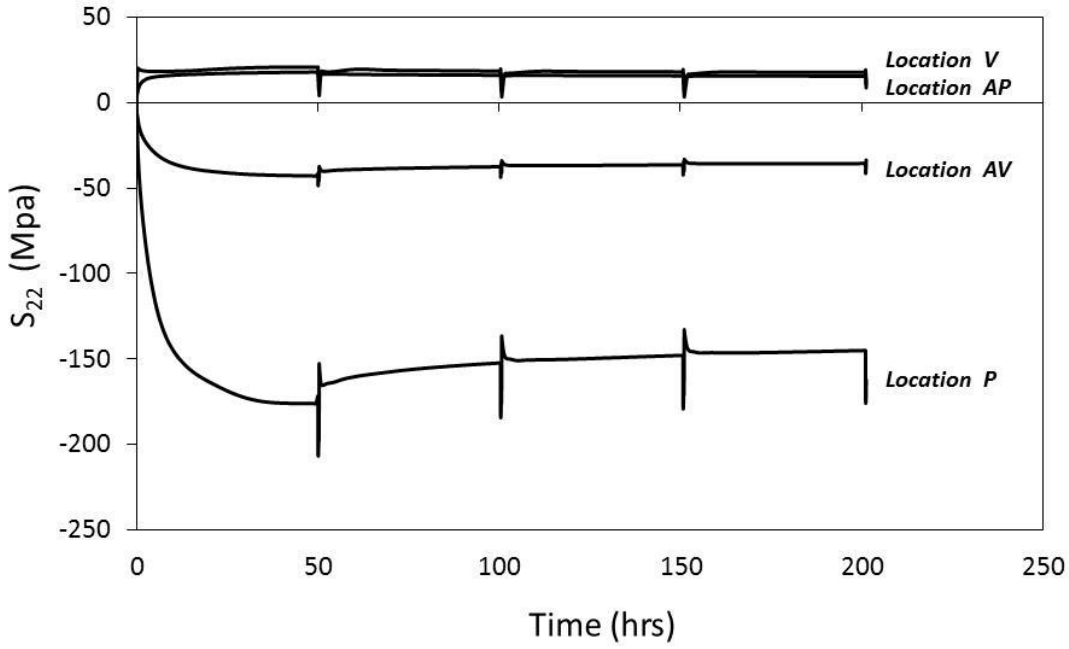

Figure 3.49 – Out-of-plane stress vs. time at 4 locations for the 'bond coat rumpling with TGO growth' case (YSZ viscoplastic)

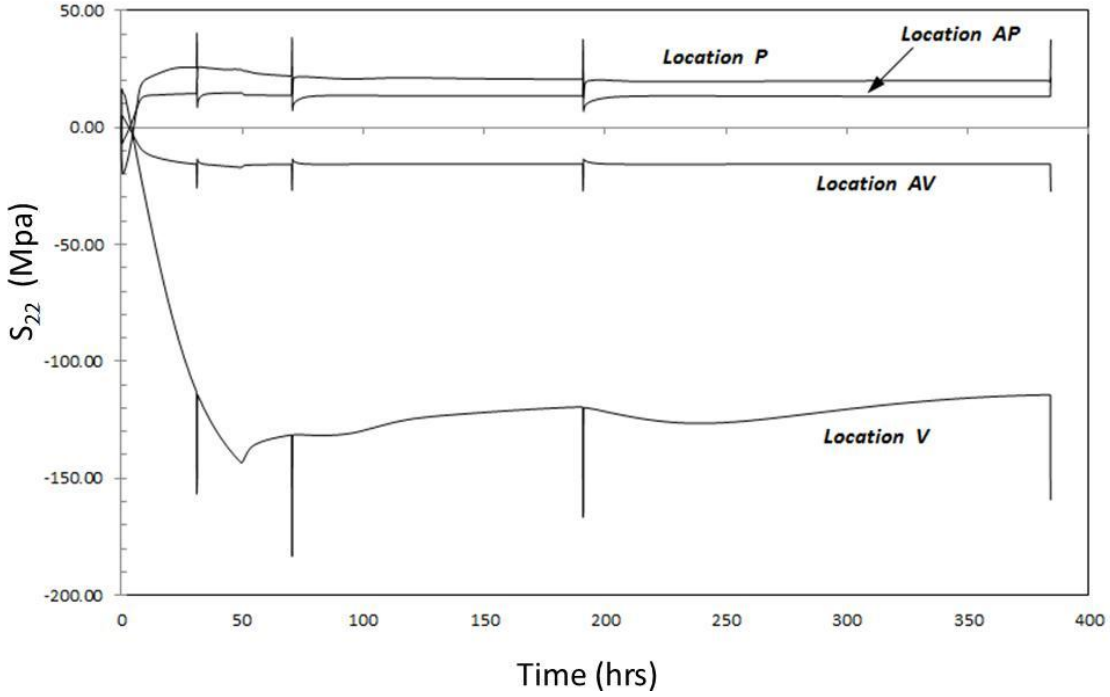

Figure 3.50 – Out-of-plane stress vs. time at 4 locations for the 'TGO growth with TGO plasticity' case (YSZ viscoplastic)

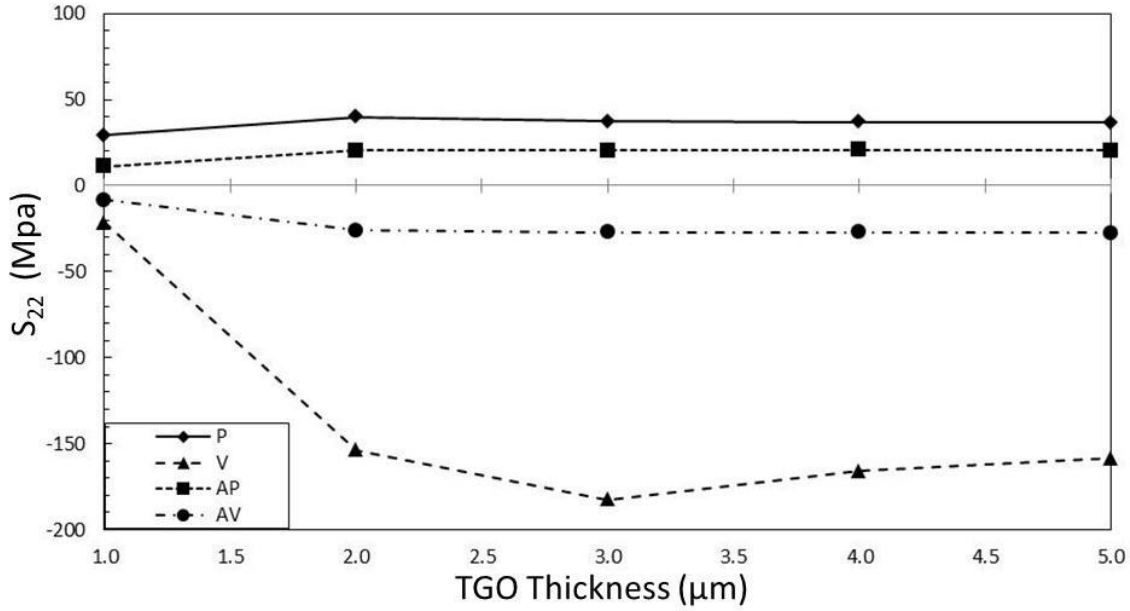

Figure 3.51 – Out-of-plane stress vs. TGO thickness at 4 locations for the 'TGO growth with TGO plasticity' case (YSZ viscoplastic)

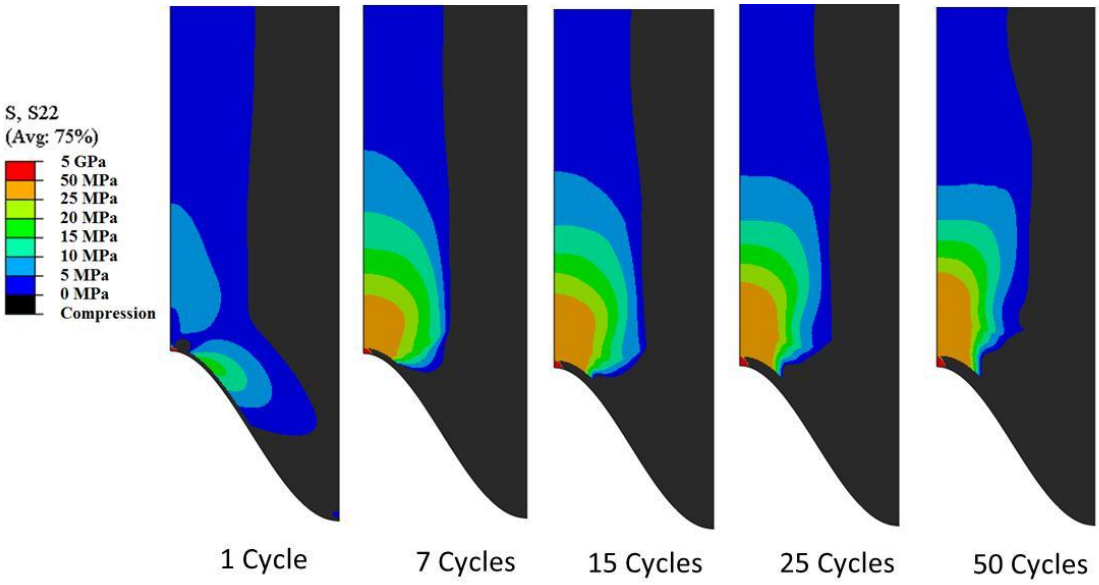

Figure 3.52 – Contour plots of the out-of-plane tension for the 'TGO growth with TGO plasticity' case (cycle durations of 4 hours)

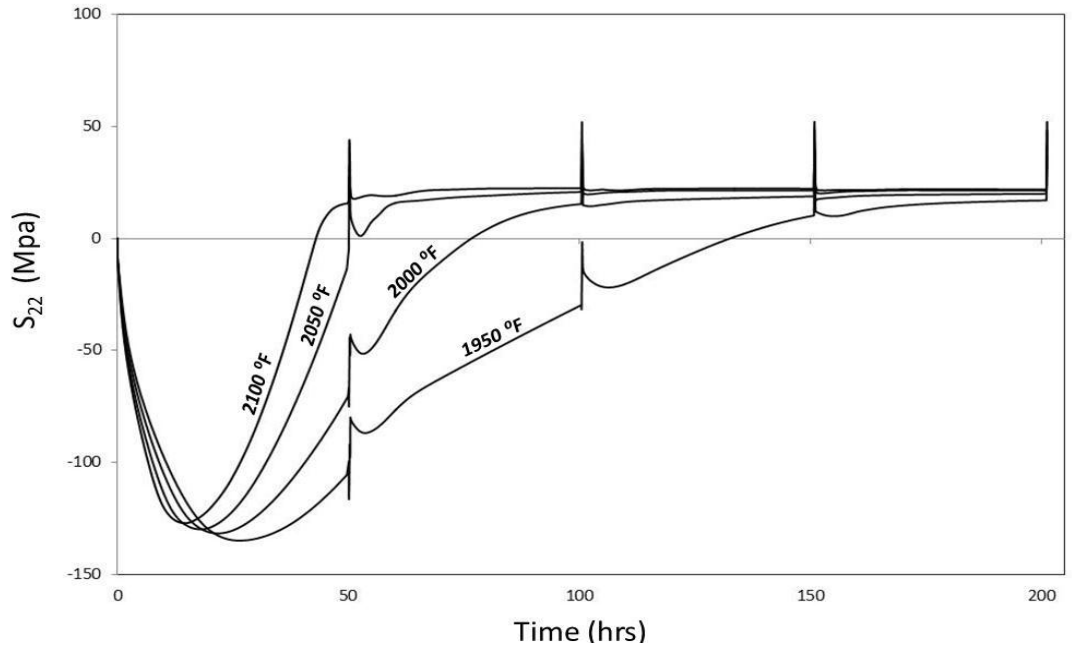

Figure 3.53 – Out-of-plane stress vs. time at location P for different temperatures and a constant cycle duration of 50 hours (TGO growth only, viscoplastic YSZ)

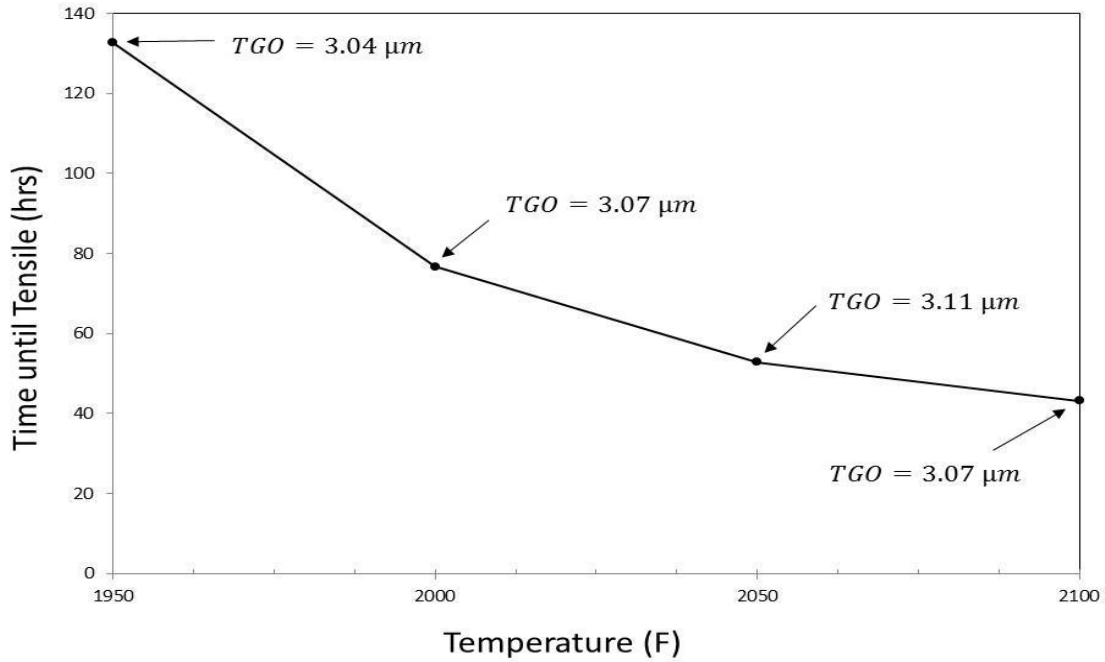

Figure 3.54 – Time until location P goes into tension as a function of temperature (50 hr cycle duration, TGO growth only, viscoplastic YSZ); TGO thicknesses at this time are indicated

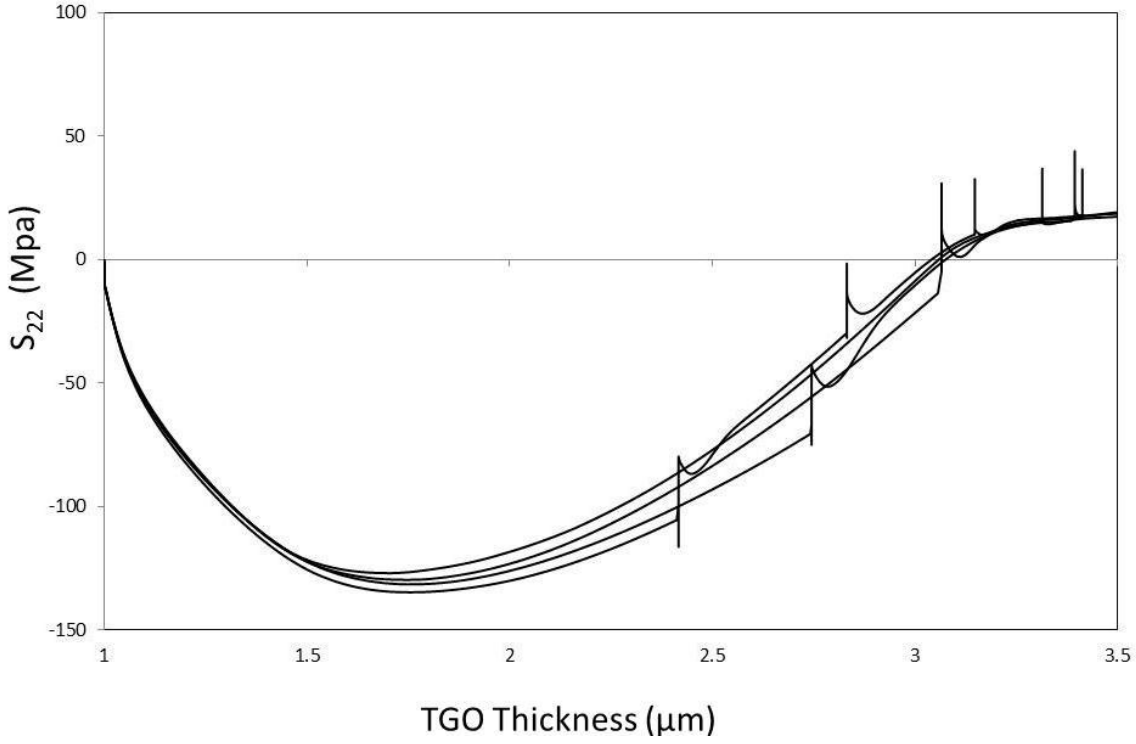

Figure 3.55 – Out-of-plane stress vs. TGO thickness at location P for different temperatures and constant cycle duration of 50 hours (TGO growth only, viscoplastic YSZ)

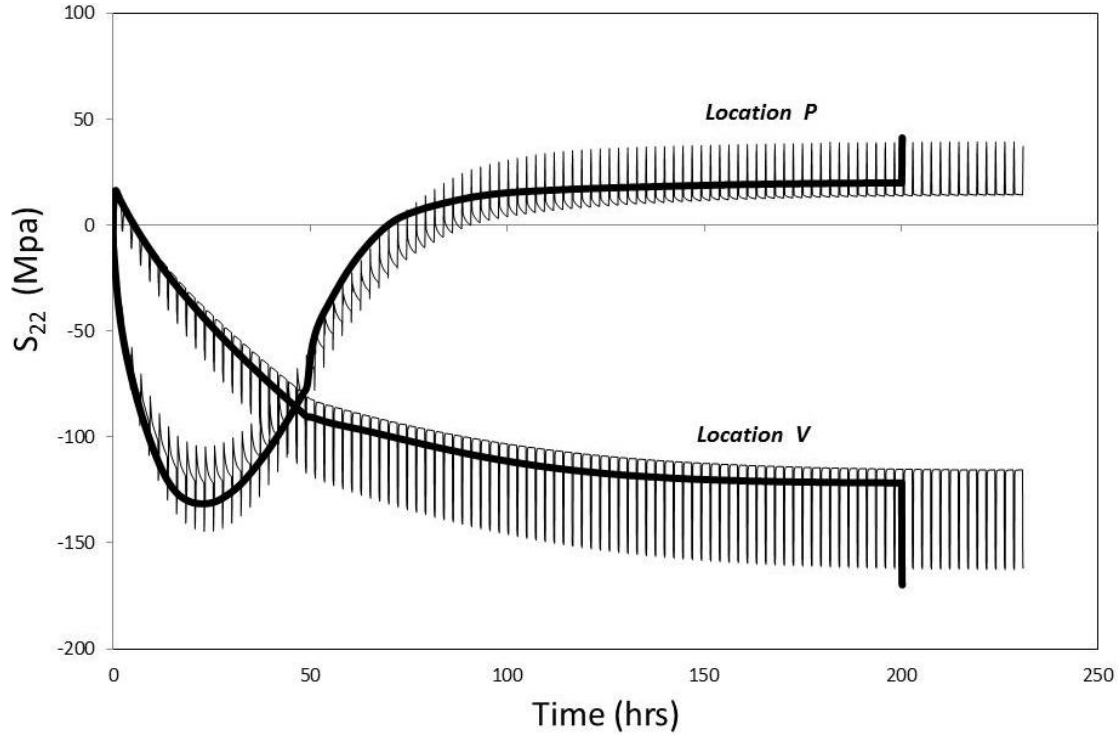

Figure 3.56 – Out-of-plane stress vs. time at locations P and V for cycle durations of 2 hours and 200 hours, both at 2000^{o}F (TGO growth only, viscoplastic YSZ)

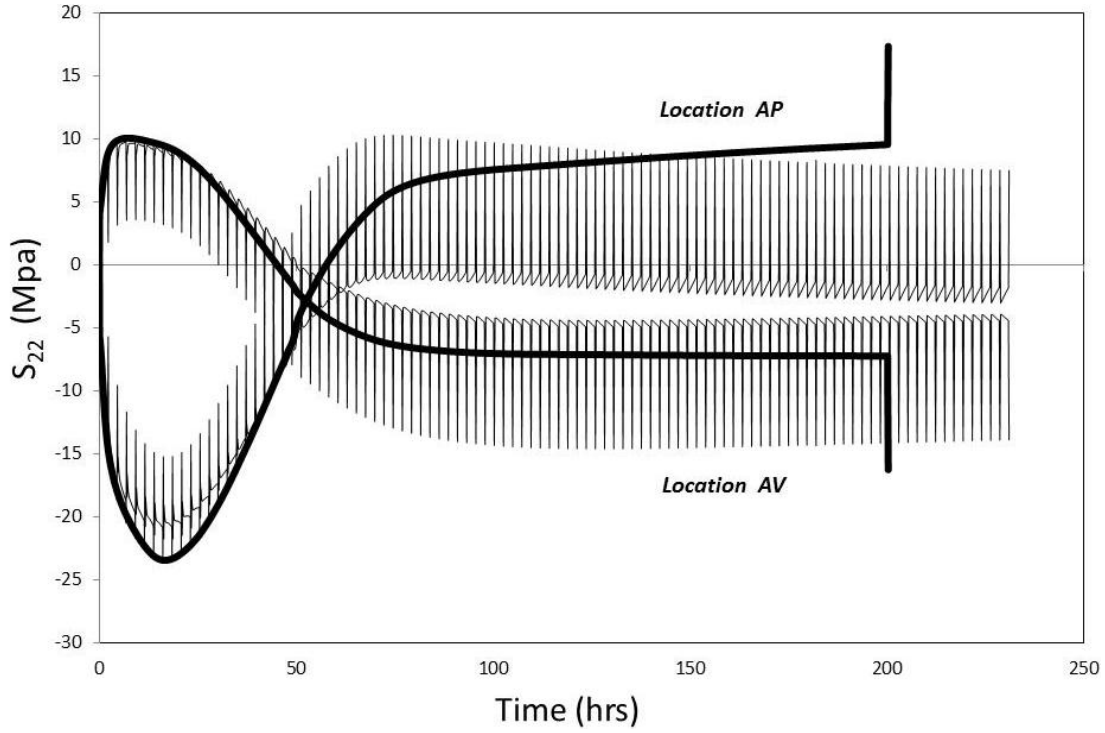

Figure 3.57 – Out-of-plane stress vs. time at locations AP and AV for cycle durations of 2 hours and 200 hours, both at 2000°F (TGO growth only, viscoplastic YSZ)

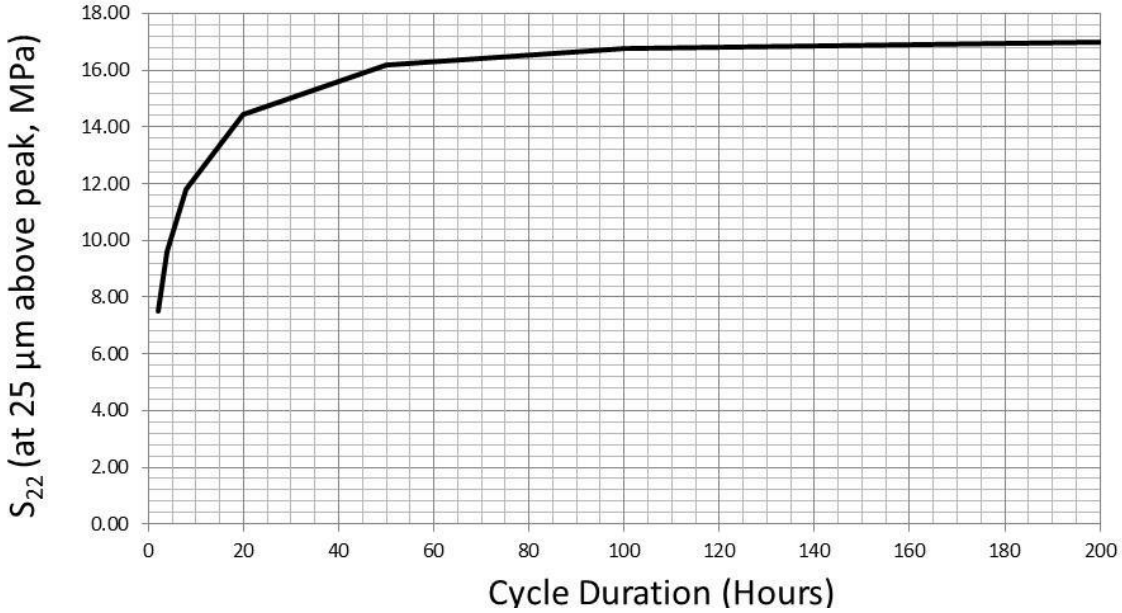

Figure 3.58 – Out-of-plane stress at location AP after 200 hours of hot time at 2000°F as a function of cycle duration (TGO growth only, viscoplastic YSZ)

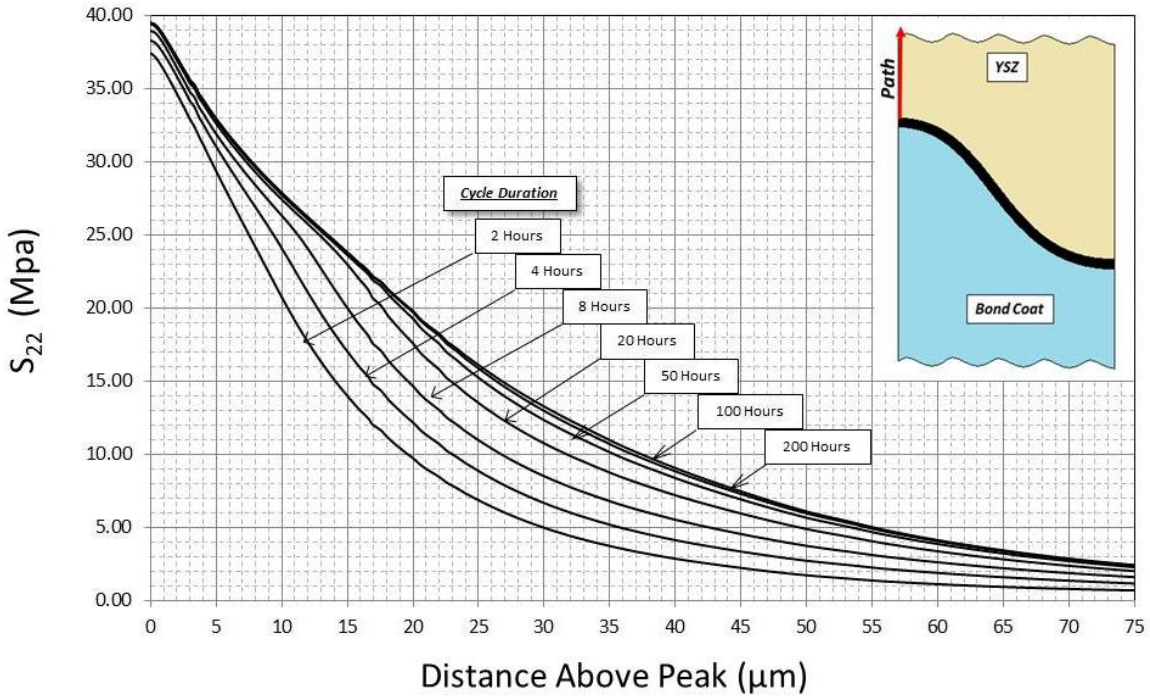

Figure 3.59 – Out-of-plane stress along path above peak upon cool down from 2000^{o}F at 200 hours for different cycle durations(TGO growth only, viscoplastic YSZ)

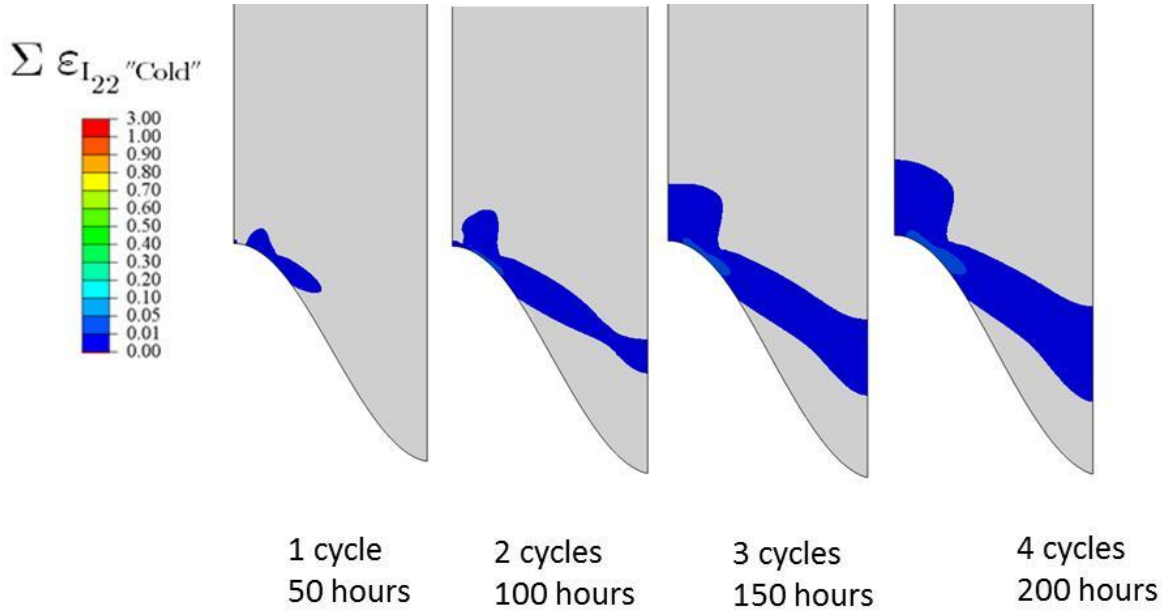

Figure 3.60 – Low temperature inelastic strain contours (1950^{o}F, 50 hr cycles, YSZ viscoplastic)

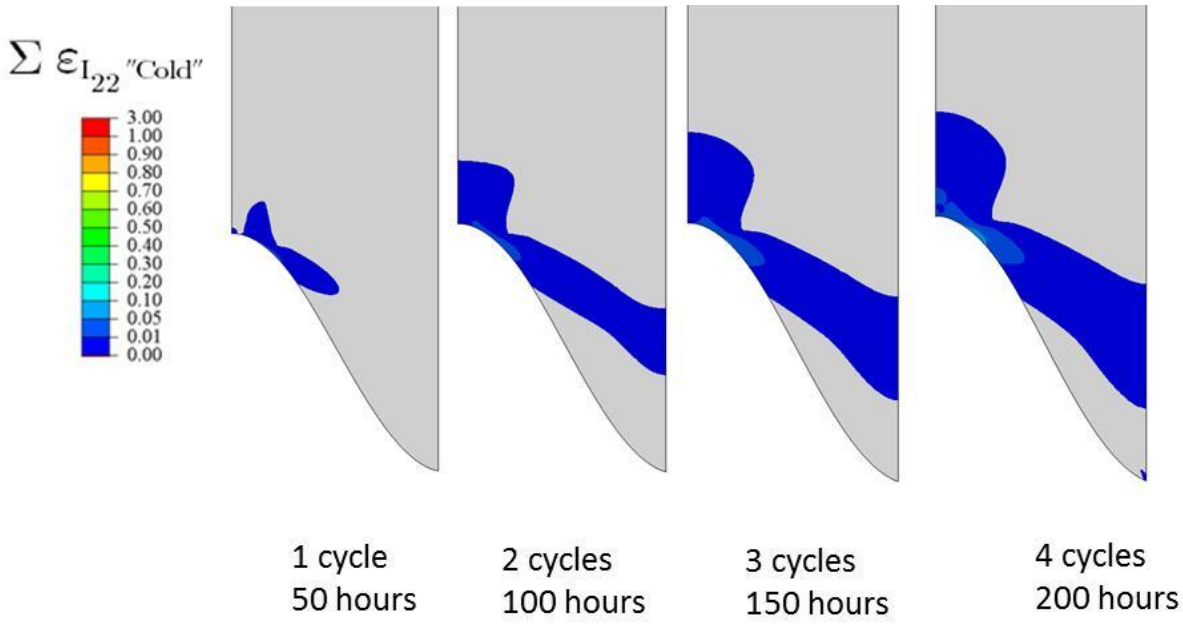

Figure 3.61 – Low temperature inelastic strain contours (2000^{o}F, 50 hr cycles, YSZ viscoplastic)

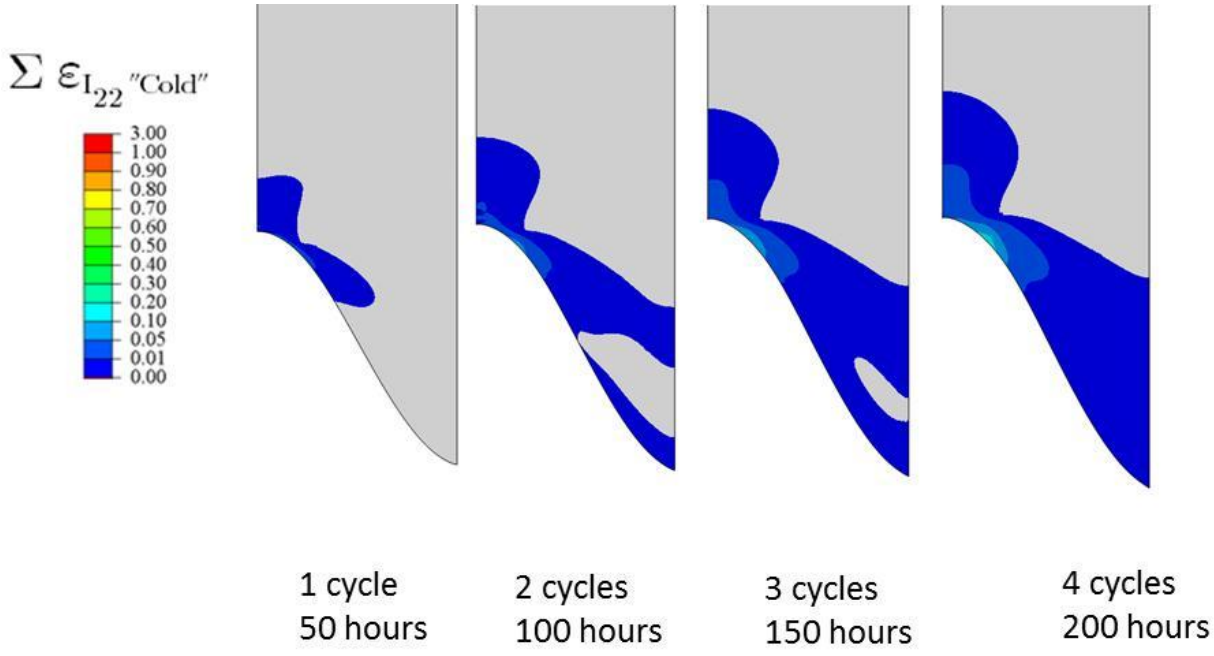

Figure 3.62 – Low temperature inelastic strain contours (2050^{o}F, 50 hr cycles, YSZ viscoplastic)

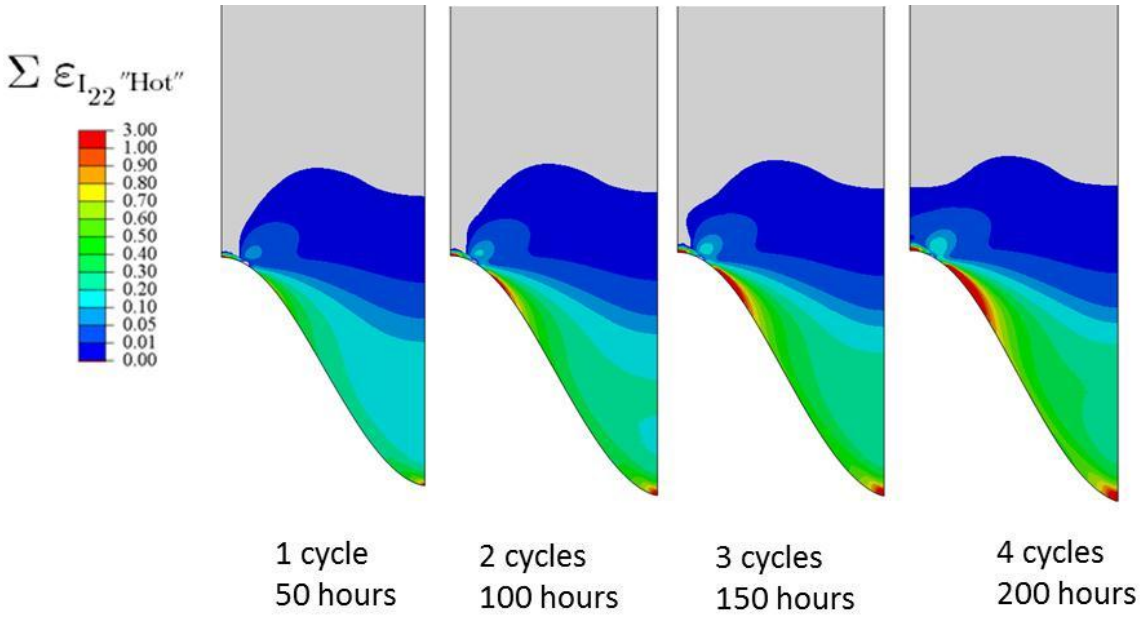

Figure 3.63 – High temperature inelastic strain contours (1950^{o}F, 50 hr cycles, YSZ viscoplastic)

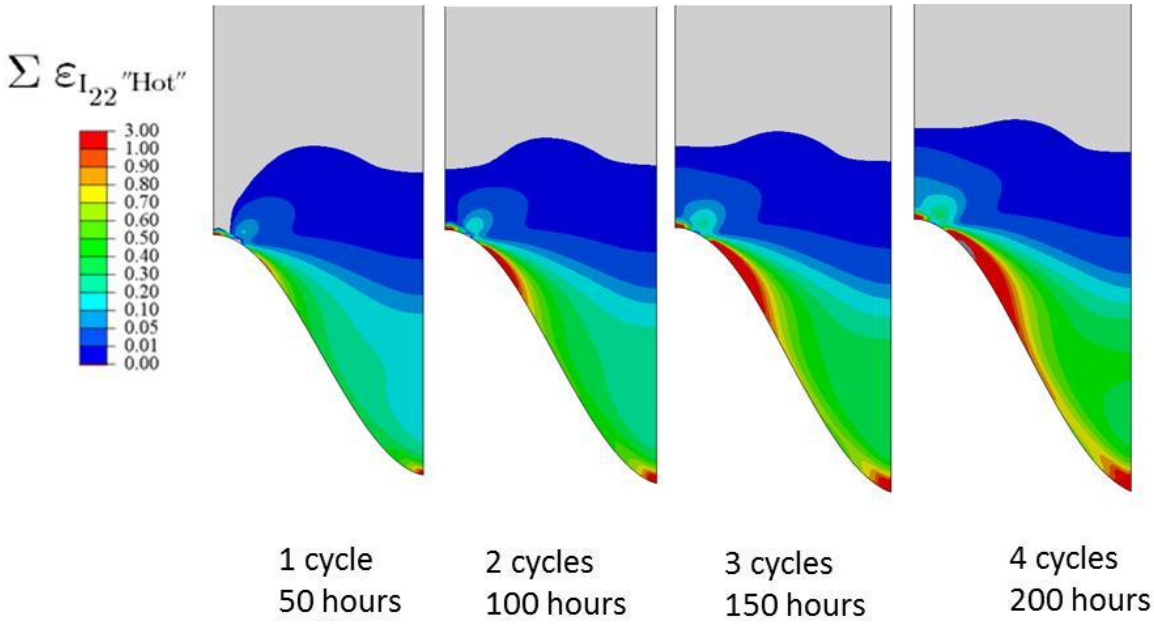

Figure 3.64 – High temperature inelastic strain contours (2000^{o}F, 50 hr cycles, YSZ viscoplastic)

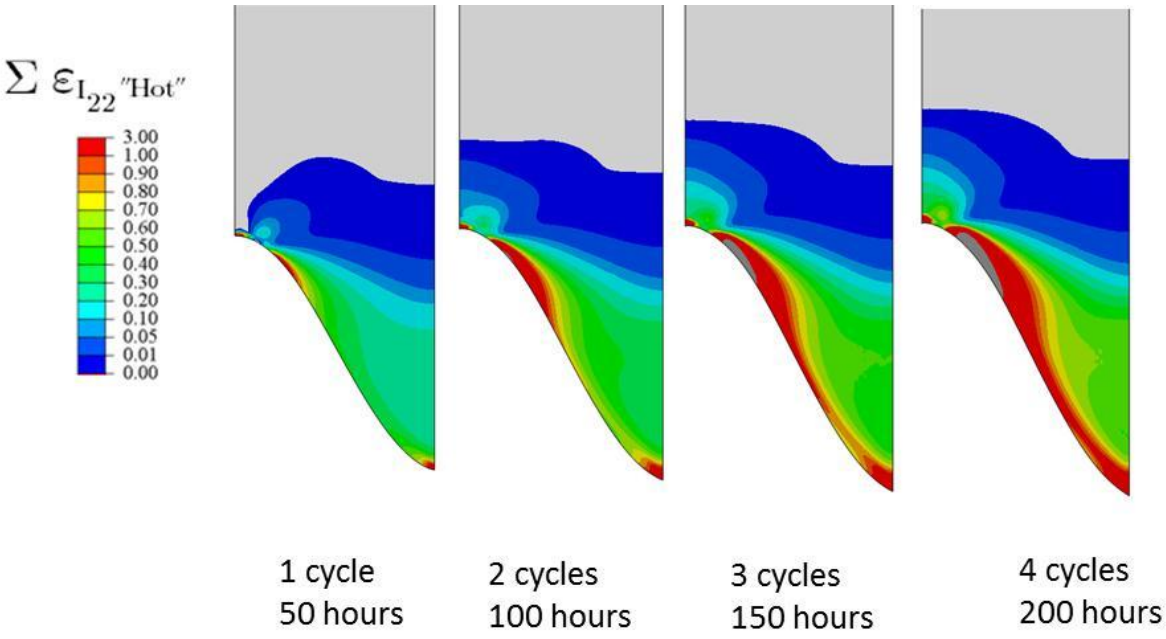

Figure 3.65 – High temperature inelastic strain contours (2050°F, 50 hr cycles, YSZ viscoplastic)

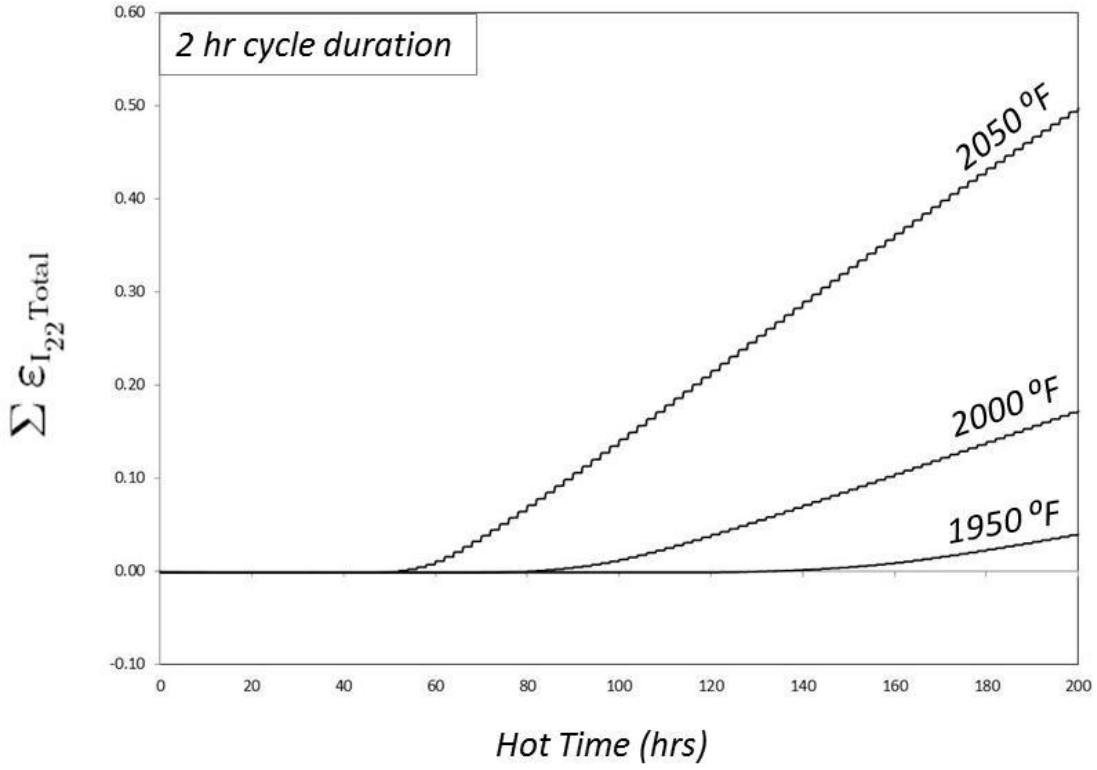

Figure 3.66 – Combined inelastic strain accumulation at location P (2 hour cycle duration)

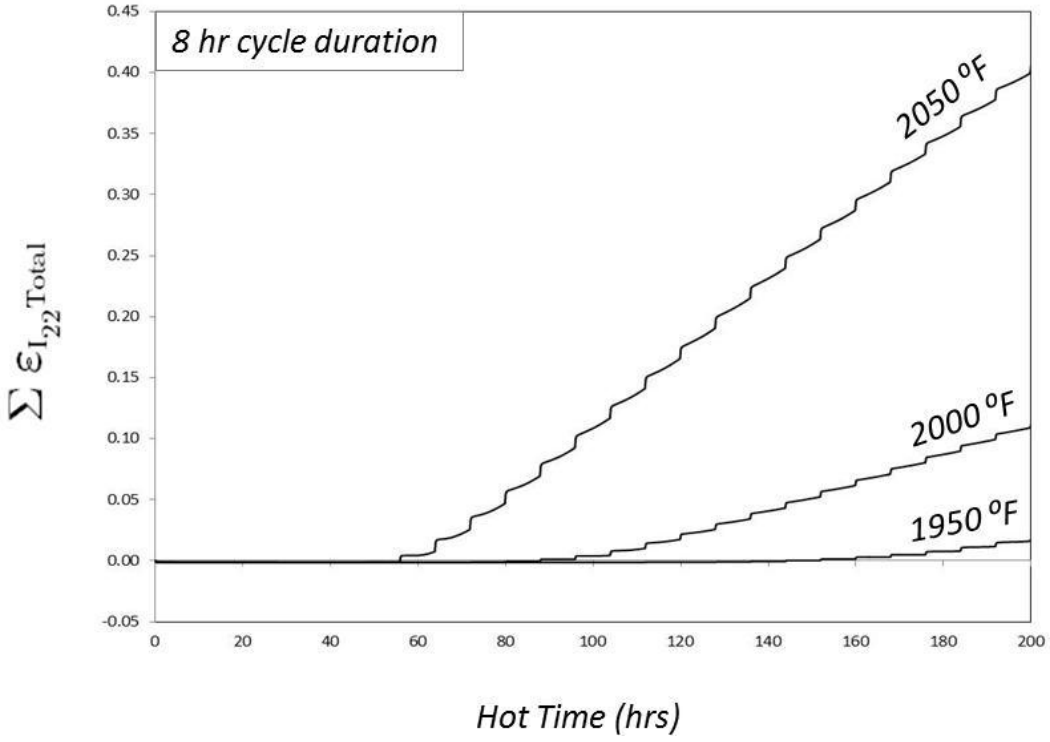

Figure 3.67 – Combined inelastic strain accumulation at location P (8 hour cycle duration)

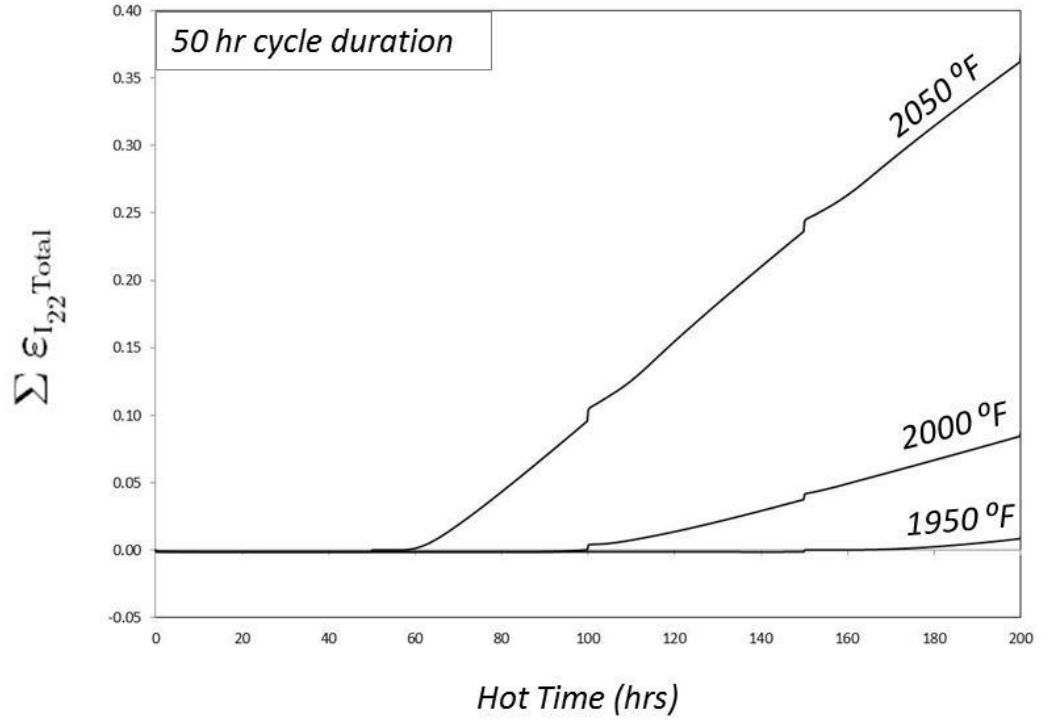

Figure 3.68 – Combined inelastic strain accumulation at location P (50 hour cycle duration)

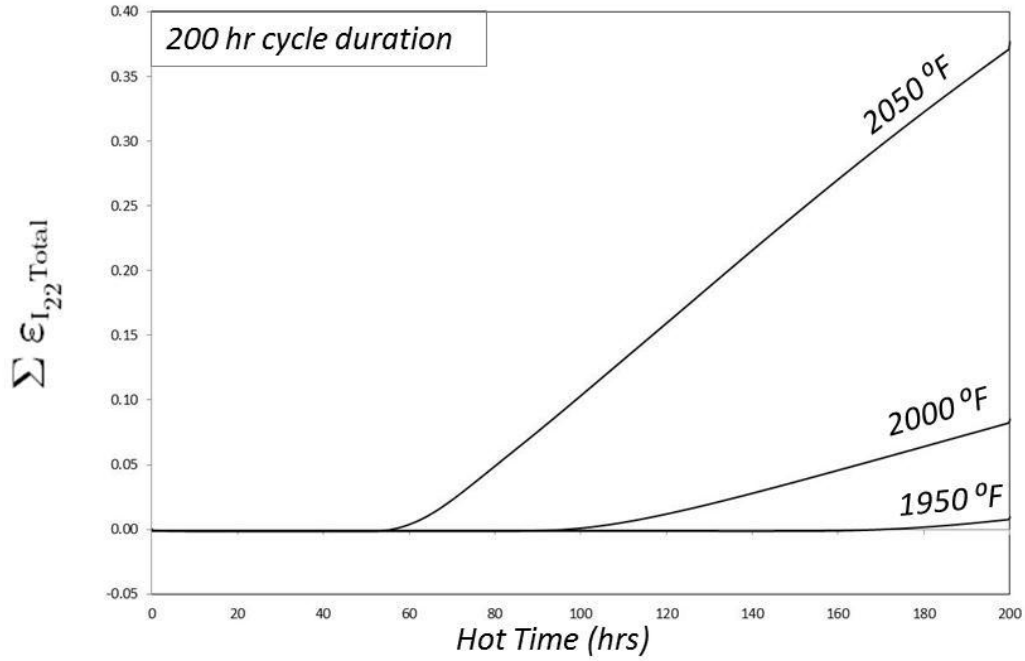

Figure 3.69 – Combined inelastic strain accumulation at location P (200 hour cycle duration)

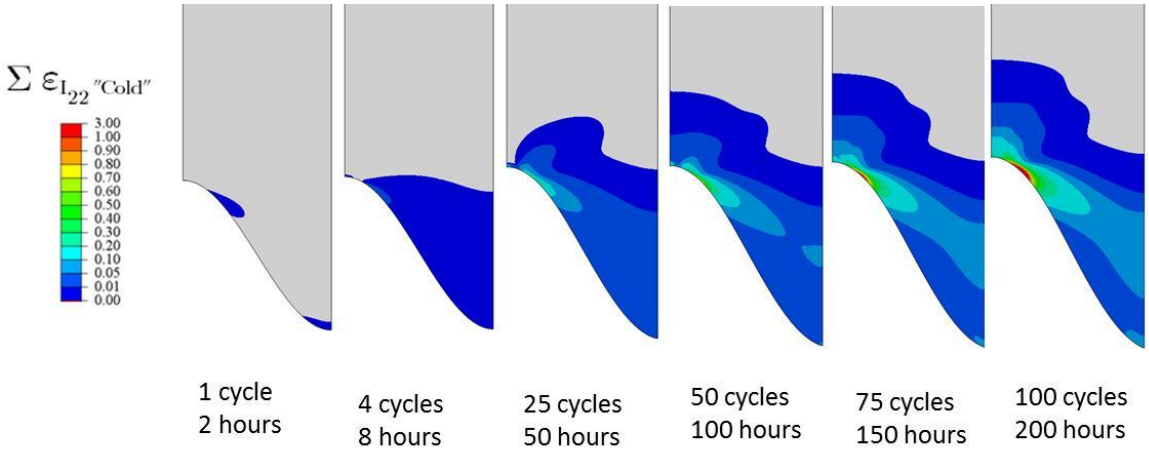

Figure 3.70 – Low temperature inelastic strain contours (2000°F, 2 hr cycles)

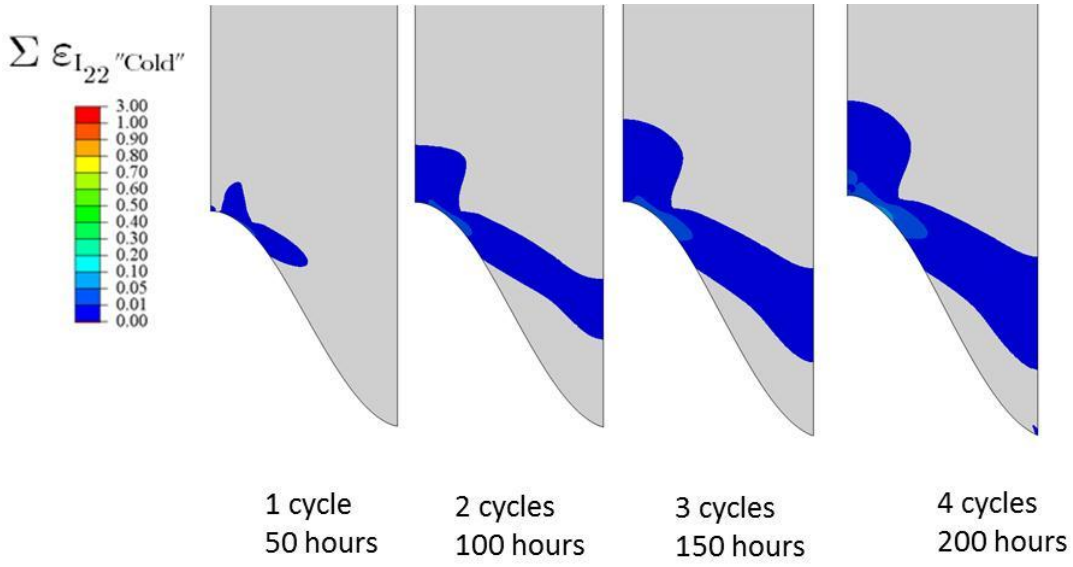

Figure 3.71 – Low temperature inelastic strain contours (2000^{o}F, 50 hr cycles)

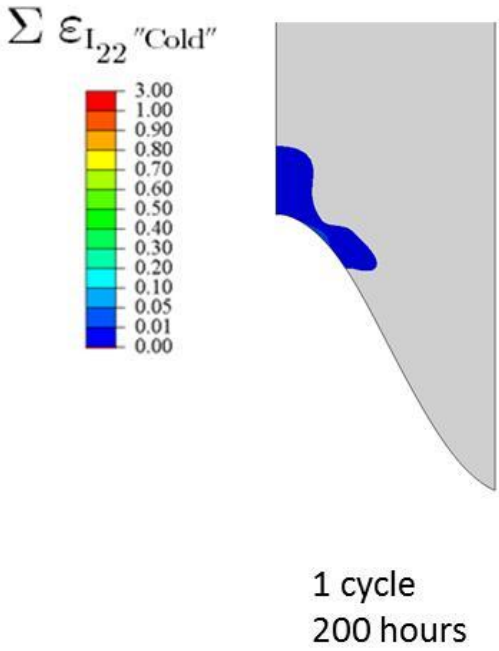

Figure 3.72 – Low temperature inelastic strain contours (2000^{o}F, 200 hr cycles)

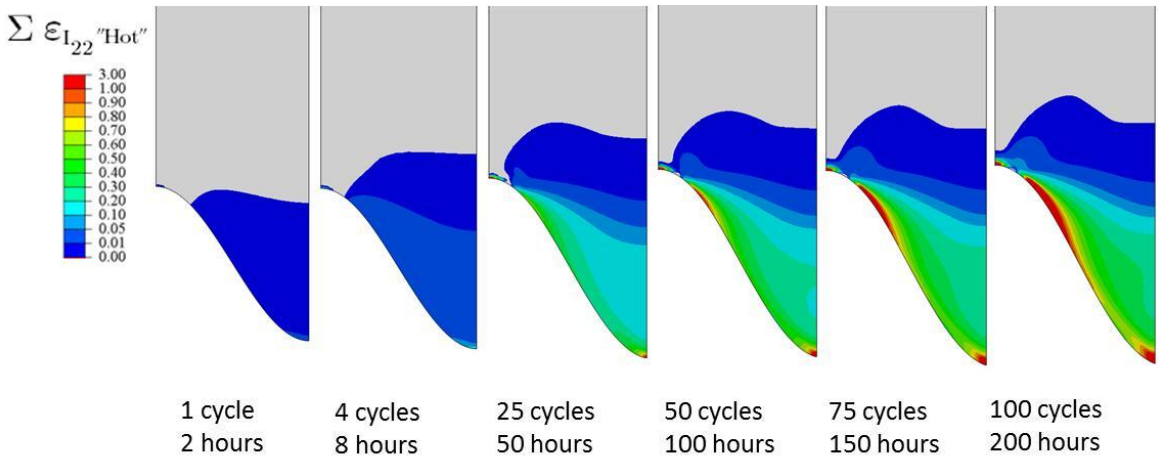

Figure 3.73 – High temperature inelastic strain contours (2000°F, 2 hr cycles)

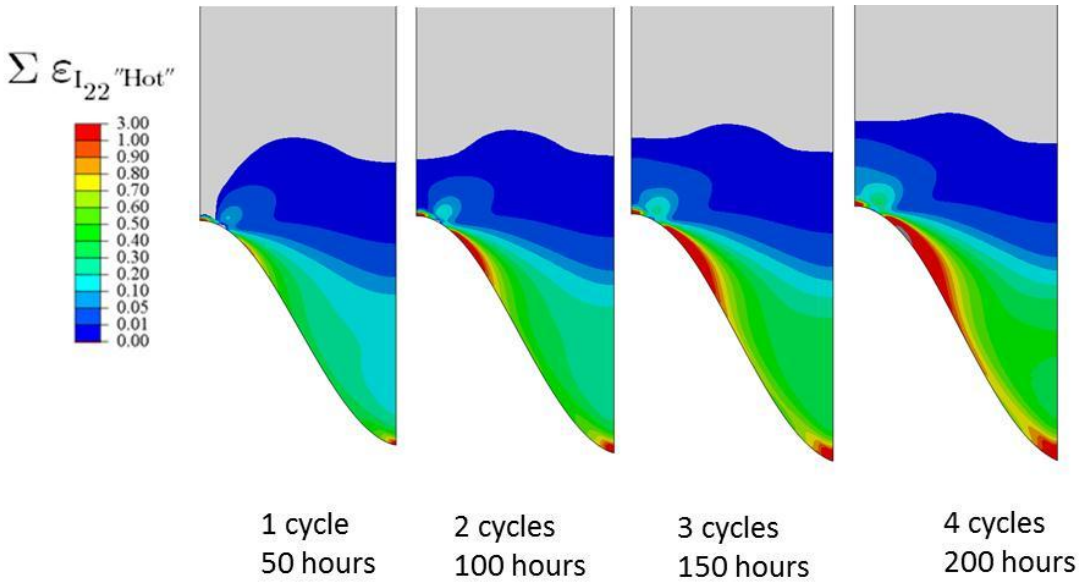

Figure 3.74 – High temperature inelastic strain contours (2000°F, 50 hr cycles)

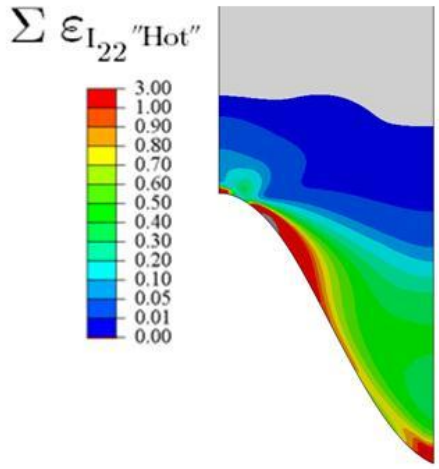

Figure 3.75 – High temperature inelastic strain contours (2000^{o}F, 200 hr cycles)

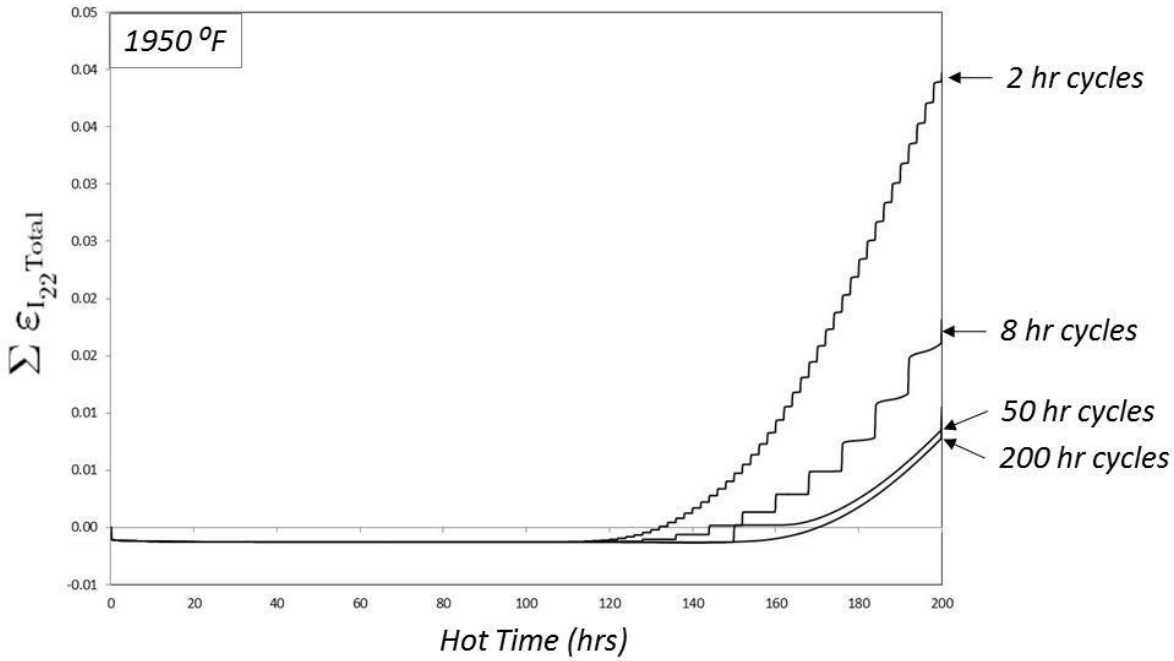

Figure 3.76 – Combined inelastic strain accumulation at location P (1950^{o}F)

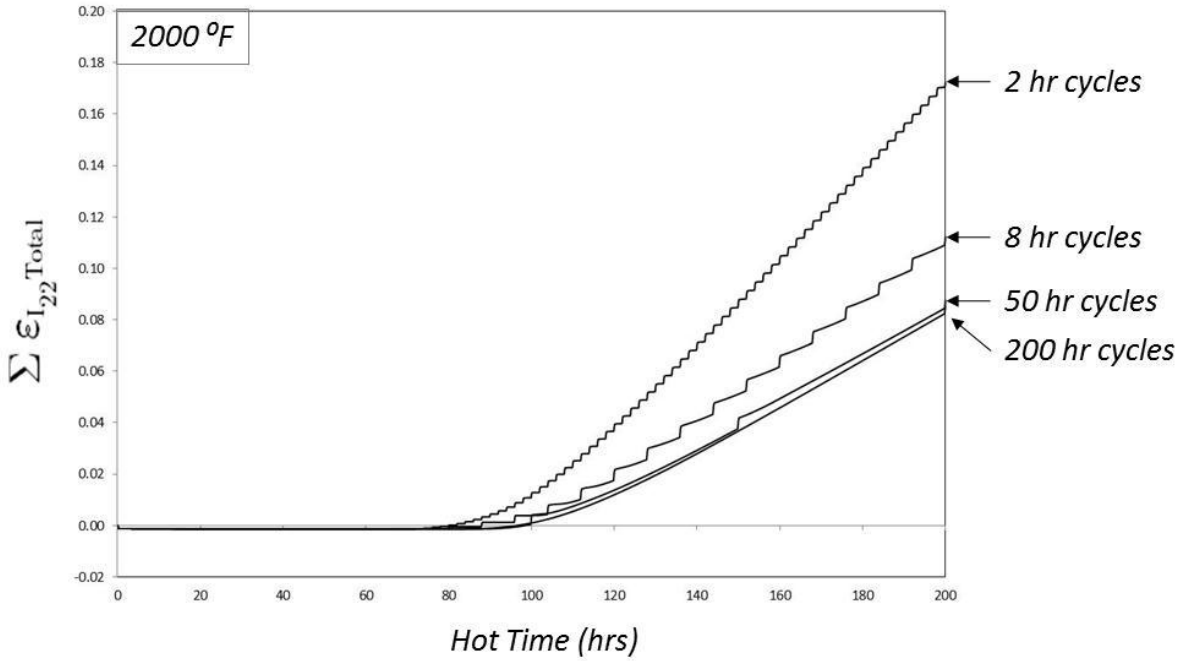

Figure 3.77 – Combined inelastic strain accumulation at location P (2000°F)

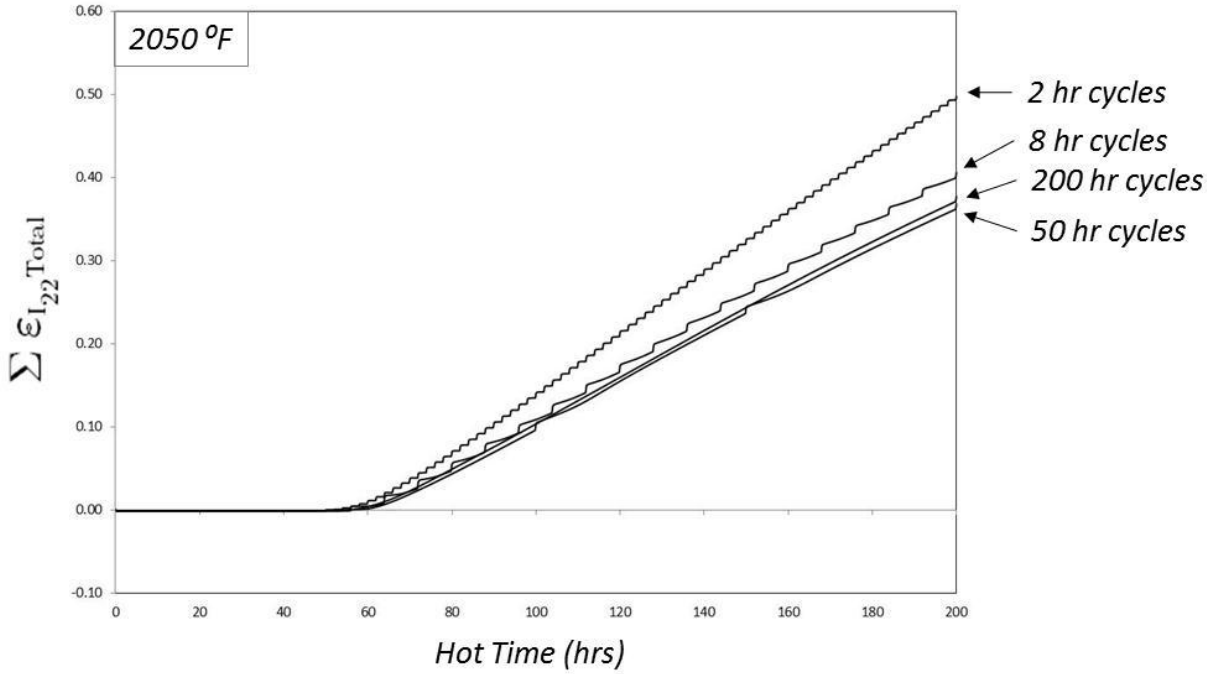

Figure 3.78 – Combined inelastic strain accumulation at location P (2050°F)

Table 3.1 – TGO thickness measurements

Temperature (°F)	Time (hours)	Average TGO Thickness (μm)
2100	0	0.355
	50	3.569
	100	4.186
	150	4.830
	200	5.119
2000	50	2.553
	100	3.060
	150	3.521
	200	4.019
	250	4.306
	300	4.429
	350	4.765
	400	5.063
	450	5.188
	500	5.409
	550	5.554
1900	50	2.197
	100	2.556
	150	2.674
	200	2.858
	250	3.088
	300	3.360
	400	3.993
	500	4.081
	600	4.282
	700	4.449
	800	4.666
	900	4.910
	1000	5.096
	1120	5.132
	1220	5.115
	1320	5.263
	1420	5.541
	1520	5.535

Table 3.2 – TGO growth parameters

Model Parameter	Value
Q	*206.273 KJ/mol*
K_{po}	2.15435×10^6 $\mu m^2/hr$
R	*8.314472 J/mol/K*
a	*0.0117*
b	*13.239*

Table 3.3 – Oxidation test failure lives

Hold Temperature (^oF)	Description	Failure upon cooling after
2100^oF	*primary test*	*200 hours*
	primary test/cut	*250 hours*
	confirmation test	*300 hours*
2000^oF	*primary test/cut*	*600 hours*
1900^oF	*primary test/cut*	*>2500 hours*

Table 3.4 – Summary of Finite Element Models

Description	YSZ Constitutive Model	TGO Constitutive Model
Thermal mismatch only	*Linear elastic*	*Linear elastic*
TGO growth	*Linear elastic*	*Linear elastic*
	Linear elastic	*Elastic/perfectly plastic*
	Viscoplastic	*Linear elastic*
	Viscoplastic	*Elastic/perfectly plastic*
Bond coat rumpling	*Linear elastic*	*Linear elastic*
	Viscoplastic	*Elastic/perfectly plastic*
TGO growth & bond coat rumpling	*Linear elastic*	*Linear elastic*
	Viscoplastic	*Linear elastic*
TGO growth & bond coat Al depletion	*Linear elastic*	*Linear elastic*
	Linear elastic	*Elastic/perfectly plastic*

4. Discussion

In the following sections, following the structure of the preceding sections, experimental results will be discussed first, followed by results from the modeling. Physical explanations will be given for the stresses obtained by finite element analysis, and the implications of inelastic strain output on life prediction will be shown. Furthermore, evidence from the experimental part will be given to support the modeling.

It should be mentioned that due to the implementation of the viscoplastic YSZ constitutive code, a previously unconsidered failure mechanism emerges that correlates well with experimental evidence and lends itself well to life prediction. This new approach of viewing thermal barrier coating failure will be elaborated on in the following sections.

4.1 Observed Failure Mechanism

4.1.1 Cause of Failure in Combustor Liner Panels

Micrographs of the combustor liner panels show clear signs of failure in the topcoat above the YSZ/TGO interface. In areas around the spallation zone where the coating remains attached, a region of increased crack density is seen which extends about 50 microns into the coating from the interface. As the spallation zone is approached, longer cracks are seen (as in Figure 3.7) until the main failure crack emerges and leads directly into the spallation zone. In the spallation zone, a thin layer of YSZ remains attached to the TGO, excepting regions where the crack runs directly

over, and sometimes into, the TGO, most commonly at asperity peaks, as shown in Figure 3.8. To draw an inference on the entire area of the spallation zone, thus making sure that a cross section which just happened to have YSZ attached was not chosen as a fluke, XRD was performed. A diffraction pattern was taken from the spalled region and compared to a pattern of the unspalled region as well as a cataloged pattern of YSZ. A comparison of the patterns, combined with the direct observation from the micrographs, leaves little doubt that the failure of the combustor liner panels, which saw actual in-service loading, took place in the YSZ.

4.1.2 Cause of Failure in Oxidation Test Samples

The cause of failure in the 2000^{o}F and 2100^{o}F oxidation test samples was similar to the combustor liner panels (the 1900^{o}F tests were suspended after 2400 hours). Because it was possible to make observations after every cycle while conducting the oxidation tests, progressive damage could be observed. Figures 4.1 and 4.2 show the state of the interface after increasing amounts of hot time for the 2000^{o}F and 2100^{o}F samples, respectively. The 2000^{o}F samples show the evolution of damage the best. The 300 hour micrograph shows an increase in cracks, but the opening displacements at the centers remain small and barely noticeable. At 400 hours, the cracks have noticeable openings, but they not coalesced. At 500 hours, it seems as if the cracks have coalesced into major cracks. The sample failed on cool down after 550 hours. The 2100^{o}F samples show a somewhat similar pattern, but accelerated. By 100 hours, cracks with large

openings at their centers are noticeable. By 200 hours, the long cracks that seem to precede failure are present, and upon cooling after 250 hours, the sample failed.

4.1.2.1 Residual Stress Calculated from Crack Openings

The residual stress in the coating was estimated from the opening displacements at the centers of the two cracks shown in Figure 3.22, as explained in section 3.1.3.2.1. The stresses obtained were 529 MPa and 439 MPa for the two cracks. The stress in this case is the far field stress, which can be interpreted as the uniform pressure load that would have to be applied to the crack faces to result in the measured displacements. The purpose of the calculations is to give further evidence that the YSZ cannot be linear elastic and still produce these large crack openings.

The method used assumes the crack is a "penny-crack" in an infinite, homogenous, linear elastic domain [38]. The cracks in Figure 3.22 are not exactly penny shaped, and the domain is certainly not infinite and homogenous, but these assumptions approximate the true geometry somewhat, and the purpose here is to gain insight into the general magnitude of the residual stress in the coating if it were linear elastic, not the exact value. The ultimate tensile stress at room temperature of various YSZ specimens measured by DeMasi et. al. range from about 20 to 50 MPa, as seen in Figure 2.13. This is approximately one order of magnitude lower than the stresses predicted by the linear elastic crack opening displacement equation. This leads to the conclusion that the high stresses predicted under the assumption that the coating is linear elastic could not exist without doing extensive damage to the surrounding coating; rather, there must be a significant non-linear component to the stress-strain response of the YSZ that allows for these large observed crack opening displacements. The viscoplastic constitutive

model used in some simulations in this thesis has a flow stress in tension of about 39 MPa, which is more in line with the experimentally measured values.

4.1.2 Cause of Failure in Burner Rig Samples

By establishing a thermal gradient through the thickness of the TBC, a burner rig test is designed to simulate more closely the actual loading conditions of the engine. A failed pin-type burner rig specimen was supplied for inspection to compliment the observations made on the combustor liner panels and the oxidation test samples. The sample was cross-sectioned and micrographs were taken using the FESEM. From the micrographs in Figure 3.23, it is concluded that the region of heavy damage was due to heating after the coating had already spalled, as the layer of TGO on the substrate indicates, and does not infer anything about the initial failure of the coating. The region around the heavy damage, however, appears to have a similar damage profile to the combustor panels and the oxidation samples. Figure 3.24 is a cross-sectional micrograph at the edge of this spallation region, where the full thickness of the YSZ remains, which shows that the major failure crack runs in the YSZ just above the interface. From the EDX mapping shown in figure 3.25, it is clear that the surface of the spallation zone is predominantly covered with YSZ, further confirming the assertion that the burner rig sample failed due to cracking just above the interface in the YSZ like the combustor panels and the oxidation test samples.

4.1.3 Summary of Failure Mechanism Observations

The observation that the failure of the coatings was independent of loading type is significant because it led to the decision that a simple uniform temperature profile would be sufficient for modeling the heating and cooling of the system. Implementing a temperature gradient approach would have required using coupled temperature-displacement elements in all layers, roughly doubling the size of the model.

All three types of samples failed in the same location – in the YSZ just above the YSZ/TGO interface. This is consistent with the imperfection/bond coat geometry induced failure, commonly observed for APS YSZ coatings and outlined in section 1.2.1. The most relevant quantity to failure in this theory is the out-of-plane stress above the interface resulting from strain from either thermal mismatch or oxide growth. Studies have shown that the resulting out-of-plane stress state in the YSZ above a growing oxide is, generally: tension in the valleys and compression above the peaks of bond coat asperities [15,16]. This stress state would lead someone taking a damage based view of failure (as opposed to a fracture mechanics based view) to conclude that there could never be any damage above the peak since the YSZ is in a state of constant compression. Experimental evidence, however, like the micrograph shown in Figure 4.3, shows that cracks can be extended over peaks. Since the stresses resulting from models that consider the YSZ to be linearly elastic don't provide a suitable explanation for the observed damage patterns and are usually unreasonably high, modeling which incorporates the realistic material behavior of the YSZ was performed with the hope that it would yield more realistic stresses consistent with the observed damage. The

way in which the nonlinear YSZ accommodates the strain due to thermal expansion and oxide growth was of particular interest. It was hoped that in nonlinear finite element modeling, a stress state would emerge that provided a sufficient explanation for failure and that outputs would be obtained that were suitable for a life prediction model.

4.2 Results of the Finite Element Models

4.2.1 Models with a Linear Elastic YSZ

Before going on to model the nonlinearities of the YSZ, it was considered important to show that the model could reproduce results previously obtained in the literature for a linearly elastic YSZ. Modeling the YSZ as linear elastic also allowed us to judge the relative importance of the morphological phenomena observed in our experimental observations (TGO growth, rumpling, and bond coat Al depletion) before we attempted to input these effects into the more computationally costly nonlinear models.

4.2.1.1 Stresses due to Thermal Mismatch

Many of the early attempts to describe the stress above the undulating YSZ/TGO interface was based on thermal mismatch alone. The TGO was simply taken to be different thicknesses, rather than grown continuously, with a corresponding decrease in thickness of the bond coat or YSZ [11-14]. In other words, the strain imposed on the material surrounding the TGO due to its growth was not considered. The results shown in Figure 3.27 are consistent with the results in the literature. When the coating is at

high temperature and the TGO is at a sufficiently small enough thickness so that the effective thermal expansion coefficient of the bond coat/TGO is greater than that of the YSZ, the material above the peak is in compression (out-of-plane) and the material in the valley is in tension. When the system cools, the peak is put in tension and the valley compression. The bond coat thickness below the peak is greater than the thickness below the valley, so upon cooling to room temperature, it will attempt to shrink more, which pulls the YSZ above the peak and squeezes it in the valley. When the TGO thickness becomes sufficiently large enough so that the effective bond coat/TGO thermal expansion coefficient is less than that of the YSZ, the reverse happens. Since the YSZ now wants to expand more than the bond coat/TGO, the YSZ above the peak is in tension at high temperature and the YSZ in the valley is in compression, and upon cool down, the material above the peak goes into compression and the material above the valley into tension. The exact TGO thickness at which the stresses switch sign is dependent on material properties, interface geometry, and according to Figure 3.27, distance from the interface, so it is not expected that our results would match up precisely with the other studies, but they are close and follow the same trend.

The stresses from these models are not thought to be accurate, since the continuous growth of the TGO as well as bond coat rumpling and nonlinear material properties have such a dominating effect, as have been shown and will be discussed. The value in these models lies in the intuition gained by determining how generic layered materials with the current geometry configuration behave when subject to thermal misfit. Another important result is the general magnitude of the stresses, which

shows that the model is capable of producing relatively low stress levels, in comparison to the unrealistically high stresses output when TGO growth and rumpling are considered.

4.2.1.2 Stresses due to TGO Growth

TGO growth was modeled by the procedure described in section 2.5.3. When the TGO reaches 4 microns, the stress at cool down at location P is about 4 GPa in compression, as shown in Figure 3.29. When this is compared to the 6 MPa in tension obtained for the 'thermal mismatch only' case, it becomes clear that since the results are not remotely similar, the effect of TGO growth must simply be dominating the effect of thermal mismatch. The reason for this stress state is very intuitive. Since the elastic modulus of the YSZ is lower than the modulus of the bond coat, most of the TGO growth is accommodated by shape change of the YSZ. The YSZ above the peak is being compressed and the YSZ in the valley is being stretched by the effective amplitude change due to the uniformly growing oxide.

The stresses predicted by imposing this shape change are much too large for the YSZ to stand, and if they were accurate, the coating would fail after about the first cycle. It is clear that the stresses must be rearranged by material nonlinearities in the YSZ, TGO, and bond coat.

4.2.1.3 Stresses due to Rumpling

Bond coat rumpling was modeled by the procedure described in section 2.5.4. The tortuosity after 200 hours of hot time, measured from sequential micrographs at 2000F, was used to calculate the required amplitude change that would lead to this tortuosity. In these models, rumpling was simplified to mean amplitude change based on tortuosity measurements. The amplitude was grown proportionally to the TGO thickness. Figures 3.31 and 3.32 and Figures 3.33 and 3.34 show the stresses resulting from the rumpling without and with TGO growth, respectively. The stresses in Figures 3.33 and 3.34 are simply the sum of the stresses due to rumpling only and due to TGO growth only, since everything is elastic. For example, at location P, the compressive out-of-plane stress upon cool down after 200 hours of hot time is: 5.04 GPa for rumpling only, 3.95 GPa for TGO growth only, and 8.77 GPa for a combination of rumpling and TGO growth. The amplitude change is 10 microns for rumpling only, while the TGO thickness change is 3 microns for TGO growth only. This means that the rate of stress increase above the peak with respect to TGO thickness is -1.68 GPa/micron for amplitude change only and -1.317 GPa/micron for TGO growth only. So it is seen that for this case the amplitude change associated with the thickening TGO causes more stress per unit thickness than the TGO growth itself.

Although these results give some evidence towards it, the validity of the general statement that rumpling due to TGO growth is more damaging than the TGO growth itself should be questioned for three reasons. First, the amplitude change when calculated from tortuosity data is dependent on the wavelength. Given a change in

tortuosity, the change in amplitude will be smaller for longer wavelengths than for shorter ones, which means that the question as to which causes more damage, TGO growth or rumpling, will be tipped in favor of TGO growth for longer amplitudes. However, it should be said that the sinusoid used in the current model (25 micron amplitude and 100 micron wavelength) represents commonly observed geometries. It would be interesting to see at what wavelength the stresses due to TGO growth outweigh the stresses due to amplitude change. Second, this modeling was done in the context of a linear elastic YSZ. It has already been seen that the stresses resulting from a nonlinear YSZ are drastically different. Third, and most important, it was assumed, largely for model simplicity, that rumpling is manifested solely by amplitude change. This may be the case, but intuition and experience from looking at micrographs of increasingly exposed coatings indicates that it's not. Admittedly, doubling the amplitude, which was done in the current case, seems a little improbable. It is difficult to tell exactly how rumpling manifests itself because it is difficult, if not currently impossible, to observe the same cross section through periods of repeated thermal cycling. Rumpling may be manifested through a combination of amplitude and wavelength change, but since the actual interface shape is obviously far from a periodic sinusoidal curve, it is probably far more complex. It seems that accurate measurements of the interface shape after each loading cycle need to precede the modeling to identify the exact manner of the shape change.

4.2.1.4 Stresses due to TGO Plasticity

In this model, the TGO was assumed to be perfectly plastic at high temperature. This was accomplished by giving the TGO a yield strength of 1 GPa above 2000F (or the hold temperature) and a yield strength of 10 GPa below 1900F, as outlined in section 3.2.2.1.5. This ensured that the TGO was purely plastic while it was growing, but elastic upon cool down. TGO plasticity was incorporated because it was observed that the very large compression the TGO sees cannot realistically be absorbed by its elasticity. So it was decided to let the TGO flow freely at high temperature, representing the extreme bound of TGO plasticity, and observe how the stresses in the YSZ would be affected.

Figure 4.5 shows S_{22} and S_{11} in the middle of the TGO for the elastic case along the path shown in Figure 4.4. The areas of highest stress are consequently the areas of the highest plastic strain, shown in Figure 4.6, when plasticity is introduced. The distribution of plastic strain has the effect of making the TGO, seen in Figure 4.7, bulge in the middle (approximately midspan). This in turn leads to the YSZ in the valley being squeezed horizontally. When the TGO is elastic and grows uniformly, the YSZ is squeezed horizontally, too, but the material above the peak is simultaneously being lifted, resulting in compression above the peak and tension in the valley. When the TGO is plastic, the extra horizontal plastic strain causes the YSZ to be squeezed at a rate higher than it is being lifted. When the squeezing effect wins out, tension is developed above the peak. The reason why this tension develops can most easily be seen by plotting the vertical displacements on a path drawn above the peak and across the width of the interface relative to the displacement of a point above the peak, as shown

in Figure 4.8 for the elastic case and Figure 4.9 for the plastic case. The elastic displacements show that material above the valley becomes depressed relative to the displacement above the peak, which leads to compression above the peak. The displacements when the TGO is plastic show that the material above the valley becomes raised relative to the material above the peak, leading to tension over the peak. Most of the displacement in both cases occurs early on in the history, when the TGO grows the fastest. A cartoon showing the basic idea of the stress redistribution due to TGO yielding is shown in Figure 4.10.

The TGO probably doesn't behave as a perfectly plastic material. The micrographs show uniform oxide growth, rather than the "bulged" shape predicted by the model. In the model, the TGO thickness at the inflection point of the sine curve is 5.17 microns, which is almost 30% more than the thickness due to growth (4.03 microns). This would definitely be observable in the micrographs. Nonetheless, the perfectly plastic TGO model is an extreme case (the other extreme being the perfectly elastic TGO case) which is helpful as it gives an upper bound to the stress state which would result given the true nature of its plasticity. For the most accurate stresses to be obtained, a viscoplastic model similar to the one used for the YSZ would probably need to be implemented.

4.2.1.5 Stresses due to Al Depletion from Bond Coat

Bond coat aluminum depletion was modeled by the procedure described in section 2.5.5. It was already mentioned that, when the layers are elastic, most of the

shape change due to TGO growth has to be accommodated by the YSZ because its elastic modulus is quite a bit lower than the bond coat's, largely because of the YSZ's microstructural strain tolerance. But since the bond coat transforms from β-NiAl to γ'-Ni_3Al as the aluminum which creates the TGO is depleted, the bond coat shrinks a little, as detailed in section 2.5.5. So the imposed shape change on the YSZ is somewhat tempered by the effect of the shrinking bond coat. The amount that the bond coat shrinks is determined by the location from which the aluminum to create the TGO diffuses. As was suggested previously, two extreme cases can be imagined, the first being when the aluminum comes entirely from deep in the bond coat. This would be the 'TGO growth only' case. The second is when the aluminum comes entirely from under the asperity, which is the case modeled here. Figure 3.37 showed a comparison of the stresses resulting from both cases when the TGO is elastic. It is clear that the shrinking bond coat has an effect similar to reducing the TGO growth rate, differing slightly because the bond coat shrinks isotropically while the TGO grows only normal to the interface. The result of this difference is that the stresses just above the valley are reduced a little more than the stresses above the peak. When the TGO is plastic, the stresses above the peak become more tensile, while the stresses above the valley become quite a bit less tensile, as shown in Figure 3.43. It was explained in the previous section how the plastic TGO manages to put the YSZ above the peak into tension by squeezing the YSZ in the valley, leading to higher displacements above the valley relative to the peak. When the bond coat shrinks in addition to this, the situation is

exacerbated, as the thickest vertical section of bond coat (underneath the peak) pulls on the material above the peak, leading to greater relative displacements than before.

Since the stress trends don't differ too much from the TGO growth only case, especially when the TGO is elastic), and since it is fairly intuitive that the effect of bond coat shrinkage is similar to that of reducing the TGO growth rate, it was not pursued in any of the more detailed models.

4.2.2 Models with a Viscoplastic YSZ

4.2.2.1 Stresses due to TGO Growth

This is the same model as discussed in section 4.2.1.2, except the YSZ was modeled using the viscoplastic constitutive code described in section 2.5.6. Again, the motivation behind using the viscoplastic model was the unreasonably high stress results from the linear elastic model. Nonlinear material behavior was focused on the YSZ rather than the TGO or bond coat because, as was seen in Figure 3.40, the stresses in the YSZ increased into the unrealistic GPa range even when perfect TGO plasticity was included. It was inferred that the same would happen for a plastic bond coat. Also, since the stresses in the YSZ have the greatest implications on failure (which occurs in the YSZ) it made sense to model them as realistically as possible.

From Figure 3.44 it was seen that the out-of-plane stress over the peak initially dips into compression but then goes into tension as time progresses, while the stress above the valley dips into compression and stays there. The mechanism causing this stress state can be identified by plotting the displacements above the peak and across

the width of the coating relative to the displacement above the peak, as was done to analyze the stresses due to TGO plasticity. Figure 4.11 shows both the out-of-plane stress at location P and the displacements (relative to location P) along the indicated path at certain times. Initially, the YSZ trends toward the stress state it would assume if it were linear elastic, with compression above the peak and tension in the valley. It doesn't take long, however, before the YSZ in the valley reaches its tensile flow stress. When the stress reaches the flow surface, the YSZ continues to incur increased in-plane compression due to the horizontal component of TGO growth, which simultaneously moves the stress-state counterclockwise along the perimeter of the surface. Eventually the YSZ becomes compressive in the out-of-plane direction. The idea is depicted in Figure 4.12. Because the in-plane thickness of the YSZ is the lowest at the bottom of the valley, the in-plane compressive stress due to the TGO growth is greatest, so this is the area that switches over to out-of-plane compression the fastest, although the entire valley switches over relatively quickly. This process can be seen in the stress contour plots of Figure 3.46.

In summary, the stresses in the YSZ initially trend toward the elastic stress state, but upon yielding in tension, the horizontal component of TGO growth causes the YSZ in the valley to slowly flow upward while remaining in compression. The eventual result of the upward material flow is to displace the material well-above the valley, which puts the material above the peak into tension. A cartoon of the process is shown as Figure 4.13. This process can be viewed as a sort of high temperature extrusion process, where the TGO acts to extrude the highly stressed material in the valley upward, putting

pressure on the rest of the top coat, which still has sufficient stiffness to put the material above the peak into tension.

One direct result of this is that a region of out-of-plane tensile stress originates in the valley and eventually migrates over the peak, eventually traversing the entire width of the coating and providing a theoretically complete pathway for cracks, which was not seen in any of the linear elastic models.

4.2.2.2 Stresses due to TGO Plasticity

The explanation for the stresses seen in Figure 3.49 is essentially a combination of the explanations for the cases of TGO growth with a viscoplastic YSZ (previous section) and TGO growth with TGO plasticity and a linear elastic YSZ (section 4.2.1.4). For the plastic TGO/linear YSZ case, the tension above the peak was due to the extra vertical displacements of the valley material, which was squeezed by the horizontal bulging of the yielded TGO. In the presence of the viscoplastic YSZ, this bulging serves to increase the rate at which the material flows upwards from the valley, greatly accelerating the process of putting the material above the peak into tension. The contours in Figure 3.51 show that the process is nearly complete even after one 4 hour cycle at 2000F, as opposed to about twenty five 4 hour cycles for the case with no plasticity. Again, the perfectly plastic TGO is an extreme case. A more realistic plasticity law would put the conversion as taking between 4 and 100 hours to complete.

The most important result of this model is that the only major effect the TGO plasticity has on the stress trends when the YSZ is viscoplastic is to shift the amount of

time taken to move the tensile region to over the peak. This is in contrast to when TGO plasticity was implemented in the linear model, where the stress trends were significantly different. Because the effect of TGO plasticity has been sufficiently explored, it will not be pursued in any of the more detailed models. It is expected, however, that in order to capture accurate stresses in the early stages of TGO growth, a realistic TGO constitutive law would be needed.

4.2.2.3 Stresses due to Rumpling

The stresses that result from bond coat rumpling are explained in a similar way as the TGO growth stresses. For the present model, it was assumed that bond coat rumpling was manifested entirely through an amplitude change. In other words, the thermal strains applied to the bond coat elements to simulate rumpling were entirely vertical with no horizontal component. As opposed to the TGO growth only case, and as seen in Figures 3.47 and 3.48 showing the out-of-plane stress evolution for the rumpling cases with and without TGO growth, the stresses above the peak are compressive the entire time, while the material in the valley remains in tension. Initially, the material in the valley closely resembles the stress state described in the TGO growth only case, quickly reaching its flow stress in tension. This time, however, instead of turning compressive, the material remains in tension because there is no horizontal component of TGO growth or rumpling to move the stress state along the flow surface. The material stills flows upward, but this time it just flows with the stretching caused by the amplitude change. It does not demonstrate the “extrusion effect” caused by in-plane

compression. When TGO growth is added in addition to the amplitude change, the changes are subtle. The stress magnitudes increase a little because the rate of growth increases. The TGO growth never has a chance to put the material above the peak in tension because the stretching due to amplitude change simply dominates any extra upward flow from the growing TGO.

The results of this case highlight the importance of accurately measuring the shape change caused by rumpling. In this simplistic model, rumpling was simply taken to mean amplitude change, which resulted in a stress field where the material above the peak was in constant compression and the valley in constant tension. If rumpling was taken to mean wavelength change, the stress field would be similar to a model with only horizontal TGO growth, which would very quickly put the material above the peak in tension and the valley in compression. So this case just serves as evidence that the way in which rumpling is modeled can have drastic effects on the stresses in the YSZ, and highlights the importance of making detailed measurements.

4.3 Time/Temperature Effects on Stress

The TGO growth only model was used in the more detailed analyses because it was considered to be the most relevant case to the development of stresses that lead to failure. Rumpling may play a larger role than TGO growth, but since the shape change due to rumpling is not well known, and the stress state is so sensitive to the shape change of the TGO/bond coat, it was not included.

Figure 3.52 showed the stress evolution above the peak for 50 hour cycle durations at different temperatures. Figure 3.54 showed these stresses plotted against TGO thickness. The fact that the stresses become very similar when plotted against TGO thickness gives good evidence that the stresses are more affected by the increase in TGO growth rate due to an increase in temperature than by any increase in thermal expansion or change in material behavior.

Figures 3.55 and 3.56 show the out-of-plane stresses in models run with 2 hour cycle durations and 200 hour cycle durations for locations P and V and locations AP and AV, respectively. Both models were run for 200 hours of hot-time. From these plots, it is evident that the stresses from the shorter cycles progressively lag the stresses from the longer cycles and the amount of lag is greater for the locations further into the coating. Figure 3.57, which shows the stress at location AP as a function of cycle duration, and Figure 3.58, which shows path plots of stress above the peak for different cycle durations, gives a more complete picture. A reason for this lag is potentially explained by examining a plot of out-of-plane stress at location A at 2000F for an intermediate length cycle; 20 hours for example, as seen in Figure 4.14.

For any given cycle before about 80 hours, the YSZ is in compression at high temperature and more compression upon cool down. Upon heating back up again, the alleviation of the accumulated back stress (a feature of the viscoplastic model) allows the YSZ to go into a less compressive state than it was previously in. The growing TGO then causes an increase in compression, and at some point the equilibrium is struck again between increasing compression from the TGO growth and the increasing tension

arising from the material flowing up in the valley. When the stress gets to be in overall tension (after about 80 hours in this case), the effect is reversed. Upon cooling the stress becomes more tensile and upon heating, the back stress causes it to be less tensile than it was previously. The material then proceeds to adjust itself to this "equilibrium" position.

So if the system cools down again before it's allowed to reach this "equilibrium" stress, it will progressively ratchet itself away, causing the observed lag. The reason that the effect is magnified a small distance away from the interface is because the stresses due to the TGO growth are not as prevalent there, so the return up to the equilibrium stress is slower. The effect diminishes again as the distance increases further, but this is just because the magnitude of the out-of-plane stresses at these far distances is very small.

4.4 Inelastic Strain

The inelastic strain output of the viscoplastic YSZ constitutive code is a better indicator of the amount of damage incurred on the model than stress. As described in section 3.2.3.2, low temperature inelastic strain is interpreted as localized failure, or microcracking, and high temperature inelastic strain is interpreted as material flow, possibly with a component of microcracking also.

Most of the high temperature tensile inelastic strain starts accumulating in the valley early on in the history, as was seen in the contour plots of Figures 3.62-3.64. The high temperature inelastic strain begins accumulating over the peak later on. The

opposite trend is seen with the low temperature inelastic strain (Figures 3.59-3.61). The contour plots show that the off-peak regions are the areas of the coating which see the highest accumulations of low temperature tensile inelastic strain, consistently throughout the entire history. The next highest region of inelastic strain lies in a band which dips from the off-peak region and crosses the valley at approximately half the peak-to-valley height. The area just above the peak seems to be the last region to go. It follows that the region with the highest probability of damage or cracking is the off-peak-region, followed by the valley, and finally the peak. Some of the micrographs of damaged oxidation test samples seem to support this (Figures 4.15-4.22).

4.5 Implications of Inelastic Strain on Life Prediction Methods

The accumulation of inelastic strain is dependent on temperature, overall time at temperature, and cycle duration, which makes it an attractive candidate for use in a life model since these are the major loading parameters which have been observed to affect failure in thermal barrier coatings. Figures 3.66-3.68 show the total (high temperature and low temperature) inelastic strain for varying temperatures and constant cycle durations at location P. Figures 3.75-3.77 show it for constant temperature and varying cycle duration. The high temperature and low temperature inelastic strain are easily distinguishable by eye, the low temperature strain being the vertical increments. Figure 4.23 shows the total inelastic strain plotted against the out-of-plane stress at location P, from which it becomes clear the manner in which it accumulates.

The point above the peak was chosen as the place where the inelastic strain is the most relevant to failure because it is the slowest to accumulate it of the three major regions that experience intense inelastic strain (off-peak, valley, and above peak, as discussed in section 4.4). So the material above the peaks might be thought of as the bottleneck to the process of extending a zone of damage throughout the coating. It makes sense then that as the inelastic strain accumulation at this point increases, so does the probability that there exists a zone extending across the peaks that has an increasingly sufficient amount of damage to cause failure. This zone of damage eventually coalesces to become part of the main failure crack that subsequently causes the coating to buckle. If some combination of high temperature and low temperature inelastic strain in the YSZ could be correlated to measured failure lives, the lives of coatings could be predicted based on the temperature and cycle histories. The finite element model, which was the physical basis used to derive the inelastic strain curves, could be used to assess the coating life sensitivities to model inputs such as material properties and geometries.

Although the highest dependence of inelastic strain is on temperature, the strong dependence that it shows on cycle duration is promising. The common observation that coating life decreases as cycle duration decreases has traditionally been one of the tougher features to work into life prediction models which attempt to describe the failure physically. To correlate life to inelastic strain, a program is needed in which the lives of coatings having various temperature and cycle duration histories are measured. To compliment this, now that the major stress trends and their causes have been

identified, models need to be run using bond coat and TGO material properties that more closely represent their true behavior in order to get the most accurate numerical results for the correlation.

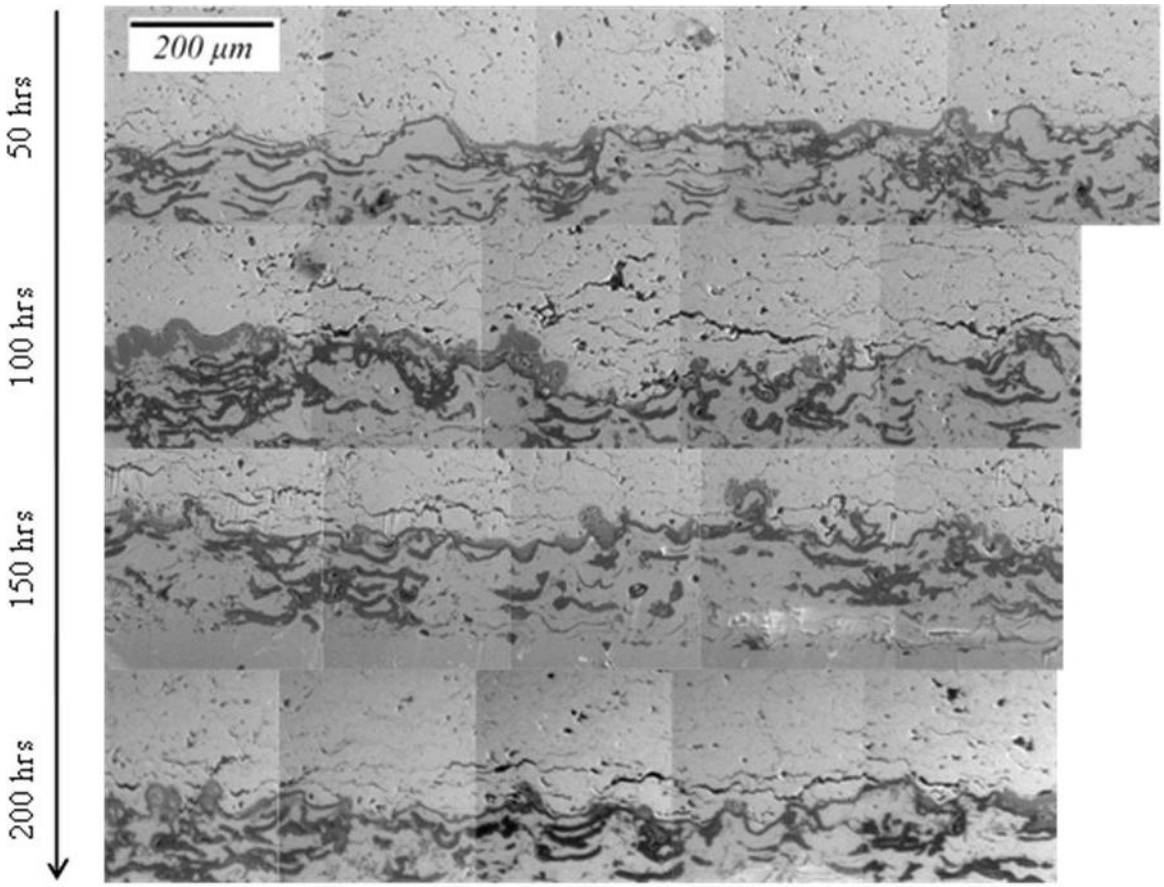

Figure 4.1 – Evolution of the interface for loading at 2100^{o}F with 50 hour cycle durations; accelerated cracking is observed when compared to the 2000^{o}F loading

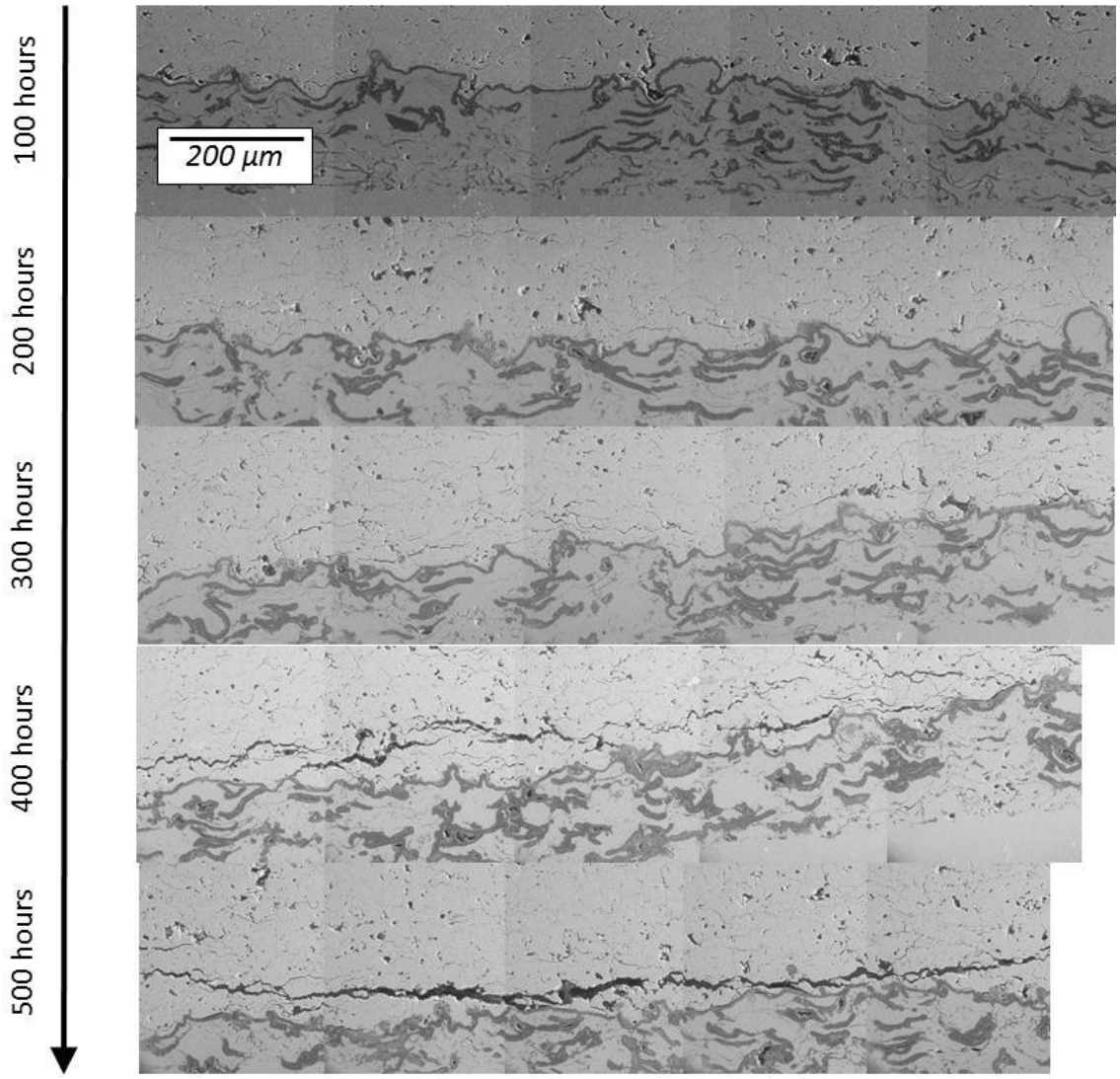

Figure 4.2 – Evolution of the interface for loading at 2000°F with 50 hour cycle durations; intermediate length cracks (400 hrs) coalesce into long cracks (500 hrs) just before failure

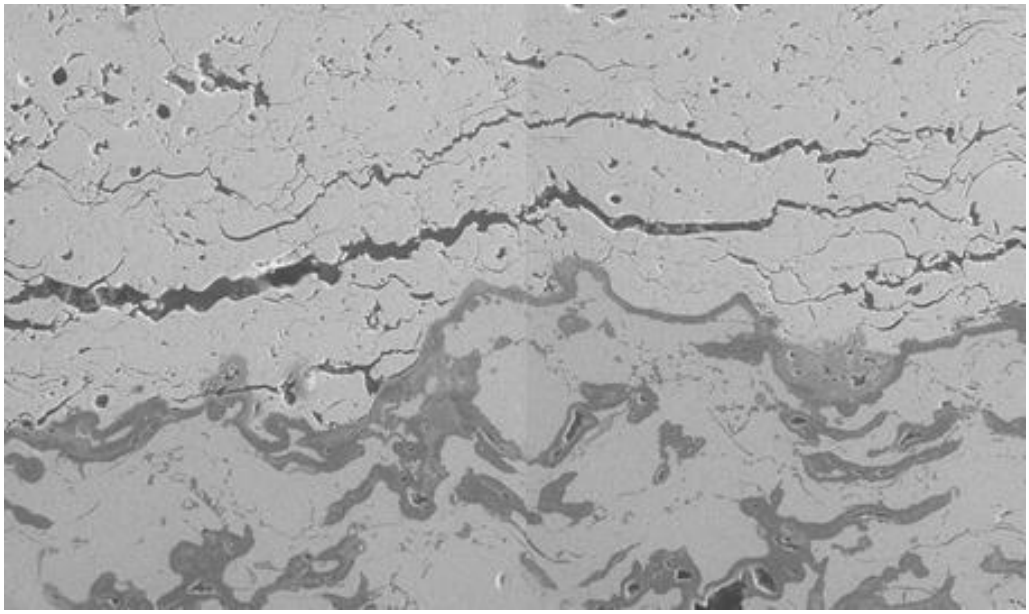

Figure 4.3 – Micrograph showing that cracks are often extended over peaks (350 hours, 2000^{o}F)

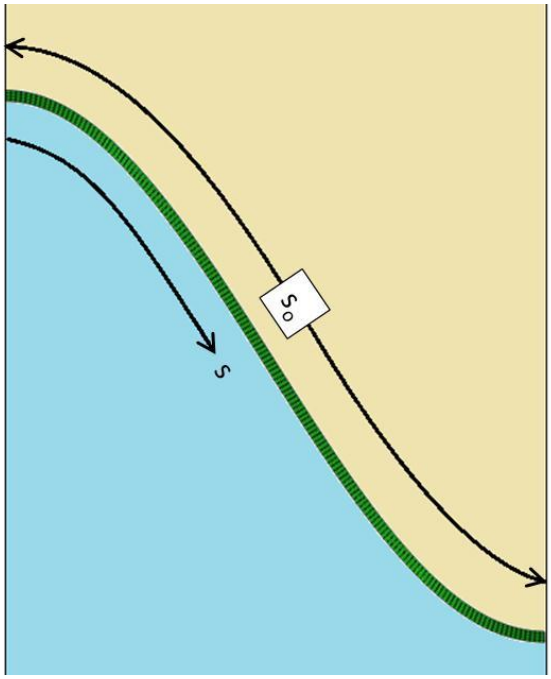

Figure 4.4 – Coordinates for stresses in Figure 4.5

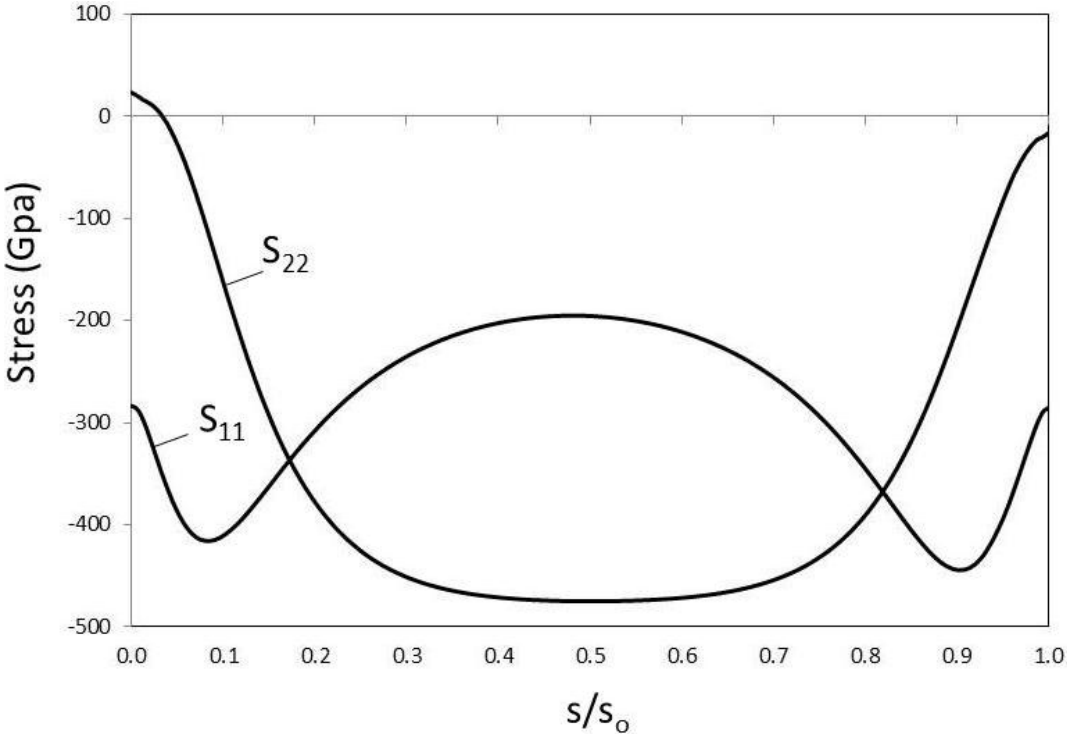

Figure 4.5 –Stresses in the TGO plotted along the path shown in Figure 4.4 (TGO elastic, YSZ elastic)

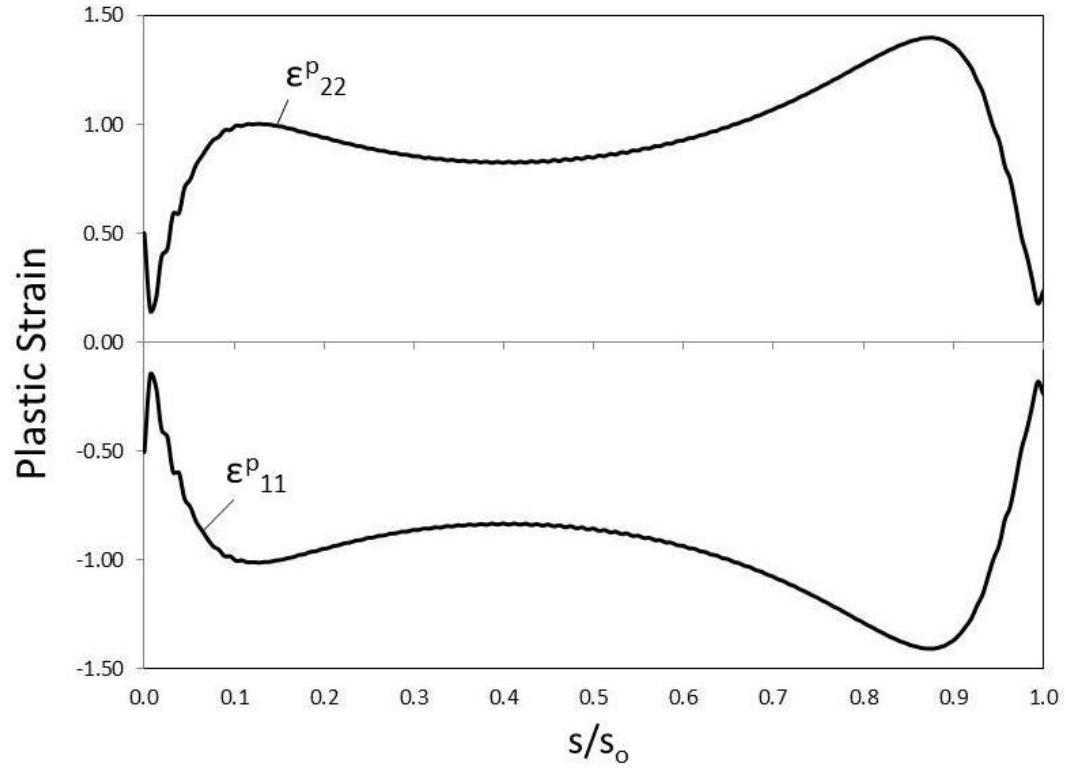

Figure 4.6 – Plastic strain accumulation in the TGO (TGO plastic, YSZ elastic)

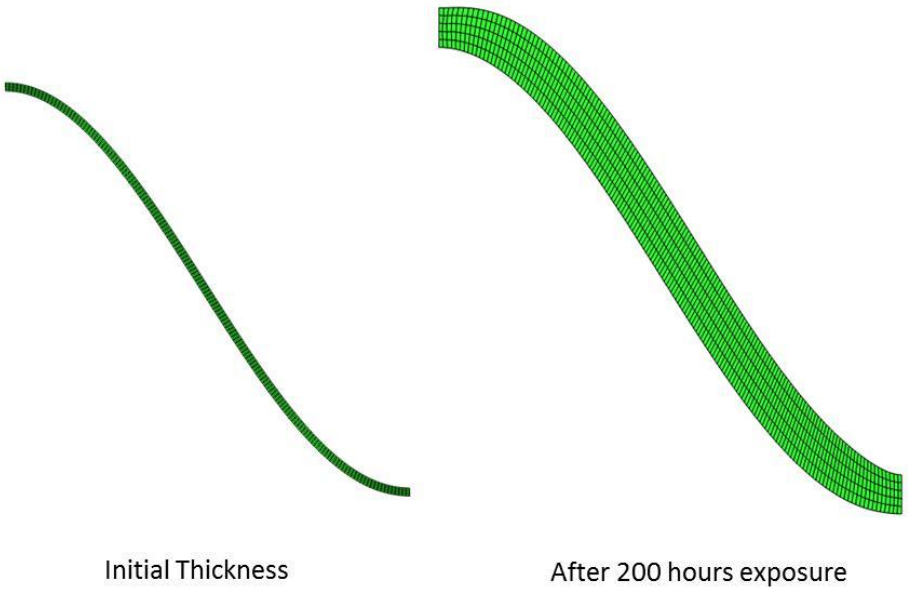

Figure 4.7 – Shape of the TGO after 200 hours of hot time due to growth and plastic strain

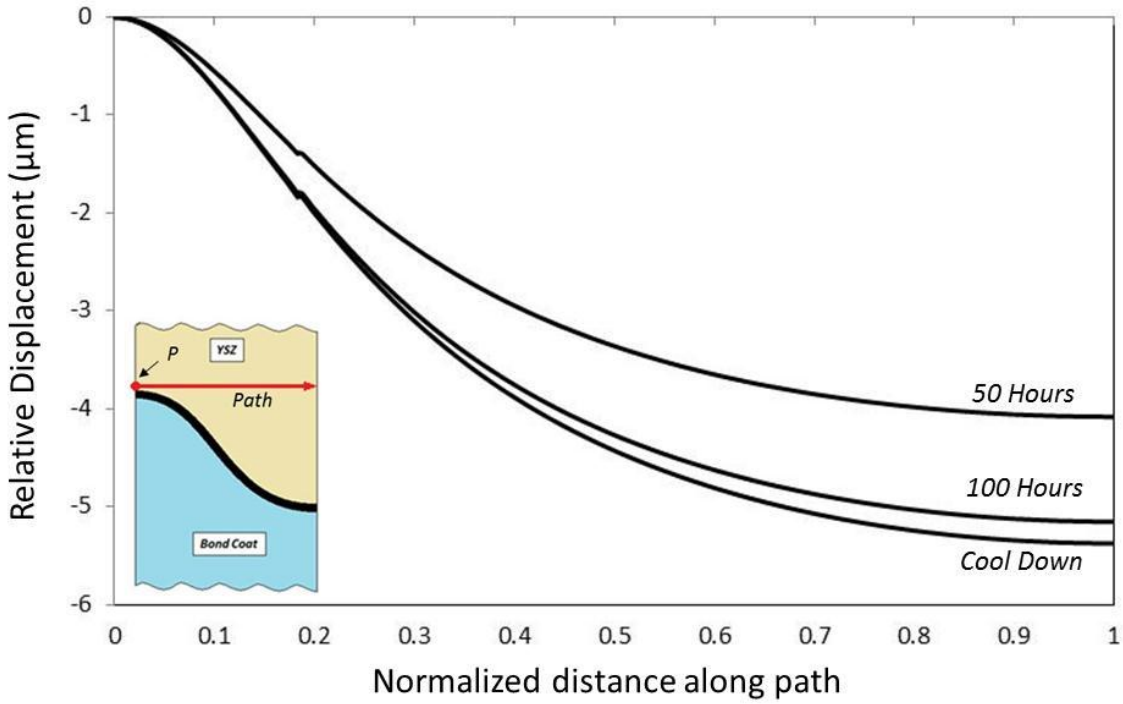

Figure 4.8 – Displacements along the path indicated relative to displacement at location P (TGO elastic, YSZ elastic)

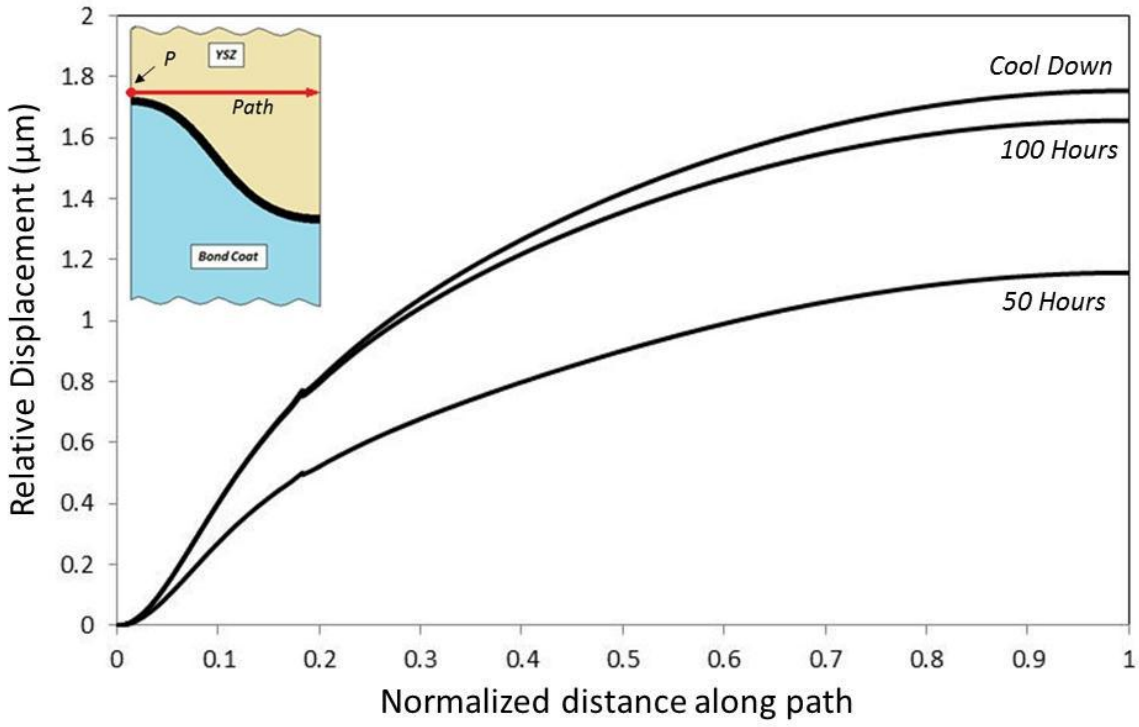

Figure 4.9 – Displacements along the path indicated relative to displacement at location P (TGO plastic, YSZ elastic)

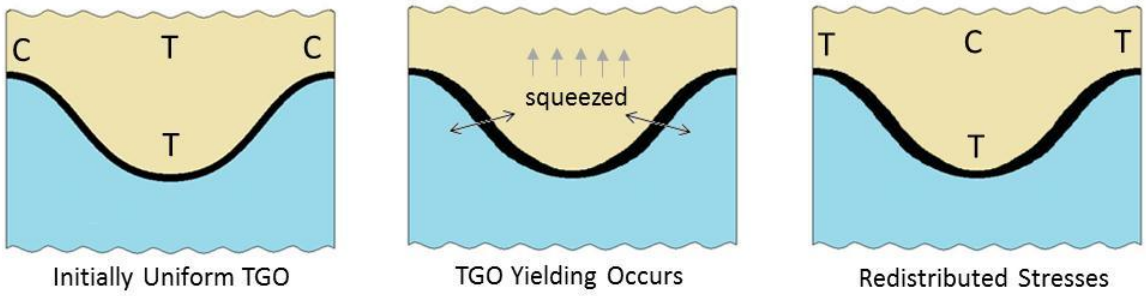

Figure 4.10 – Schematic showing redistribution of stress in the linear elastic YSZ when the TGO is perfectly plastic: as the TGO yields, the plastic strain causes the YSZ in the valley to incur excessive in-plane compression, translating into extra vertical elongation of that material, causing the material above the valley to become raised relative to the material above the peak, putting it into tension

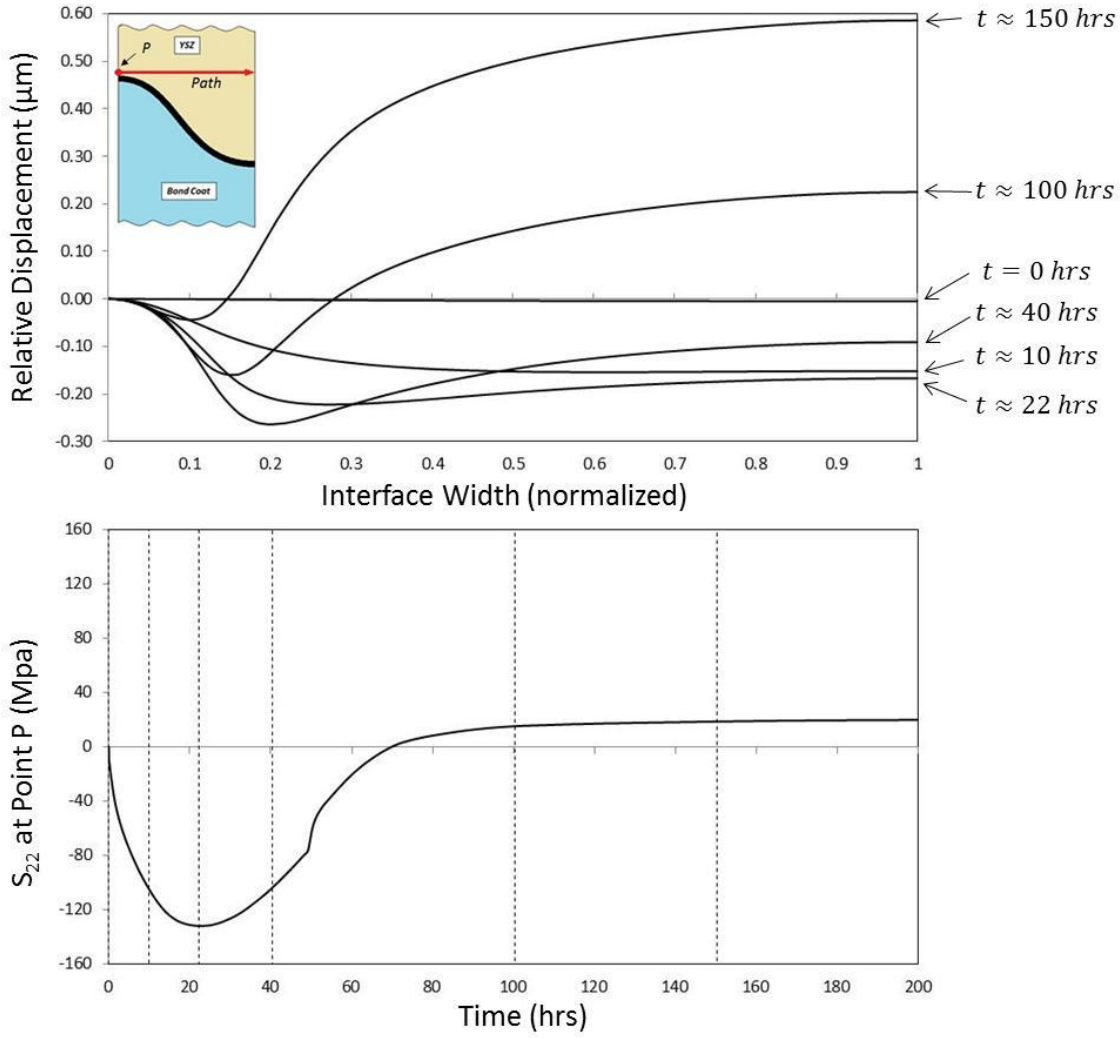

Figure 4.11 – Below: out-of-plane stress vs. time at location P (200 hr cycle, 2000°F), dotted lines correspond to displacement output times above; above: displacements along the path indicated relative to displacement at point P at times indicated

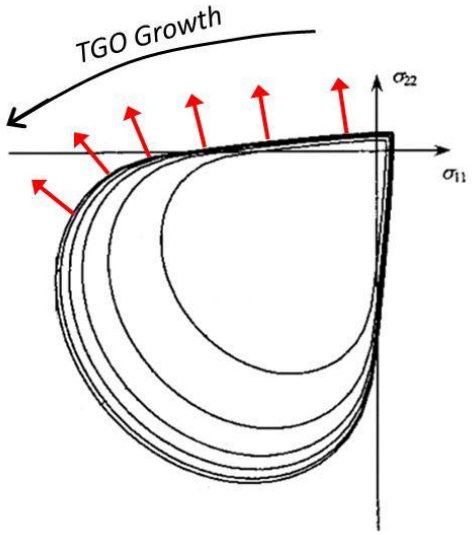

Figure 4.12 – YSZ in the valley is initially tensile, but with increasing in-plane compression from TGO growth it turns compressive

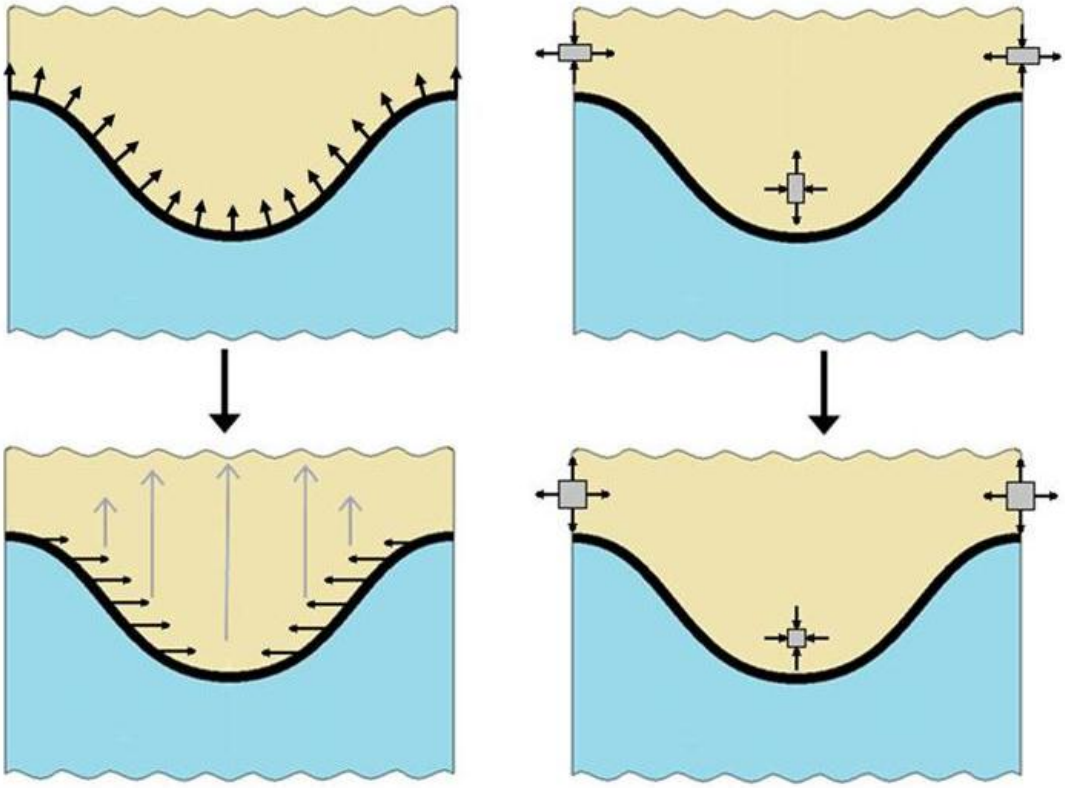

Figure 4.13 – Initially, the YSZ trends to same stress state it would assume if it was elastic, but as the material in the valley reaches its flow stress, it begins to flow upward due to the horizontal component of TGO growth and puts the material above the peak into tension

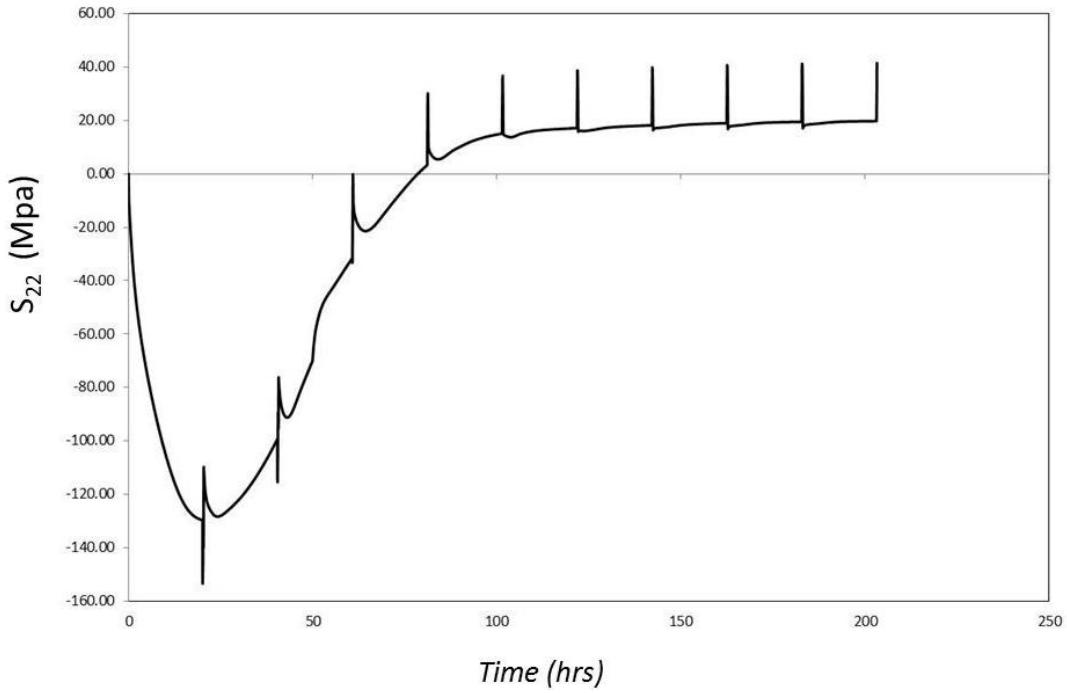

Figure 4.14 – Out-of-plane stress vs. time at location P (20 hour cycles, 2000°F); the stresses immediately following cool down illustrate the effect back stress has on the system

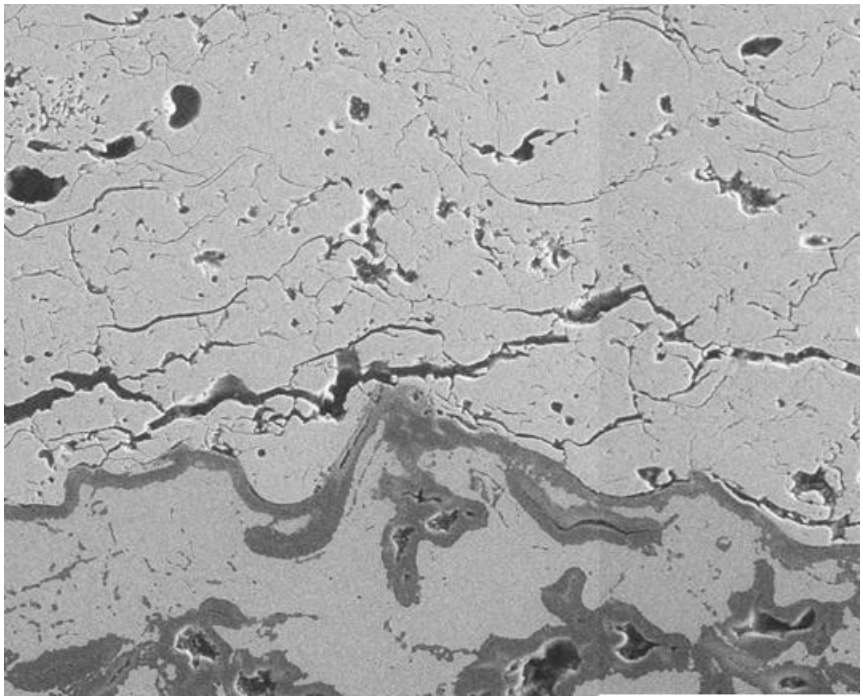

Figure 4.15 – Micrograph of damaged coating supporting the damage patterns seen in inelastic strain contour plots (450 hrs, 2000°F)

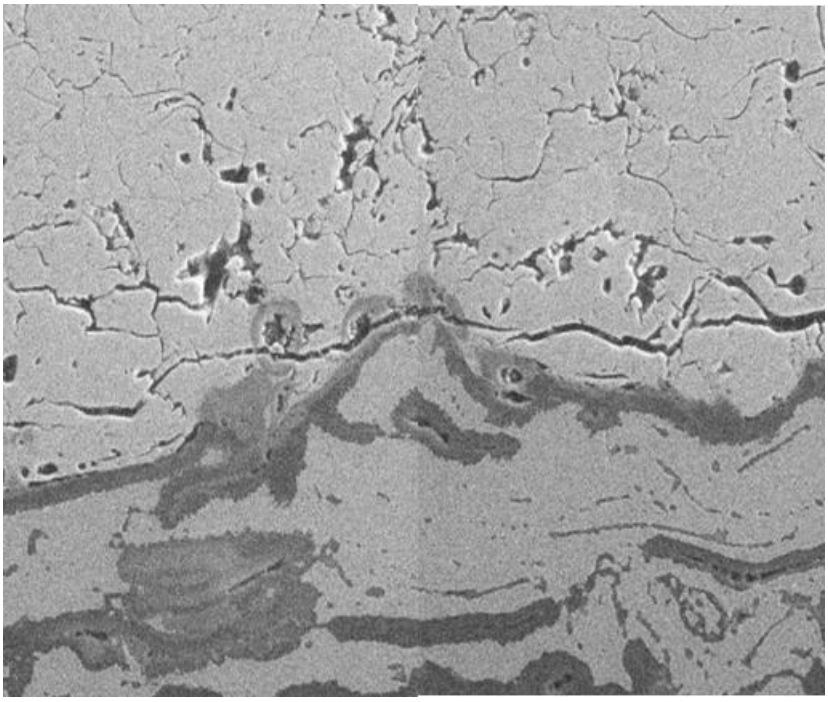

Figure 4.16 – Micrograph of damaged coating supporting the damage patterns seen in inelastic strain contour plots (450 hrs, 2000^{o}F)

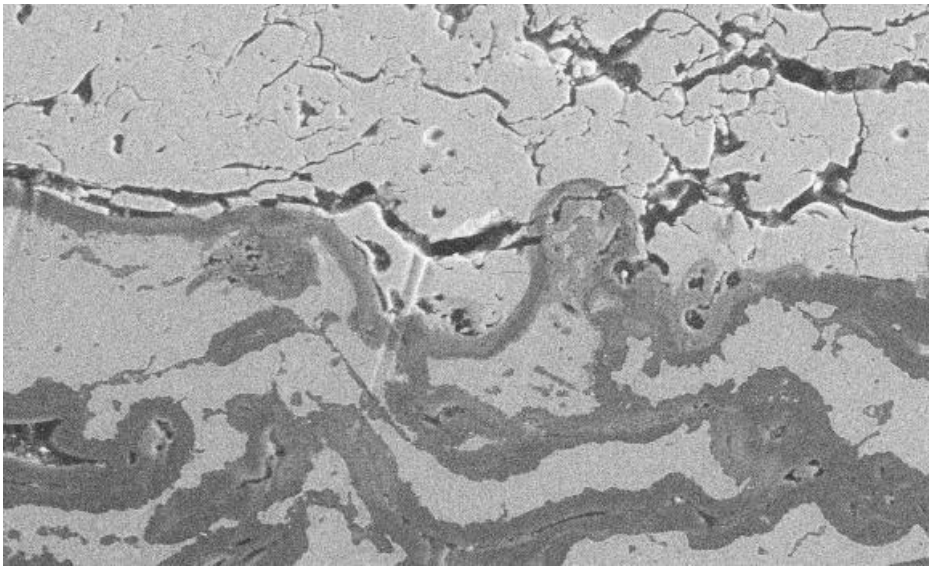

Figure 4.17 – Micrograph of damaged coating supporting the damage patterns seen in inelastic strain contour plots (500 hrs, 2000^{o}F)

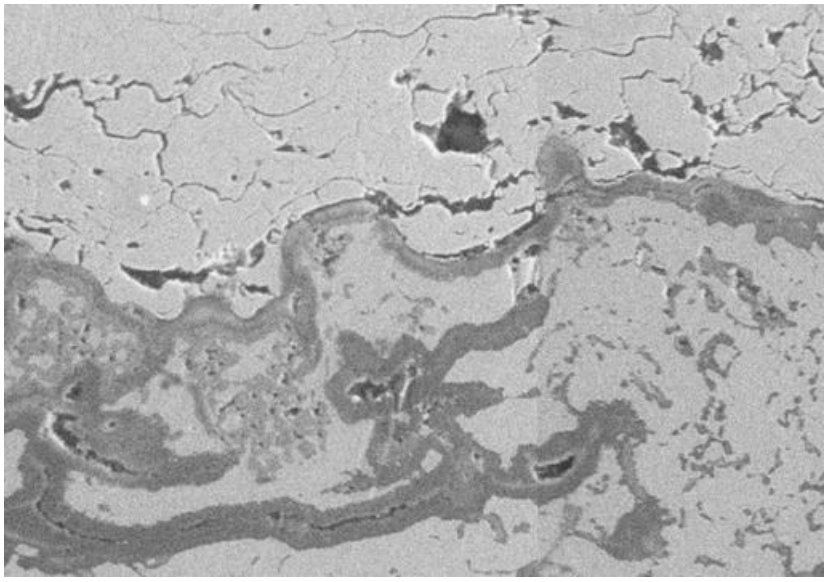

Figure 4.18 – Micrograph of damaged coating supporting the damage patterns seen in inelastic strain contour plots (500 hrs, 2000^{o}F)

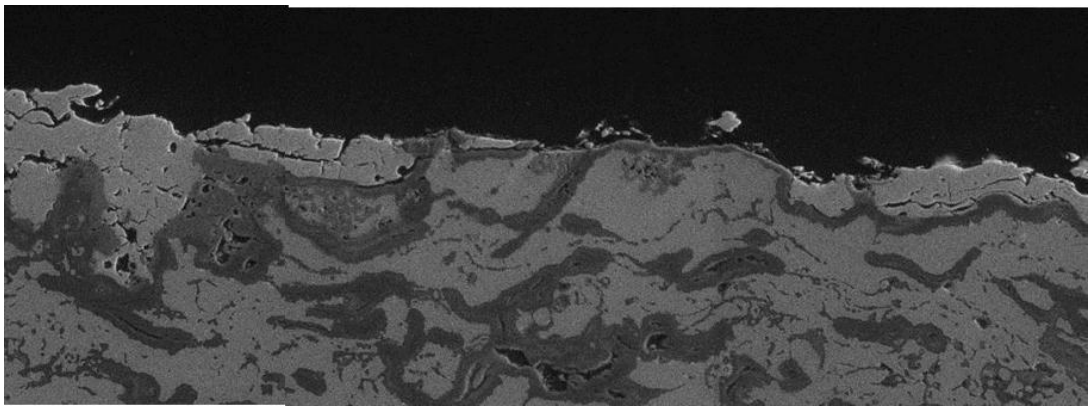

Figure 4.19 – Micrograph of damaged coating supporting the damage patterns seen in inelastic strain contour plots (250 hrs, 2100^{o}F)

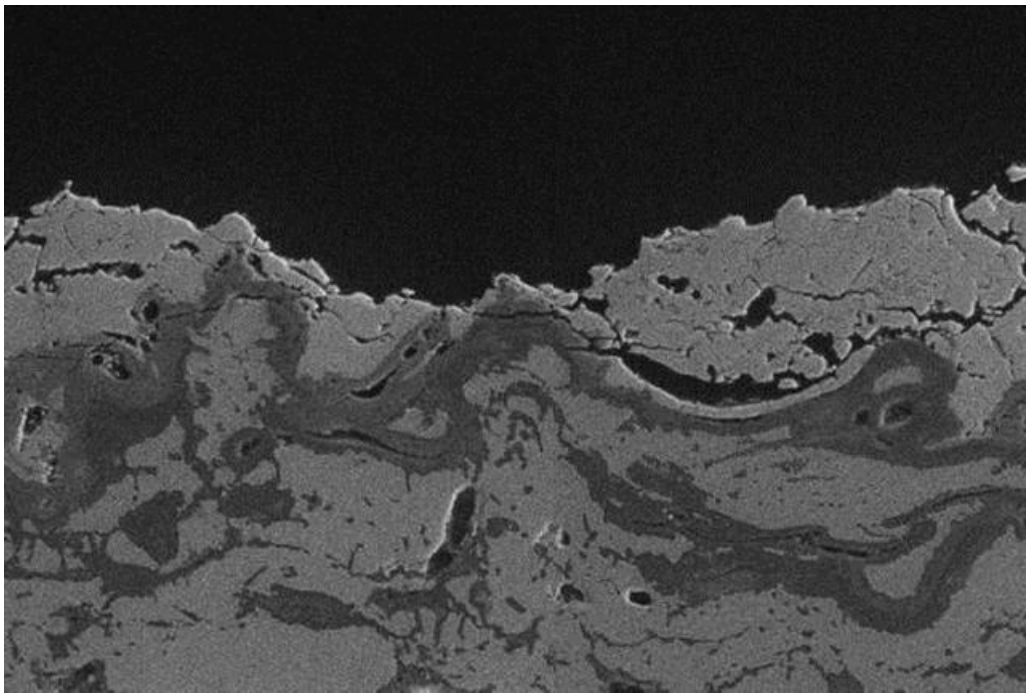

Figure 4.20 – Micrograph of damaged coating supporting the damage patterns seen in inelastic strain contour plots (250 hrs, 2100^{o}F)

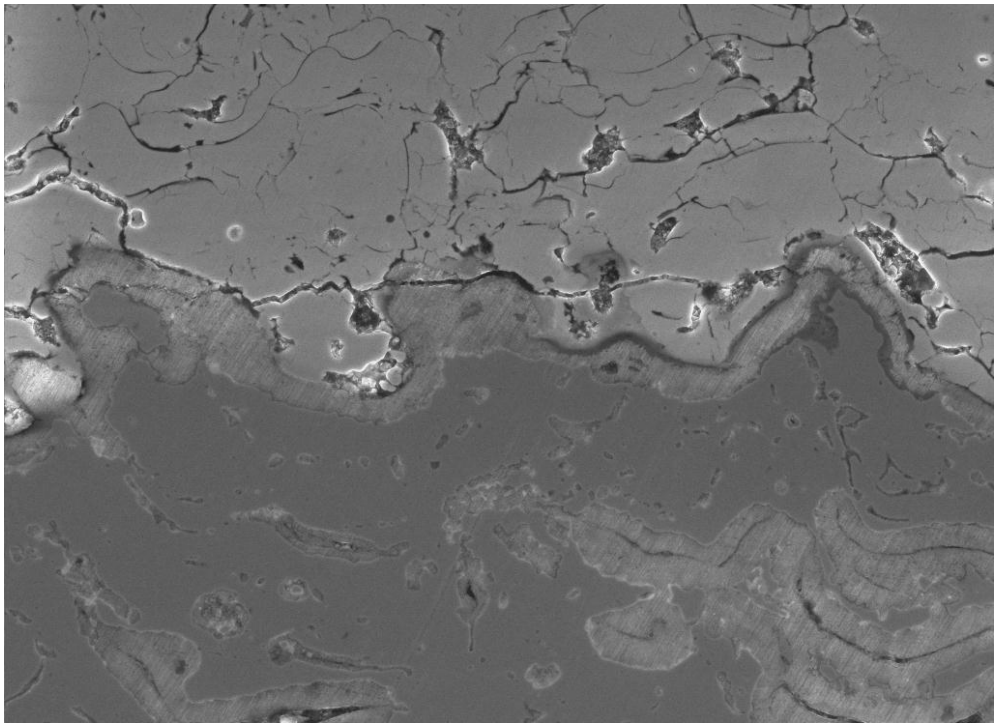

Figure 4.21 – Micrograph of damaged coating supporting the damage patterns seen in inelastic strain contour plots (150 hrs, 2100^{o}F)

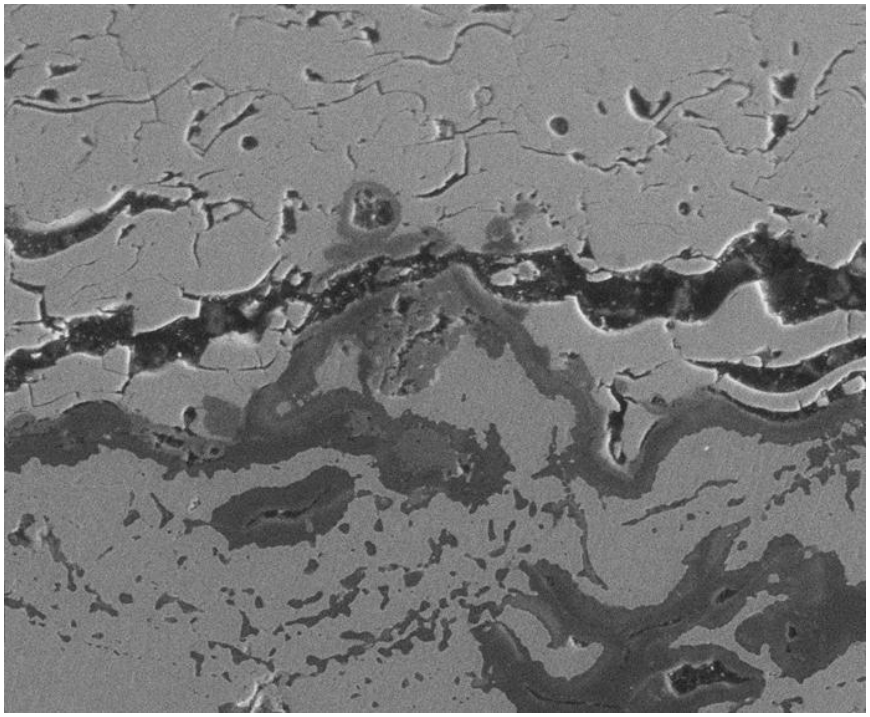

Figure 4.22 – Micrograph of damaged coating supporting the damage patterns seen in inelastic strain contour plots (200 hrs, 2100°F)

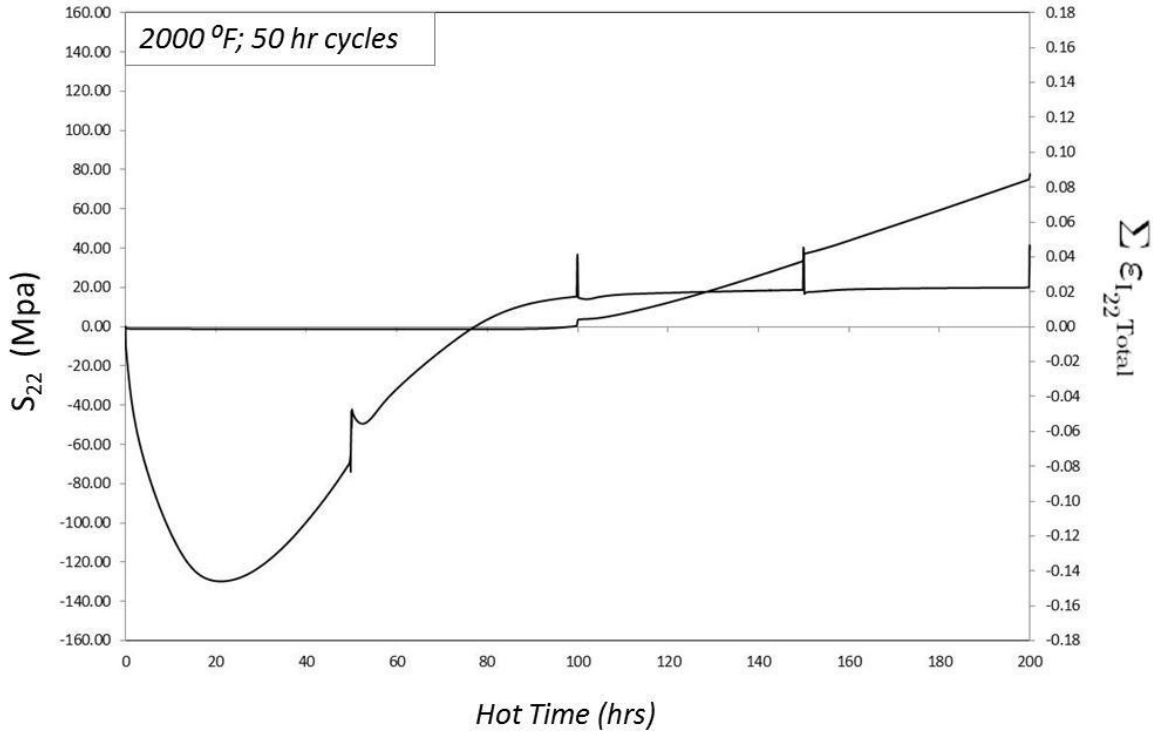

Figure 4.23 – Out-of-plane stress vs. time at location P plotted against inelastic strain accumulation; shows the manner in which inelastic strain accumulates (50 hour cycles, 2000°F)

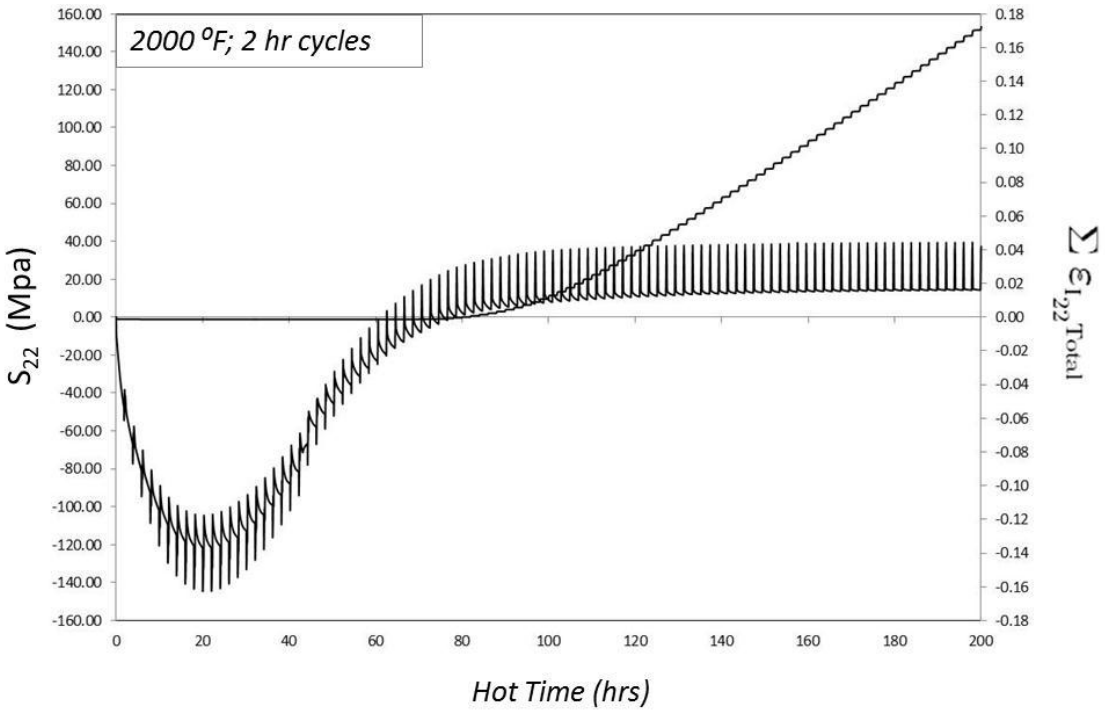

Figure 4.23 – Out-of-plane stress vs. time at location P plotted against inelastic strain accumulation; shows the manner in which inelastic strain accumulates (2 hour cycles, 2000°F)

5. Conclusions

5.1 Experimental

1. TGO growth for this particular coating was observed to be parabolic.
2. Increase in tortuosity of the TGO/bond coat interface was found to be roughly proportional to TGO thickness.
3. In all three types of samples (combustor liner samples, oxidation test samples, and the burner rig sample) failure was brought on in the same manner: by crack propagation in the YSZ just above the YSZ/TGO interface.
4. Final failure of the oxidation test samples was confirmed to be by buckling. Final failure of the combustor liner samples and the burner rig sample was inferred to be by buckling.
5. Failure was found to be independent of loading type (actual in-service loading, uniform temperature loading, and thermal gradient loading).
6. The general failure mechanism was determined to be of the "imperfection/bond coat geometry induced failure" type.

5.2 Modeling

5.2.1 Linear YSZ

1. Stresses due to TGO growth far outweigh stresses due to thermal mismatch alone.

2. Stresses due to bond coat rumpling may outweigh the stresses due to TGO growth, but more accurate measurements of the manner of shape change associated with bond coat rumpling needs to precede the modeling for this to be determined.
3. Aluminum depletion from the bond coat has an effect similar to a slight lowering of the TGO growth rate. Its effect on stresses in the YSZ is minimal compared to TGO growth and rumpling.
4. TGO plasticity, in the extreme case, causes the TGO to bulge in its middle, which adds to the in-plane compression of the YSZ in the valley, which in turn can cause material above the peak to experience tension.
5. A realistic constitutive law for the YSZ needs to be used for unrealistically high stresses to be avoided.

5.2.2 Viscoplastic YSZ

1. When the YSZ is considered to be viscoplastic with an asymmetric flow surface, TGO growth causes material in the valley to flow upward, putting pressure on the material above it, which causes the material over the peak to experience tension.
2. The stress state in the viscoplastic YSZ can be affected by rumpling in different ways, depending on the manner in which it is implemented. If amplitude increases and wavelength remains constant, the material in the valley will remain in tension and the material above the peak in compression.

If the frequency increases and amplitude remains constant, the material in the valley will go into compression and the material above the peak into tension.

3. TGO plasticity accelerates the conversion in stress that takes place in the viscoplastic YSZ due to TGO growth.
4. The conversion from compression to tension over the peak takes place at a more or less constant TGO thickness when different temperatures are considered.
5. Stresses in the YSZ in models with shorter cycles have smaller magnitudes than in models with longer cycles, but the effect becomes hardly noticeable in cycles longer than about 50 hours. The difference in stresses resulting from different cycle durations is minimal directly above the peak and most pronounced about 20 to 25 μm above the peak.
6. Inelastic strain is a good indicator of the amount of damage incurred in the YSZ since it shows a strong dependence on temperature and cycle duration, which are two of the major observable factors that affect coating life.
7. A combination of low temperature inelastic strain and high temperature inelastic strain could very well be capable of predicting coating life. The inelastic strain output from the finite element models could be worked down into a simple life prediction formula for the current system, and the models themselves could be used to assess life sensitivities to inputs such as material properties and geometries.

References

1. J.H. Perepezko, “The Hotter the Better”, Science, 20 November 2009: Vol. 326 no. 5956 pp. 1068-1069

2. R.A. Miller, “Thermal Barrier Coatings for Aircraft Engines: History and Directions”, Journal of Thermal Spray Technology, Volume 6(1), March 1997, pp. 35-42

3. R.A. Miller, “History of Thermal Barrier Coatings for Gas Turbine Engines”: Kloster Irsee, Germany, August 12-17 2007, NASA/TM—2009-215459

4. S. Stecura, “Effects of Compositional Changes on the Performance of a Thermal Barrier Coating System”, NASA TM-78976, National Aeronautics and Space Administration, 1978

5. N.P. Padture, M. Gell, E.H. Jordan, “Thermal Barrier Coatings for Gas-Turbine Engine Applications,” Science, 2002: 296, pp. 280-284

6. K. Vaidyanathan, “Failure Mechanisms of Platinum Aluminide Bond Coat/Electron Beam – Physical Vapor Deposited Thermal Barrier Coatings”, PhD Dissertation, University of Connecticut (2001)

7. R.L. Jones, “Experience in Seeking Stabilizers for Zirconia Having Hot Corrosion-Resistance and High Temperature Tetragonal (t’) Stability”, Naval Research Laboratory, April 16 1996, NRL/MR/6170—96-7841

8. S.M. Meier, D.K. Gupta, “The Evolution of Thermal Barrier Coatings in Gas Turbine Engine Applications”, J. Eng. Gas Turbines Power, 116, 1994, pp. 250-257

9. K.A. Marino, E.A. Carter, “The Effect of Platinum on Al Diffusion Kinetics in β-NiAl: Implications for Thermal Barrier Coating Lifetime”, Acta Materialia, Volume 58, Issue 7, April 2010, Pages 2726-2737

10. A.G. Evans, D.R. Mumm, J.W. Hutchinson, G.H. Meier, F.S. Pettit, “Mechanisms Controlling the Durability of Thermal Barrier Coatings”, Progress in Materials Science, vol. 46, issue 5, 2001, pp. 505-553

11. C. H. Hsueh , E. R. Fuller, “Analytical Modeling of Oxide Thickness Effects on Residual Stresses in Thermal Barrier Coatings”, Scripta Materialia, Volume 42, Issue 8, 31 March 2000, Pages 781-787

12. K. W. Schlichting, N. P. Padture, E. H. Jordan, M. Gell, “Failure Modes in Plasma-Sprayed Thermal Barrier Coatings”, Materials Science and Engineering A, Volume 342, Issues 1-2, 15 February 2003, Pages 120-130

13. M. Ahrens, R. Vassen, D. Stover, “Stress Distributions in Plasma-Sprayed Thermal Barrier Coatings as a Function of Interface Roughness and Oxide Scale Thickness”, Surface and Coatings Technology, Volume 161, Issue 1, 1 November 2002, pp. 26-35

14. C. H. Hsueh, E. R. Fuller, “Residual Stresses in Thermal Barrier Coatings: Effect of Interface Asperity Curvature/Height and Oxide Thickness”, Material Science and Engineering A, 283 (2000), pp. 46-55

15. P. Bernarz, “Finite Element Simulation of Stress Evolution in Thermal Barrier Coatings”, PhD Dissertation, Aachen, RWTH, 2006

16. M.Y He, J.W. Hutchinson, A.G. Evans, “Simulation of Stresses and Delamination in a Plasma-Sprayed Thermal Barrier System upon Thermal Cycling”, Materials Science and Engineering A, 345, (2003), pp. 172-178

17. K. Vaidyanathan, E.H. Jordan, M. Gell, “Surface geometry and strain energy effects in the failure of a (Ni, Pt)Al/EB-PVD thermal barrier coating”, Acta Materialia, vol. 52 (2004), pp. 1107-1115

18. D. Zhu, L.J. Ghosn, R.A. Miller, “Failure Mechanisms and Life Prediction of Thermal and Environmental Barrier Coatings under Thermal Gradients”: 32nd International Conference on Advanced Ceramics and Composites, 30 January 2008

19. Y.R. Takeuchi, K. Kokini, “Thermal fracture of multilayer ceramic thermal barrier coatings”: ASME, International Gas Turbine and Aeroengine Congress and Exposition, 37th, Cologne, Germany, 1-4 June 1992

20. K. Kokini, A. Banerjee, T.A. Taylor, “Thermal Fracture of Interfaces in Precracked Thermal Barrier Coatings”, Materials Science and Engineering, A323 (2002), pp. 70-82

21. J.W. Hutchinson, A.G. Evans, “On the Delamination of Thermal Barrier Coatings in a Thermal Gradient”, Surface and Coatings Technology, 149 (2002), pp. 179-184

22. E.P. Busso, J. Lin, S. Sakurai, “A Mechanistic Study of Oxidation-Induced Degradation in a Plasma-Sprayed Thermal Barrier Coating System. Part I: Model Formulation”, Acta Materialia, 49 (2001), pp. 1515-1528

23. E.P. Busso, J. Lin, S. Sakurai, “A Mechanistic Study of Oxidation-Induced Degradation in a Plasma-Sprayed Thermal Barrier Coating System. Part II: Life Prediction Model”, Acta Materialia, 49 (2001), pp. 1529-1536

24. R.A. Miller, “Oxidation-Based Model for Thermal Barrier Coating Life”, Journal of the American Ceramic Society, Vol 67, no.8, August 1984

25. R.V. Hillery, B.H. Pilsner, R.L. McKnight, T.S. Cook, M.S. Hartle, “Thermal Barrier Coating Life Prediction Model Development”, 1988, NASA-CR 180807

26. J.T. DeMasi, K.D. Sheffler, M. Ortiz, “Thermal Barrier Coating Life Prediction Model Development: Phase I”, 1989, NASA-CR 182230

27. S.M. Meier, D.M. Nissley, K.D. Sheffler, “Thermal Barrier Coating Life Prediction Model Development: Phase II”, 1991, NASA-CR 189111

28. W. Xie, K.P. Walker, E.H. Jordan, M. Gell, “Implementation of a Viscoplastic Model for a Plasma Sprayed Ceramic Thermal Barrier Coating”, Journal of Engineering Materials and Technology, vol. 125, issue 2, April 2003, pp. 200-207

29. “Blade Life Management: Coating Systems, EPRI, Palo Alto, CA: 2002. 1006608

30. T. Beck, R. Herzog, O. Trunova, M. Offermann, R.W. Steinbrech, L. Singheiser, “Damage mechanisms and lifetime behavior of plasma-sprayed thermal barrier coating systems for gas turbines – Part I: Experiments”, Surface & Coatings Technology, vol. 202 (2008), pp. 5027-5032

31. T. Beck, R. Herzog, O. Trunova, M. Offermann, R.W. Steinbrech, L. Singheiser, “Damage mechanisms and lifetime behavior of plasma-sprayed thermal barrier coating systems for gas turbines – Part II: Modeling”, Surface & Coatings Technology, vol. 202 (2008), pp. 5901-5908

32. *ABAQUS Analysis User’s Manual*, Dassault Systèmes Simulia Corp., Providence, RI, USA, 2010

33. *ABAQUS User Subroutines Reference Manual*, Dassault Systèmes Simulia Corp., Providence, RI, USA, 2010

34. L.A. Janosik, S.F. Duffy, “A Viscoplastic Constitutive Theory for Monolithic Ceramics – I”, J. Eng. Gas Turbines Power, vol. 120, January 1998, pp. 155-162

35. K. Vaidyanathan, M. Gell, E.H. Jordan, “Mechanisms of spallation of electron beam physical vapor deposited thermal barrier coatings with and without platinum aluminide bond coat ridges”, Surface and Coatings Technology, Volumes 133-134, November 2000, pp. 28-34

36. B.A. Pint, I.G. Wright, W.Y. Lee, Y. Zhang, K. Prubner, K.B. Alexander, “Substrate and bond coat compositions: factors affecting alumina scale adhesion”, Materials Science and Engineering, A245 (1998), pp. 201-211

37. S. Sridharan, L. Xie, E.H. Jordan, M. Gell, K.S. Murphy, “Damage evolution in an electron beam physical vapor deposited thermal barrier coating as a function of cycle temperature and time”, Materials Science and Engineering, A 393 (2005), pp. 51-62

38. Hiroshi Tada, Paul C. Paris, George R. Irwin, *The Stress Analysis of Cracks Handbook*. 3rd ed. New York, NY: The American Society of Mechanical Engineers. 2000.

39. Neil Birks, Gerald Meier, and Fred Pettit. *Introduction to the High Temperature Oxidation of Metals*. 2nd ed. New York, NY: Cambridge University Press, 2006.